Kinoshita, M., Tobin, H., Ashi, J., Kimura, G., Lallemant, S., Screaton, E.J., Curewitz, D.,
Masago, H., Moe, K.T., and the Expedition 314/315/316 Scientists
Proceedings of the Integrated Ocean Drilling Program, Volume 314/315/316

Expedition 315 Site C0001[1]

Expedition 315 Scientists[2]

Chapter contents

Introduction

Integrated Ocean Drilling Program (IODP) Site C0001 (proposed Site NT2-03B) targeted the uppermost 1000 meters below seafloor (mbsf) at the seaward slope of the Kumano Basin uplift (outer arc high) where the megasplay fault system branches and may approach the surface (Figs. **F1**, **F2**). The upper 1000 m drilled during this expedition provides an opportunity to access the thrust sheets uplifted by several branches of the megasplay fault system, as well as a thin overlying slope basin cover sequence. The nature of the material in these thrust sheets is unknown. The acoustically nonreflective nature of this section suggests that it may be composed of chaotically deformed accretionary wedge sedimentary mélange transported from significantly greater depths. Alternatively, this zone may be composed of highly deformed Kumano forearc basin sediments. It may also be a structurally juxtaposed combination of both.

The principal objective during IODP Expedition 315 was to reveal the stratigraphic, physical, structural, and chemical features of materials obtained from the shallow accretionary prism and the overlying slope basin. An integrated interpretation is proposed based on these findings combined with seismic and log data obtained during IODP Expedition 314. Coring at this site also provides critical pilot hole information for future riser drilling. To achieve the ~3500 m total depth objective using riser and weighted drilling mud involves setting multiple casing strings, with the depth of each depending on the least principal stress, the fracture strength of the formation, and the pore fluid pressure gradient. The key part of this casing plan is the "top-hole" portion, where tolerances on mud weight are tight. Planning the casing program, therefore, requires excellent information on physical properties in the uppermost 1000 m. In light of this, our strategy is to utilize riserless coring for this section during a future stage of the Nankai Trough Seismogenic Zone Experiment (NanTroSEIZE). Furthermore, downhole (in situ) temperature measurements were conducted as deeply as possible, which will enable estimation of deeper temperatures by extrapolation. These measurements will provide critical information for well planning of the 3.5 km riser hole and will aid in the design of sensors and telemetry of the long-term borehole observatory planned for a future NanTroSEIZE stage.

---

[1] Expedition 315 Scientists, 2009. Expedition 315 Site C0001. *In* Kinoshita, M., Tobin, H., Ashi, J., Kimura, G., Lallemant, S., Screaton, E.J., Curewitz, D., Masago, H., Moe, K.T., and the Expedition 314/315/316 Scientists, *Proc. IODP,* 314/315/316: Washington, DC (Integrated Ocean Drilling Program Management International, Inc.). doi:10.2204/iodp.proc.314315316.123.2009

[2] **Expedition 314/315/316 Scientists' addresses.**

Operations

Locations of holes drilled during Expedition 315 are shown in Figure F3.

Transit from Site C0006 to Site C0001

The D/V *Chikyu* departed IODP Site C0006, the last location of Expedition 314, at 1700 h on 15 November 2007. The 14 nmi transit was covered at an average speed of 3.5 kt. Rig maintenance was carried out upon arrival at Site C0001 at 2100 h on the same day.

Hole C0001E

After making up a hydraulic piston coring system (HPCS)/extended shoe coring system (ESCS) coring assembly with an 11⁷⁄₁₆ inch bit, we started running in Hole C0001E at 0000 h on 17 November 2007 (Table T1). A mechanical failure was found in a drawworks motor while running in the hole to 1706 m drillers depth below rig floor (DRF). We pulled the assembly to the surface, and inspection of the drawworks started at 2145 h. Troubleshooting of the drawworks' A and B motors continued to 0200 h on 19 November. We made up an 11⁷⁄₁₆ inch HPCS/ESCS coring assembly and continued to run in the hole at 0930 h. We observed the HPCS core barrel drop through the core bit during running with core line at 1515 m DRF because of a loose connection from severe vibration induced by the strong current. A fishing operation started at 1645 h, and we successfully retrieved the core barrel at 0200 h on 20 November. We restarted running in the hole to the seafloor and shot the first core at 2211.6 m DRF at 0415 h. The first core was on deck at 0500 h. HPCS coring continued until the morning of 21 November, and we cut 13 cores. In situ temperature measurement was carried out with the advanced piston corer temperature tool (APCT3) on Cores 315-C0001E-2H, 5H, 8H, and 11H. After shooting Core 315-C0001E-14H, the inner barrel could not be freed with 450 kN maximum overpull. We rotated the string with 450 kN of overpull by mistake, which resulted in an inner barrel break at the bottom of the second rod connection. An APCT3 tool with an HPCS inner barrel assembly (except for a middle/upper piston rod and landing shoulder sub) was also lost. We displaced the hole with 1.3 specific gravity kill mud and pulled out of hole from 2344 to 2163 m DRF at 0830 h on 21 November.

Hole C0001F

After we abandoned Hole C0001E, we moved 20 m eastward and spudded Hole C0001F (Table T2) at 0945 h on 22 November 2007. After washing to 108 m drillers depth below seafloor (DSF), we started coring with ~10 m of overlap with the previous hole. We cored 121.8 m and cut 19 cores with the HPCS. Our recovery rate was >100% for most cores; however, some relatively deep cores showed obvious flow-in structures. In situ temperature measurements were carried out using the APCT3 on Cores 315-C0001F-2H, 5H, 8H, and 11H. Because the formation became stiff, we changed to the ESCS from the twentieth core and then cored an additional 19.0 m and cut two cores. Core recovery was good for both cores; however, severe drilling disturbance was observed on X-ray computed tomography (CT) scan imagery, suggesting that we could not get good samples for physical and mechanical properties. We therefore decided to stop ESCS coring and switch to the rotary core barrel (RCB). We abandoned the hole by displacing with 1.3 specific gravity kill mud and then pulled out of the hole and recovered the remotely operated vehicle (ROV) under drifting at an average speed of 0.8 kt at 0500 h on 24 November.

Hole C0001G

We started making up a 10⅝ inch RCB assembly at 0845 h on 24 November 2007 and started running in the hole at 1300 h (Table T3). We spudded Hole C0001G at 0130 h on 25 November. After jetting to 74.5 mbsf, we started drilling. Just after drilling started, the ROV umbilical cable wrapped around the drill pipe. We stopped drilling and started pulling out of the hole at 1415 h. We safely recovered the ROV on board at 1500 h and confirmed it had no fatal damage.

Hole C0001H

After moving the vessel 6 nmi upcurrent at an average speed of 3.0 kt, we restarted running in the hole at 0000 h on 26 November 2007 (Table T4). We spudded Hole C0001H at 0515 h, ~10 m away from the previous hole. After jetting to 74 mbsf, we started drilling with an RCB assembly with a center bit. Washing to 230.0 mbsf, we retrieved the center bit and started RCB coring at 1445 h. The first RCB core arrived on deck at 1704 h. The ROV umbilical cable wrapped around the drill pipe at 0300 h on 27 November, but we recovered it at 0530 h without retrieving it to the surface. After cutting Core 315-C0001H-20R at 412.5 m core depth below seafloor (CSF), we observed high torque up to 18 kNm. Torque returned to normal (3–5 kNm) after we pumped 10 m^3 of Hi-Vis mud twice. Round mudstone gravel, typical of borehole caving, was observed at the top of Cores 315-C0001H-18R (~15 cm) and 20R.

Core recovery was generally as low as 30%–35%, except for one core that yielded almost full recovery. Correlation between drilling parameters and core recovery was uncertain. As the weather was worsening, we stopped coring at 448.0 m CSF after cutting Core 315-C0001H-24R and started free-fall funnel (FFF) installation at 1600 h on 28 November.

We completed installation of the FFF by 0700 h on 29 November, and then we pulled the pipe to 35 mbsf and waited on weather for the rest of the day. As the weather improved that night, we started running in the hole at 2330 h. After washing from 152 to 381 mbsf, we swept and reamed with Hi-Vis mud from 381 to 448 mbsf. We restarted coring at 0700 h on 30 November and cut two cores from 447.2 to 457.8 m CSF. The pipe stuck while coring and was released with 350 kN overpull; we then decided to stop coring. We displaced the hole with 1.3 specific gravity kill mud and started to pull out of the hole at 1230 h. The pipe was recovered at the surface by 2145 h. As the current was too strong to retrieve the ROV, we had to wait until the current was below the operational limit. Meanwhile, we made up a 10⅝ inch RCB drilling assembly. After moving the vessel 8.6 nmi to a low-current area at 0730 h on 1 December at an average sped of 0.7 kt, we retrieved the ROV at 2045 h while drifting. We started moving the vessel 5 nmi upcurrent of the well location from 2045 h at an average speed of 3.1 kt. Meanwhile, we repaired an ROV cursor cable.

We started running in the hole at 0200 h on 2 December. We launched the ROV at 0630 h and dove to the location at 0900 h. Having positioned the vessel to set the bit above the FFF at 1030 h, we reentered the hole at 1235 h. After washing and reaming from 299 to 458 m DSF, we started drilling at 1930 h. After repeating the reaming and wiper trip several times, we reached 600 m DSF, the starting depth for coring, at 2000 h on 3 December. We spotted 57 m^3 of 1.3 specific gravity kill mud and then started picking up out of the hole at 2030 h and retrieved the bottom-hole assembly to the surface at 0500 h. We moved the vessel 6 mni upcurrent and meanwhile made up an RCB coring assembly without a center bit. We started running in the hole at 0900 h and launched the ROV at 1330 h. The vessel was on location at 1845 h. We reentered the hole at 2010 h and continued running in the hole to 264 m DSF. We then started washing and reaming from 268 m DSF at 2200 h. Despite repeated washing and reaming, borehole conditions did not improve. After washing and reaming to 449 m DSF, we finally decided to abandon the hole at 1300 h on 5 December. We displaced the hole with 50 m^3 of 1.3 specific gravity kill mud and picked up the coring assembly to the seafloor. We moved the vessel 60 m eastward and spudded a new hole (C0001I).

Hole C0001I

We dropped a center bit and then spudded Hole C0001I at 1550 h on 5 December 2007 (Table T5). After jetting to 70 mbsf, we started drilling at 1700 h with a 10⅝ inch RCB assembly with a center bit. Drilling to 425 mbsf was relatively smooth. At every pipe stand, 10 m^3 of Hi-Vis mud was spotted. On 6 December, while picking up from 457 to 340 m DSF to change the wash pipe, both upper and lower inline blowout preventers were repaired. Running in the hole started at 1400 h, and we repeatedly washed and reamed to 520 m DSF. While backreaming 434 to 520 m DSF, we had a pipe stick at 464 m DSF. We managed to free the pipe with 700 kN of overpull. After escaping from this zone, we gave up further drilling and coring at 0315 h on 7 December. After displacing the hole with 35 m^3 of 1.5 specific gravity kill mud, we started pulling out of the hole at 0900 h and finished at 1400 h. The ROV dove to retrieve transponders at 1600 h. Meanwhile, we changed saver subs and repaired a leak on the top drive system. Four transponders were recovered at 0230 h on 8 December. We left the location for Site C0002 at 0230 h.

Lithology

We recognized two lithologic units during examination of cores from Site C0001 (Fig. F4). Unit I contains three subunits. Units and subunits are differentiated based on persistent contrasts in grain size, layer thickness, sedimentary structures, trace fossils, and mineralogy. We also considered the interpretations of logging-while-drilling (LWD) results during Expedition 314 (see the **"Expedition 314 Site C0001"** chapter) and seismic reflection data.

Unit I (slope-apron facies)

Interval: Sections 315-C0001E-1H-1 through 315-C0001F-13H-CC
Depth: 0–207.17 m CSF
Age: Quaternary–late Pliocene
Lithology: silty clay to clayey silt with volcanic ash, silt, and fine sand

The dominant lithology of Unit I is silty clay to clayey silt (Fig. F4; Table T6). Secondary lithologies include thin interbeds and irregular patches of sand, sandy silt, silt, and volcanic ash. Overall, the siliciclastic interbeds define a trend of fining and thinning upward (Fig. F4). During interpretation of LWD data, the comparable boundary between logging

Units I and II was placed at 198.9 m LWD depth below seafloor (LSF).

Subunit IA

Subunit IA extends from 0.00 to 168.35 m CSF. The dominant lithology is greenish gray to grayish green mud (silty clay to clayey silt). The mud is generally structureless, but local wavy laminae are expressed by color change (dark green). Calcareous nannofossils are common to abundant in silty clay intervals; foraminifers, diatoms, and radiolarians are also evident in smear slides (Fig. F5). Bioturbation is patchy and relatively mild in severity (compared to Unit II). Irregular patches of silt and sandy silt are rare. Local zones of contorted bedding are similar to those observed at Ocean Drilling Program (ODP) Sites 1175 and 1176 within the slope-basin facies (Shipboard Scientific Party, 2001a, 2001b).

The most common interbeds within Subunit IA consist of white or light gray to dark gray volcanic ash, which typically displays a sharp base and normal size grading; the upper contacts between ash and silty clay are less distinctive than the bases (Fig. F6). Ash layer thickness ranges from <1 to 25 cm (Fig. F7), and particle size ranges from coarse silt to medium sand. The highest concentrations of ash occur between ~75 and 180 m CSF (Fig. F7). Light-colored ash deposits contain fresh shards of clear volcanic glass and pumice, with minor amounts of fresh, euhedral plagioclase. In contrast, darker ash beds contain more fragments of altered volcanic rock, altered glass (replaced by clay minerals or coated by manganese oxide), crystals of plagioclase and iron-magnesium silicates (e.g., pyroxene and amphibole), and opaque grains.

Subunit IB

Subunit IB extends from 168.35 to 196.76 m CSF. The subunit boundary is defined by the first occurrence of multiple closely spaced silt beds. The dominant lithology is greenish gray to grayish green mud (silty clay to clayey silt), superficially identical to the mud of Subunit IA. Calcareous nannofossils are common to abundant, and bioturbation is relatively mild. Dark gray silt to sandy silt is the characteristic minor lithology of this subunit. These thin beds display sharp bases, faint plane-parallel laminae, normal size grading, and diffuse tops. Such features are typical of fine-grained turbidites. Silt-size grains are composed mostly of quartz, feldspar, sedimentary rock fragments, and opaque minerals.

Subunit IC

Subunit IC extends from 196.76 to 207.17 m CSF. The dominant lithology is gray to dark bluish gray sand, intercalated sporadically with greenish gray to grayish green mud. Grain size varies from silt to medium sand but is predominantly fine sand (Fig. F8). Unconsolidated sand appears to be structureless and soupy, but this is probably an artifact caused by coring disturbance. Bed thickness is impossible to recognize because of flow within the core liner. Sand grains consist mostly of detrital quartz and feldspar with abundant sedimentary and low-grade metasedimentary rock fragments (shale, argillite, chert, and quartz-mica grains) (Fig. F8). LWD data indicate moderate bedding dips within the correlative logging unit.

Interpretation of Unit I

Deposition of Unit I probably occurred in a slope-apron to slope-basin environment. This interpretation is consistent with present-day bathymetry, which features a small depression or topographic bench that was created by uplift along the megasplay fault system. The dominant mechanism of sedimentation was hemipelagic settling of suspended silt, clay, and biogenic constituents. Most of the volcanic ash probably entered the site by vertical settling from air falls, although remobilization by subaqueous gravity flow is also feasible. Local zones of contorted bedding are probably manifestations of soft-sediment folding caused by gravitational failure. The sand beds of Subunit IC are somewhat enigmatic. Turbidity currents were the most likely agents of transport for sand and silt beds. Gravity flows during the early stages of Unit I deposition may have moved down the axis of the trench (i.e., toward the southwest) and lapped onto the landward slope. This transport direction would be consistent with paleoflow data from the Quaternary trench wedge in the Muroto transect area (Pickering et al., 1993a). Alternatively, turbidity currents during the late Pliocene may have moved across the forearc in a transverse direction, funneling sand through small submarine canyons. Detrital provenance analysis will be needed to discriminate between these options. In either case, the delivery of sand and silt gradually dissipated, either because the site rose above the influence of trench floor processes or because the transverse flow paths were blocked or diverted by accretion-related deformation. The interpretation of progressive uplift is reinforced by the distribution of calcareous nannofossils, which increase in concentration upsection. The pattern of fining and thinning upsection is similar to what was observed at ODP Sites 1175 and 1176, within slope basins of the Muroto transect of the Nankai Trough (Shipboard Scientific Party, 2001a, 2001b; Underwood et al., 2003).

Unit II (upper accretionary prism)

Interval: Sections 315-C0001F-14H-1 through 315-C0001H-26R-CC
Depth: 207.17–456.50 m CSF
Age: late Pliocene–late Miocene
Lithology: silty clay to clayey silt with rare volcanic ash, silt, and silty sand

The boundary between Units I and II is an unconformity, with an associated hiatus, as shown by both paleomagnetic data and biostratigraphy. The occurrence of a geometric unconformity is also obvious from seismic reflection and LWD data (see the **"Expedition 314 Site C0001"** chapter). Within Unit II, Expedition 314 shipboard scientists recognized three logging subunits (IIA, IIB, and IIC) (Fig. **F4**). Lithologic variations in the cores, however, are not distinctive enough to warrant division of lithologic Unit II on the basis of texture, composition, or sedimentary structures.

The dominant lithology of Unit II is greenish gray to grayish green bioturbated mud (silty clay to clayey silt). Thin layers of silt or silty sand are rare and limited to cores near the top of the unit. Volcanic ash layers are also rare, thin, and limited to cores near the top of the unit. (Fig. **F7**). Mud contains local wavy laminae, as defined by a darker green color and higher clay content. Concentrations of calcareous nannofossils are significantly lower here than they are within comparable mud deposits of Unit I (Fig. **F5**). Bioturbation, as characterized by the association of *Zoophycos* and *Chondrites,* is moderate to heavy and increases in severity with depth. Pyrite grains are moderate to abundant.

The depositional environment of Unit II is difficult to interpret with confidence. Seismic reflection data indicate that the contact between Units I and II is a boundary between the slope apron and the accretionary prism, which means that the most likely depositional environment prior to accretion is trench wedge. This part of the accretionary prism, however, does not display continuous high-amplitude seismic reflectors, so lithology is evidently homogeneous throughout. Low concentrations of calcareous nannofossils point to a depositional environment below the carbonate compensation depth (CCD), probably near the base of the trench slope. Elsewhere along the Nankai margin, the preponderance of hemipelagic mud is unusual within the trench-wedge environment, although the facies becomes muddier near its seaward margin (Pickering et al., 1993b; Moore, Taira, Klaus, et al., 2001). Farther outboard, the upper Shikoku Basin facies contains abundant beds of volcanic ash, at least where it has been cored in the Muroto and Ashizuri transects (Moore, Taira, Klaus, et al., 2001). Tectonic kneading of the muddy slope apron, or a slope basin between imbricate thrusts, into the accretionary prism is also possible, although the paucity of ash beds and biogenic carbonate argues against this interpretation. Thus, although the match between lithology and environment is not definitive, our preferred interpretation for the depositional setting is outer (marginal) trench wedge during a time interval of low sand-silt influx.

X-ray diffraction mineralogy

Bulk powder X-ray diffraction (XRD) results provide useful constraints on relative abundances of total clay minerals, quartz, plagioclase, and calcite. Data are shown in Figure **F9** and tabulated in Table **T7.** As a measure of accuracy for these estimates, relative to absolute percentages, we completed regression analysis of percent calcite from XRD versus percent calcium carbonate from coulometric analysis (see **"Organic geochemistry"**). For XRD relative values above ~10%, this comparison shows a progressive overestimation of calcite relative to the coulometric data, which is to be expected if the coulometric concentration is expressed as a percentage of the total solid mass (weight percent) (Fig. **F10**). Conversely, the XRD method underestimates relative percent calcite for absolute values below ~5%, and the detection limit for calcite is ~3% (true weight percent).

Values of quartz (XRD) at Site C0001 range from 10.2% to 28.2%. Average relative values are 20.3% and 20.6% for Units I and II, respectively. Relative percentages of plagioclase vary between 11.2% and 38.5%. Unit I contains an average of 19.6% plagioclase, whereas Unit II contains an average of 15.6%. Relative concentrations of total clay minerals are between 28.3% and 67.6%. Total clay significantly increases in Unit II (average = 62.5%) compared to Unit I (average = 42.9%). Calcite shows the largest stratigraphic variation, and its abundance is controlled mostly by the concentration of calcareous nannofossils. Unit I contains between 1.7% and 45.9% calcite (average = 17.2%), whereas relative values in Unit II drop from 9.0% to 0.0% (average = 1.3%). This shift in composition across the unit boundary is consistent with uplift of the depositional site from below the CCD (Unit II) to above the CCD (Unit I). The same compositional trend is evident at ODP Sites 1175 and 1176 across the same type of facies change (Shipboard Scientific Party, 2001a, 2001b; Underwood et al., 2003).

Structural geology

The main goal of the structural geologists during Expedition 315 was to describe and document the style, geometry, and kinematics of structural features observed in the cores. Drilling at Site C0001 retrieved >450 m of core from three holes (C0001E, C0001F, and C0001H), and drilling during Expedition 314 retrieved an additional 30 m of core at this site from Hole C0001B (0–32 m CSF) that were also described by Expedition 315 scientists. Although the total drilling depth at Site C0001 was shorter than the planned total depth of 1000 mbsf, >550 individual structural features, including 135 bedding measurements, were documented and described. Hole C0001H (the deepest hole cored at this site) also yielded the largest number and greatest variety of structures, although geologic structures and bedding measurements from Holes C0001B, C0001E, and C0001F provided additional information critical to understanding regional kinematics. Drilling-induced structures, identified primarily in Hole C0001H, were also documented. Many structural features were also reoriented to a geographic reference frame using shipboard paleomagnetic data. Overall, structural data show significant changes with depth, particularly above and below a zone of deformation that occurs 15–20 m below an unconformity that separates the slope apron from the underlying sediments thought to have originated on the ocean floor of the Philippine Sea. Kinematics derived from structures at Site C0001 confirm and expand upon the orientations of stresses obtained from LWD data during Expedition 314.

Types of structures

A range of planar deformation structures was observed in Expedition 315 cores. Most could be classified as belonging primarily to one of three types of structures: faults, shear zones (or deformation bands), or "vein structures." This classification is not meant to imply that all structures were only one type—in fact, many structures showed features characteristic of all three types—but at this preliminary stage, and with limited thin section and other microscopic analyses, we chose to use a limited number of broader categories. Descriptive modifiers and sketches provide additional information on the similarities and differences of individual structures.

Faults

Faults are relatively planar, narrow zones of deformation characterized by a single band of concentrated deformation at the scale of the core and CT images. Faults also show clear evidence of displacement, including offset markers (e.g., bedding, burrows, or small pumice fragments), fault drag, and slickensided rough or polished surfaces (Fig. **F11A, F11C, F11D**). They are also typically slightly bright in CT images, suggesting a higher density than the adjacent wall rock (Fig. **F11B**).

Shear zones

Shear zones (or deformation bands) are generally wider (>2 mm) than faults and are often composed of multiple sets or bands of concentrated deformation (Fig. **F12A**). In many cases, the outer edges of a shear zone are sharp and more planar than the anastamosing surfaces of deformation within the zone. CT images also suggest a range of densities within individual zones and between different shear zones (Fig. **F12B**). On the cut surfaces of cores, shear zones commonly appear darker than wall rock (Fig. **F12C**), and in thin section, phyllosilicates display a range of crystallographic preferred orientations (CPOs), from well-developed bands to distributed clusters of phyllosilicates with different CPOs in different parts of the same thin section (Fig. **F12D**).

Vein structures

Vein structures include a variety of structures, many of which have been identified on previous ocean drilling expeditions and interpreted as dewatering structures. This category of structures includes the classic sigmoidal-shaped suite of thin, mud-filled veins that are slightly darker than the surrounding materials and first documented by Ogawa (1980) and Cowan (1982), as well as other veinlike structures that appear darker (Fig. **F13**) than the surrounding sediment and slightly brighter (or denser) in CT images (Fig. **F13C**). These other veinlike structures include single planar to subplanar features that are several millimeters thick but associated with only limited displacements and rare to poorly developed slickenlines. Dark veins are often spaced at regular intervals in the horizontal plane (Fig. **F13A, F13B**). In some cases, veinlike structures extend subparallel to the core axis for decimeters; in other cases, they occur at moderate to low angles to the core axis with limited extent. Apparent offsets across these structures in the split core indicate mostly normal displacements (Fig. **F13B**).

Steepened bedding

Steepened bedding is an important and relatively sensitive indicator of deformation. Seismic reflection studies and LWD data suggest that bedding dips were relatively shallow in the upper 500 m in the area of this site, although dips as steep as ~50° were documented at ~200 m LSF. These findings were largely corroborated during Expedition 315 through core and CT image logging efforts, although some important differences emerged, as described below.

Breccia

Breccia is marked by a relatively high concentration of small polished and slickenside, lens-shaped fragments of clayey silt or silty clay. Zones of breccia range in thickness from a few centimeters to 1 or 2 dm and are often associated with zones of poor recovery. Breccia was recognized at 160–170 and 218–220 m CSF.

Kink bands

Only two occurrences of kink bands were documented (Korig and Lundberg, 1990). More detailed analysis may show, however, that some of the structures classified as faults or shear zones evolved from kink or kinklike structures.

Drilling-related structures

Drilling, particularly with the RCB in Hole C0001H, induced a range of styles of fractures and slickensided surfaces that in some cases appeared to be very similar to small faults and in other cases overprinted preexisting faults or shear zones. Fractures that appeared to be clearly related to drilling ranged from planar surfaces perpendicular to the core axis and displaying concentric or circular slickenlines to conspicuous cones or “witch hats” that point vertically up in the core reference frame. Planar features, in addition to circular slickenlines, display unusually flat and polished surfaces. Cone-shaped fractures, in contrast, often expose broken and only slightly polished surfaces, and slickenlines, if present, spiral up the sides of the cone. In cases where drilling-induced slip occurs on preexisting faults or shear zones, faulted surfaces appear unusually smooth and polished, similar to the polished surfaces with circular slickenlines. Reactivation of preexisting faults was also interpreted based on kinematic analysis, as described below, and a selection of these kinematically identified faults showed some of the features associated with clearly drilling-induced faults (e.g., unusually smooth and polished surfaces).

Distribution of structures

Figures F14 and F15 show the distribution and dip of the dominant deformation structures at Site C0001 and highlight both the heterogeneity of deformation throughout the site and the dominance of structures at or below a zone of breccia and concentrated deformation at ~220 m CSF.

Bedding generally dips gently with only three anomalous zones: ~80–100, 140, and ~200–205 m CSF (Fig. F14). Each of these zones of increased bedding dip also appears to generally correlate with structural features identified at Site C0001. For example, the zone between 80 and 100 m CSF occurs just above an interval of slumping documented in the lithology, whereas the cluster of increased bedding dips at ~140 m CSF correlates with a possible normal fault suggested by an apparent offset of seismic reflectors (Fig. F15) and is likely related to a breccia zone at 160–170 m CSF, as well as a cluster of normal faults at 150–160 m CSF (Fig. F14). Bedding-dip directions in the interval 140–205 m CSF are also significantly more organized than elsewhere, ranging from ~270° to 360° (Fig. F14). Finally, the well-defined zone of steepened bedding at 200–205 m CSF occurs just above the Unit I/II boundary and the zone of concentrated deformation suggested by clusters of shear zones and normal faults (Figs. F14, F15).

Shear zones are present almost exclusively below the Unit I/II boundary and form three groups with different dip magnitudes: very gently dipping, moderately dipping, and steeply dipping (Fig. F14). Moderately dipping shear zones dip ~50°, are present just below the Unit I/II boundary and correlate with a cluster of moderately deepening normal faults at the same depth interval. Very gently dipping and steeply dipping shear zones have mean dips of 15° and 80°, respectively, and occur below ~240 m CSF (Fig. F14).

Faults are generally present at all depths at Site C0001, but only normal faults and a few relatively minor thrust faults occur above ~220 m CSF. Clusters of normal faults occur from 150 to 160 and 220 to 240 m CSF (Fig. F14), and both clusters are associated with breccia zones. Normal faults above ~240 m CSF have steep to moderate dips similar to the cluster of shear zones at the same depth (Fig. F14). Below ~240 m CSF, the range of dip magnitudes increases, although many of the normal faults have relatively steep dips (e.g., 80°), which is also similar to the dip of the shear zones below this depth (Fig. F14). Both thrust and strike-slip faults have a range of dip magnitudes (Fig. F14).

Geometry and crosscutting relationships

In the most deformed sections of Hole C0001H, structures have been found in association with one another, allowing sense of movement and crosscutting relationships to be established. As a general rule, the oldest structures observed are shallow-dipping (<30°) black shear zones. In most cases, sense of shear could not be determined for these shear zones, although based on rare shear sense indicators, it seems that some of them might have a thrust offset.

These shallow-dipping shear zones are commonly cut by steeper (>60°) dark-colored shear zones. Steeper shear zones are often observed to merge by coalescence of several thin black "dewatering" veins. At the hand specimen scale, steep shear zones display both reverse and normal offsets, but normal offsets are more frequently observed and are consistent with the microscale normal movement of dewatering veins (see thin bed at middle of Fig. **F13B**).

Shear zones and dewatering structures are systematically cut by faults, indicating that the faults are younger. The fact that faults are not filled with black material indicates either that these structures are too recent for chemical alteration to have occurred or that interstitial fluid chemistry has changed since the black deformation structures formed. Alternatively, these differences may reflect fundamentally different grain scale micromechanical processes (e.g., dilational versus compactive processes). Normal and thrust faults display mutually crosscutting relations, and both are crosscut by shallow-dipping strike-slip faults.

Kinematics

Using shipboard paleomagnetic data, ~30% of the planar structures were reoriented to true north. The remaining data could not be reoriented because of extensive whole-round sampling, relatively strong drilling-related magnetic overprint, and drilling-related disturbances. Reoriented data provide key insights into the state of stress in sediments cored at Site C0001.

Fault orientations are strongly contrasted above and below the highly deformed zone at ~220 m CSF. Above this zone, ~90% of the faults described are sets of normal faults dipping at 60° either northeast or southwest (Fig. **F16A**). These normal faults are consistent with a vertical maximum principal stress (σ_1), a minimum principal stress (σ_3) oriented northeast, and an intermediate principal stress (σ_2) oriented southeast (Fig. **F16B**). Deformation in the slope apron is therefore dominated by extension subparallel to the trench. Stress state is consistent with both seismic reflection profiles that show steep, northwest-striking normal faults (see Fig. **F2** in the "Expedition 314 Site C0001" chapter) and borehole breakout data that show a north-northwest–trending maximum horizontal stress (see the **"Expedition 314 Site C0001"** chapter). A few moderately dipping thrust faults were also encountered above 220 m CSF. Fault kinematics (corrected for drilling-induced rotations) indicate northwest–southeast shortening subparallel to the direction of plate convergence (Fig. **F17**).

The geometry and kinematics of planar structures display greater variation below ~222 m CSF than above it (Figs. **F18, F19, F20, F21**). Nonetheless, kinematic analyses computed from normal (Fig. **F18B**) and thrust faults (Fig. **F19**) are respectively consistent with northeast–southwest extension and northwest–southeast shortening, as observed in the slope apron.

Strike-slip faults only occur below ~220 m CSF and display heterogeneous kinematics, including an unusually large number of low-dipping fault planes. Stereographic projections of fault planes and associated slickenlines, along with tangent lineation diagrams where the pole to the fault and the movement of the footwall relative to the hanging wall are shown, however, suggest two populations of faults (Figs. **F20, F21**). One population contains faults dipping <50° and records a clockwise sense of motion for the hanging wall relative to the footwall (Fig. **F20B**), which is the same sense of motion as the drilling pipe during drilling on the *Chikyu*. These faults also generally strike north–south (Fig. **F20A**). The second set contains more steeply dipping faults (generally >50°) and shows northwest–southeast shortening. Fault surfaces of the low-dipping strike-slip faults also appear to have more irregular steps than true tectonic faults. Consequently, we interpret the set of low-dipping strike-slip faults to be preexisting faults reactivated as strike-slip faults during drilling. The fact that shallow-dipping strike-slip faults crosscut all other structures supports this interpretation. After removal of shallow-dipping faults, the remaining steep strike-slip faults yield a kinematic solution consistent with the northwest–southeast shortening and northeast–southwest extension (Fig. **F21**) inferred from the other faults (Figs. **F18B, F19B**).

Discussion

The superposition of normal, thrust, and strike-slip faults as observed in the deeper sections of Site C0001 may have a number of causes. One possibility is that as the sediments moved through the accretionary prism and away from the trench the overburden-induced (i.e., vertical) stress became proportionally more important. This may have involved reorientation of σ_3 from vertical to horizontal and northeast trending (Fig. **F22**) and a reorientation of σ_1 from northwest trending to vertical. This interpretation would explain, in particular, why older sediments of the accretionary prism are affected by faults with a range of kinematics, whereas the slope apron is mostly deformed by extension. Alternatively, principal stress permutations could be caused by increases and decreases of the northwest–southeast plate convergence stress related to the Nankai seismic cycle. This would explain the absence of clear overprinting relations between fault types. A third possibility is that differential stresses are small and minor local perturbations of the stress field are the cause of stress permutations and resulting diversity of fault types.

Structural data collected from Site C0001 cores provide a critical third dimension to the stress data obtained from LWD during Expedition 314, especially for stress orientations in the sediments of the slope apron. For example, borehole breakouts observed in LWD logs consistently show that σ_{Hmax} trends northwest–southeast at least in the uppermost 500 m of the hole where the breakouts were observed. This trend for σ_{Hmax} is approximately perpendicular to the plate margin, suggesting that it represents σ_1. Site C0001 core-based structural data show, however, that the uppermost 200 m (i.e., the sediments of the slope apron) are dominated by normal faults that trend north-northwest. These data suggest that σ_1 is vertical rather than horizontal and that σ_2 is equivalent to σ_{Hmax}, which trends perpendicular to the margin. Thus, relative magnitudes of the horizontal stresses interpreted from the LWD borehole breakout data are consistent with the fault data, but actual principal stresses can only be deduced from fault kinematics.

The extension direction interpreted from normal faults in the slope apron (i.e., margin parallel) also contrasts with the extension direction interpreted from Site C0002 borehole breakout data, which show margin-perpendicular extension. The regional significance of this change across the margin from shelf to accretionary prism will be part of our postcruise research program, but these preliminary data suggest Site C0001 may represent the transition from horizontal compression near the trench to horizontal extension on the shelf.

The consistent trend of σ_h determined from borehole breakout data at Site C0001 suggests continuity of stresses throughout the hole, although the uppermost 200 m may be dominated by gravitationally driven slope stresses, whereas the lower few hundred meters are dominated by tectonic stresses. The vertical transition from gravitationally driven to tectonically driven stresses may therefore reflect the change in magnitudes of these stresses with depth.

Biostratigraphy

Calcareous microfossils belonging to two major groups, nannofossils and planktonic foraminifers, were recovered from the sedimentary succession at Site C0001 in the trench slope basin, off the Kumano coast of Honshu Island, in the northwest Pacific Ocean. Combined biostratigraphic results suggest at least one time break in the sequence from the late Quaternary to the Miocene/Pliocene boundary (Fig. **F23**).

Foraminifers and nannofossils are generally abundant within lithologic Subunit IA, with preservation ranging from moderate to good; the most well-preserved assemblages are found in the Pleistocene. Sedimentation rates are relatively high in Subunit IA, ranging from 140 to 180 m/m.y. (Fig. **F23**). In Unit II, which spans the accretionary prism sediments, sedimentation rates are difficult to pinpoint because of the lack of reliable biostratigraphic events. However, preliminary results suggest sedimentation rates between 31 and 44 m/m.y. (Fig. **F23**). The Pliocene/Pleistocene boundary is placed between Sections 315-C0001F-9H-CC and 10H-CC based on planktonic foraminiferal evidence (last occurrence [LO] of *Neogloboquadrina asanoi*). Definite Pliocene nannofossil assemblages are present in Sample 315-C0001F-10H-CC, 37–42 cm, and correspond well to foraminifers. A marked change in both nannofossil and foraminifer assemblages occurs in Sections 315-C0001F-13H-CC through 14H-CC, spanning the interval between 207.16 and 213.27 m CSF. Here, mixed assemblages of late Pliocene to late Miocene age were encountered. In Samples 315-C0001F-19H-CC, 33–38 cm, and 315-C0001H-1R-CC, 26–31 cm, microfossil assemblages indicate an early Pliocene age.

The Miocene/Pliocene boundary is placed below Section 315-C0001H-21R-CC based on foraminiferal evidence. Nannofossil results, however, suggest that the boundary is located between Section 315-C0001H-24R-CC and the bottom of Hole C0001H. The exact position of the Miocene/Pliocene boundary at Site C0001 remains equivocal and warrants more detailed investigation.

Generally, the applicability of nannofossil zonation based mostly on low-latitude records benefits from the Kuroshio Current transporting warm equatorial surface waters to higher latitudes. Therefore, most samples studied here contain subtropical species within the Pliocene and Miocene intervals. However, there are indications that downhole variations in microfossil assemblage composition are partly invoked by regional paleoenvironmental changes. Early Pliocene to late Miocene planktonic foraminiferal assemblages exhibit low species diversity, and their downhole distribution is patchy, with several barren samples. A particularly poor interval in terms of nannofossil preservation and abundance stretches from Sections 315-C0001H-7R-CC to 10R-CC (296.64–

319.95 m CSF). The interval is characterized by elevated numbers of the subarctic species *Neogloboquadrina pachyderma* sinistral form, indicating the presence of cooler water masses.

Calcareous nannofossils

All core catcher samples plus additional samples from some critical intervals in the vicinity of zonal boundaries were examined for calcareous nannofossils at Site C0001. Calcareous nannofossils are generally abundant and well to moderately preserved throughout the slope sediments (lithologic Unit I; Table T8). In contrast, within the accretionary prism sediments (Unit II) nannofossil abundance is generally low with moderately to mostly poorly preserved specimens (Tables T9, T10). Several samples from the lower Pliocene section yield only few or no nannofossils. A total of 15 nannofossil biostratigraphic events recorded at Site C0001 are listed in Table T11.

In Hole C0001B, two nannofossil events were recognized that assign its entire sedimentary succession a Pleistocene age. The first occurrence (FO) of *Emiliania huxleyi,* which defines the base of nannofossil Zone NN21 at 0.291 Ma, was placed between Samples 314-C0001B-1H-CC, 0–5 cm, and 2H-CC, 0–5 cm (2.11–11.86 m CSF). The LO of *Pseudoemiliania lacunosa* is located between Samples 314-C0001B-2H-CC, 0–5 cm, and 3H-CC, 15–17 cm (11.86–22.06 m CSF), marking the top of nannofossil Zone NN19.

In Hole C0001E, the first event recognized was the crossover in abundance from *E. huxleyi* to *Gephyrocapsa* spp. (>3.5 µm) between Samples 315-C0001E-1H-2, 10 cm, and 1H-3, 38 cm (0.17–1.83 m CSF). The FO of *E. huxleyi* was found between Samples 315-C0001E-1H-3, 38 cm, and 1H-5, 18 cm (1.83–3.02 m CSF). The concentration of several biostratigraphic events within the first core spanning a time interval between 63 and 291 ka might be indicative of a condensation horizon in the upper part of the core. The base of Zone NN20 at 0.436 Ma is defined by the LO of *P. lacunosa,* located between Samples 315-C0001E-2H-6, 16.5 cm, and 2H-7, 16.5 cm (10.10–11.50 m CSF). The last consistent occurrence of *Reticulofenestra asanoi* (0.9 Ma) was found between Samples 315-C0001E-7H-2, 80 cm, and 7H-5, 75 cm (53.63–57.58 m CSF). Zone NN19 was further divided by biohorizons based on changes in occurrences of different sized *Gephyrocapsa.* The reentrance of *Gephyrocapsa* spp. (>4 µm) is recorded between Samples 315-C0001E-8H-CC, 48 cm, and 9H-CC, 31.5 cm (68.07–80.10 m CSF). The LO of *Gephyrocapsa* spp. (>5.5 µm) provides another datum level of 1.24 Ma between Samples 315-C0001F-3H-CC, 51–56 cm, and 4H-CC, 12.5–17.5 cm (131.97–145.95 m CSF).

The LO of *Calcidiscus macintyrei* was found between Samples 315-C0001F-6H, 23.5 cm, and 7H-CC, 71–76 cm (161.50–170.98 m CSF). Frequent reworking of discoasters in the interval above blurs the exact identification of the zonal base of NN19. However, in accordance with magnetostratigraphy the LO of *Discoaster brouweri,* which occurs below the Pliocene/Pleistocene boundary, is placed between Samples 315-C0001F-9H-CC, 27.5–32.5 cm, and 10H-CC, 37–42 cm (189.24–195.79 m CSF). In the latter sample, well-preserved *D. brouweri* specimens were detected.

Nannofossil content is generally low, and nannofossil preservation is poor within Samples 315-C0001F-10H-CC, 37–42 cm, through 13H-CC, 20–25 cm. This sandy interval is referred to as logging Subunit IB, marking the contact between the overlying slope apron sediments and the upper accretionary prism according to seismic and log interpretation.

Samples below the sandy layers yield a mixed and rather poorly preserved nannofossil assemblage with *Gephyrocapsa* spp. (>3.5 µm), the occurrence of which is restricted to the upper Pliocene, and older nannofossils with LOs positioned in the upper to middle Pliocene, such as *Discoaster pentaradiatus, Discoaster surculus, Discoaster variabilis, Sphenolithus* spp., and *Reticulofenestra pseudoumbilicus* (>7 µm). In contrast, the nannofossil assemblage present in Sample 315-C0001F-18H-5, 33–38 cm, is mainly composed of abundant *Reticulofenestra* spp. as the dominant placoliths, *D. brouweri, D. pentaradiatus, D. surculus, D. variabilis,* and *Sphenolithus abies*. This assemblage is regarded as typical for Zones NN15 to NN12, which span the interval from 3.79 to 5.59 Ma. The LO of *R. pseudoumbilicus* (>7 µm) at 3.79 Ma was found between Samples 315-C0001F-17H-CC, 13–18 cm, and 18H-CC, 0–1 cm (220.31–226.18 m CSF). Therefore, these sediments are assigned at least an early Pliocene age. This age assignment implies a biostratigraphic gap of at least 1.8 m.y. between the lowermost slope sediments, which are ~2 Ma, and the accretionary prism sediments, which are early Pliocene in age.

The uppermost core catcher sample of Hole C0001H contains basically the same assemblage as that recognized in Sample 315-C0001F-19H-5, 33–38 cm, recovered from Hole C0001F. Nannofossil abundance is generally low in sediments recovered from Hole C0001H, and their preservation is often poor. Dissolution and overgrowth affected the assemblage to a minor degree, whereas mechanical breakage was more severe, especially with respect to discoasters, which made species assignment sometimes difficult. The genera *Amaurolithus* and *Ceratolithus* provide important marker species for dividing the lower Pliocene nannofossil zones. However, these marker species appear only in low numbers in Hole C0001H, which impairs their biostratigraphic usefulness. *Ceratolithus acutus* was first recorded in Sample 315-C0001H-17R-CC, 0–5 cm (380.83 m CSF). This species occurs last at 5.04 Ma. One *Amaurolithus primus/Amaurolithus delicatus* intergrade was first observed in Sample 315-C0001H-22R-2, 139–140 cm. The LO of *A. primus* at 4.5 Ma is placed between Samples 315-C0001H-21R-CC, 0–5 cm, and 22R-2, 139–140 cm (417.85–422.32 m CSF). The FO of *Ceratolithus rugosus,* which defines the base of Zone NN13 at 5.12 Ma, was placed between Samples 315-C0001H-22R-CC, 0–5 cm, and 23R-CC, 29–34 cm. *C. acutus* appears sporadically downhole to Sample 315-C0001H-25R-CC, 0–5 cm. Because of its rare occurrence, the placement of the FO of *C. acutus* between Samples 315-C0001H-25R-CC, 0–5 cm, and 26R-CC, 0–5 cm (449.53–456.55 m CSF), is questionable. Yet this species is confined to a relatively short stratigraphic interval between 5.04 and 5.32 Ma, providing a good biostratigraphic approximation of the Miocene/Pliocene boundary, which is generally located slightly above the FO of *C. acutus.*

Planktonic foraminifers

All core catcher samples and 13 additional core samples within stratigraphically important intervals were examined. Planktonic foraminifers successively occurred in Holes C0001B, C0001E, C0001F, and C0001H, with the exception of several barren samples. Fossil abundance and preservation are generally excellent within the upper interval of the slope apron deposits (lithologic Unit I). In contrast, sediments of the lower accretionary prism (lithologic Unit II), recovered from the lower part of Hole C0001F to Hole C0001H, show relatively low numbers of fossil foraminifers with moderate to poor preservation. Some samples are even barren. These barren samples include only thick-walled benthic foraminifers such as *Amphicoryna* spp. with dissolved surface structures. Therefore, the discontinuous occurrence of planktonic foraminifers in the lower part of Hole C0001F could be due to dissolution of their more delicate shells, which might be related to a depositional environment below the CCD. Stratigraphic distribution of selected species is given in Tables **T12, T13,** and **T14.**

The planktonic foraminiferal assemblage significantly changes around the boundary between lithologic Units I and II: the upper assemblage of Unit I is characterized by dominant occurrences of temperate to cosmopolitan taxa such as *Neogloboquadrina, Globigerina,* and *Globoconella*. Tropical to subtropical genera such as *Globogerinoides, Globorotalia,* and *Pulleniatina* exhibit a continuous record. In contrast, the lower Unit II comprises relatively cool assemblages mainly consisting of *Neogloboquadrina* spp. and *Globigerina bulloides*. Noteworthy features of the foraminiferal record are cyclic variations in species composition within Unit II. In particular, the dominant coiling direction of *N. pachyderma* changes every 20–40 m in the lower sequence of Hole C0001H. These cyclic variations might result from changes in paleoclimatic conditions.

A total of 14 biohorizons are recognized at Site C0001 (Table **T15**). *Globigerinoides ruber rosa* continuously occurs between Samples 315-C0001E-1H-3, 81–83 cm, and 2H-5, 14–18 cm. The LO of this species (0.12 Ma) is recognized between Samples 315-C0001E-1H-2, 36–40 cm (0.47 m CSF), and 1H-3, 81–83 cm (2.27 m CSF). In Hole C0001B, this biohorizon is located above Sample 314-C0001B-1H-CC, 0–5 cm (2.11 m CSF), which is in good accordance with the results of Hole C0001E. *Truncorotalia tosaensis* continuously occurs from the lower to middle part of Hole C0001E, and its LO (0.61 Ma) is recognized between Samples 315-C0001E-2H-CC, 46–51 cm, and 3H-CC, 23–28 cm. However, the sporadic presence of reworked specimens in this interval, such as the early Pleistocene species *Globoturborotalita obliquus* (LO = 1.30 Ma) and *Truncorotalia crassaformis viola* (LO = around the base of the Pleistocene), might indicate that the actual LO of *T. tosaensis* should be located further downhole. Thus, its LO only serves as a maximum age estimate. Four samples from Hole C0001E contain *Truncorotalia crassaformis hessi*. The FO of this species (0.81 Ma) is placed below Sample 315-C0001E-6H-CC, 32.5–37.5 cm (51.60 m CSF). However, the precise position of the FO remains uncertain because of the sporadic occurrence of the species. Moreover, previous research has already mentioned that the FOs of several *Truncorotalia* species are generally delayed in mid-latitudes (Brunnes et al., 2002). At the present site, the FOs of *Truncorotalia truncatulinoides, T. tosaensis,* and *T. crassiformis* lag behind other foraminiferal events.

The FO of *T. truncatulinoides* (1.93 Ma) is detected between Samples 315-C0001F-2H-CC, 22–27 cm (127.00 m CSF), and 3H-CC, 51–56 cm (131.97 m CSF), and defines the base of Zone N22. The change in coiling direction (SD) of *Pulleniatina* spp., mainly *Pulleniatina obliquiloculata* and *Pulleniatina primalis,* from sinistral to dextral is recorded twice. The lower SD1 at 4.08 Ma occurs between Samples 315-C0001F-14H-CC, 0–5 cm (213.27 m CSF), and 315-C0001H-1R-CC, 26–31 cm (234.24 m CSF). The upper event (SD2 at 1.7–1.8 Ma) lies between Samples 315-C0001F-6H-CC, 21–26 cm (161.50 m CSF), and 7H-CC, 71–76 cm (170.98 m CSF). *N. asanoi* occurs abundantly in Sample 315-C0001F-10H-CC, 37–42 cm (195.79 m CSF), and the LO of this species (1.8 Ma) is placed above this sample. The FO of *T. tosaensis* (3.35 Ma) is located between Samples 315-C0001F-12H-CC, 18–23 cm (202.34 m CSF), and 11H-CC, 13–18 cm (200.85 m CSF). This event determines the lower boundary of Zone N21.

Between Samples 315-C0001F-13H-CC, 20–25 cm (207.16 m CSF), and 14H-1, 125–129 cm (208.45 m CSF), three biohorizons of different ages are detected—namely, the FO of *Globoconella inflata* modern form (2.3–2.5 Ma), the LO of *Sphaeroidinellopsis seminulina* s.l. (*Sphaeroidinellopsis subdehiscens* of the present author), and the LO of *Dentoglobigerina altispira* (3.47 Ma). The species concept of *S. seminulina* in Gradstein et al. (2004) is based on Kennett and Srinivasan (1983) and includes *S. seminulina* and *Sphaeroidinellopsis* of the present author. Therefore, the LO of *S. seminulina* s.l. of the present study corresponds to the LO of *S. seminulina* of Gradstein et al. (2004) (3.59 Ma). This interval corresponds to the lithologic boundary between Units I and II. With respect to foraminifer ages, the sedimentation gap between Units I and II should be at least 1.09 m.y.

The assemblage of Sample 315-C0001F-17H-CC, 13–18 cm, which is composed of soft mudstone with heavily disturbed bedding, contains species of different ages. Well-preserved specimens of *T. truncatulinoides, G. ruber rosa,* and *G. inflata* modern form indicate a latest Pleistocene age. However, yellowish-colored specimens of *Sphaeroidinella dehiscens, G. obliquus,* and *Globoconella puncticulata,* which are stratigraphically confined to the early Pliocene, are also observed. This implies that Section 315-C0001F-17-CC is contaminated with late Pleistocene sediments.

The FO of *T. crassaformis* (4.31 Ma) is placed between Samples 315-C0001F-18H-CC, 0–5 cm (226.18 m CSF), and 20X-CC, 49.5–54.5 cm (239.33 m CSF). The LO of *Globoturborotalita nepenthes* occurs between Samples 315-C0001H-1R-CC, 26–31 cm (234.24 m CSF), and 2R-CC, 0–5 cm (246.33 m CSF). Samples obtained from lithologic Unit II generally include specimens showing different ages, especially late Miocene to early Pliocene species of *Globoconella* (*Globoconella conoidea, Globoconella conomiozea,* and *Globoconella sphericomiozea*), which are often recognized within Unit II. The problem remains unsolved as to whether the morphotypes are reworked or represent regional phenotypes. The zonal marker species *Globorotalia tumida* appears sporadically, and its bottom occurrence is in Sample 315-C0001H-21R-CC, 0–5 cm (417.85 m CSF). It therefore indicates a maximum age of 5.57 Ma for this sample. This biohorizon also defines the lower boundary of Zone N.18. In addition, the lowermost sample of Hole C0001H, Sample 315-C0001H-26R-CC, 15–20 cm (456.68 m CSF), contains *Pulleniatina primalis*. Therefore, the sample is younger than the FO of *P. primalis* that defines the base of Subzone N.17b at 6.4 Ma.

Paleomagnetism

Paleomagnetic directions

Archive-half core sections from Holes C0001E, C0001F, and C0001H were measured on the shipboard pass-through cryogenic magnetometer, except for a few sections where sediments were severely disturbed by drilling or flow-in. Natural remanent magnetization (NRM) was measured at 5 cm intervals in each core section, followed by alternating-field (AF) demagnetization at 5, 10, 15, and 20 mT peak fields. Occasionally we opted to reach higher AF fields on short core segments from Hole C0001H that were of particular interest for structural geology. In this case, the goal was to obtain a more reliable magnetization direction based on principal component analysis after analysis of demagnetization (Zijderveld type) diagrams (Zijderveld, 1967). Only a few discrete samples were taken at this stage. Most of the measured cores displayed directions biased toward steep inclinations. After AF demagnetization at 20 mT, magnetic inclination agrees with the expected value (~52°) (Fig. **F24**). Such steeper NRM inclinations are indicative of drilling-induced overprint, typically observed in ODP/IODP studies. The overprint can be generally removed after AF demagnetization at 5–20 mT, although we observed that cores obtained with the RCB often showed a more resistant overprint and required higher AF fields to overcome. Figure **F25** shows the overall trend of both NRM and magnetization after 20 mT, which shows a decrease of quite a large proportion in intensity. For characteristic remanent magnetization (ChRM), in order to establish a magnetic reversal stratigraphy, we used the directions obtained after blanket demagnetization at 20 or 30 mT, following standard ODP/IODP procedures. Note that sometimes the magnetic directions do not reach a stable endpoint at the highest demagnetization value used, suggesting that the primary magnetization has been only partially isolated. A more reliable ChRM by vector analysis is planned with shore-based measurements.

Hole C0001H produced paleomagnetic results more difficult to interpret. We believe that there are basically two issues related to the data set quality. On one hand, a magnetic overprint, typically the type that is drilling induced (i.e., steep and downward), is widespread in cores from Hole C0001H (obtained with the RCB). On the other hand, and because of

RCB coring, there are numerous cores that show biscuiting. Measuring nonuniformly magnetized cores (i.e., because of biscuiting or a polarity transition) with the pass-through magnetometer produces steeper magnetic inclinations and very scattered declinations (e.g., Shipboard Scientific Party, 2002). Reliable declination and inclination values can be inferred only when measurements are consistent across an interval longer than the sensing region of the superconducting rock magnetometer (SRM) coils (20 cm). Consequently, in our data interpretation we excluded all cores from Hole C0001H which show biscuits too short for the pass-through magnetometer. Seemingly homogeneous cores have been included, as well as cores for intervals of particular interest, because of the appearance of tectonic microstructures. We took two different approaches. If a section contained biscuits longer than 20 cm, they were measured one at a time in order to avoid a convoluted signal. Alternatively, some sections were measured as usual, but in the analysis we averaged directions that correspond to the center of biscuits longer than 20 cm.

Core orientation

Declinations obtained from archive-half core pieces were fundamental in core orientation corrections and structural analysis (See **"Structural geology"**). After AF demagnetization of each section, visual inspection of the Zijderveld diagrams allowed us to determine whether the end vector at the highest AF level (typically 20 mT) could be used as the representative paleomagnetic direction for a given interval. If so, paleomagnetic directions were grouped by section and a mean direction was computed with the associated statistical parameters (Table **T16**). In addition, a number of biscuit fragments were selected for more complete AF demagnetization analysis in order to isolate reliable paleomagnetic directions. On these fragments, the AF peak was 80 mT and the characteristic remanent magnetization component direction was calculated using principal component analysis (program "pca;" Tauxe, 1998), guided by visual inspection of orthogonal demagnetization plots (program "plotdmag;" Tauxe, 1998).

There are three basic assumptions in using paleomagnetic directions to determine the core azimuth. First, the direction of the ambient field in which the remanence was acquired is known. Rocks sampled during Expedition 315 are young enough for Earth's magnetic field to be modeled satisfactorily by a geomagnetic axial dipole (Quaternary to Neogene). Average inclinations in Holes C0001E and C0001F are 49.7° for positive inclination and –44.2° for negative inclination (Fig. **F26**), so the expected inclination (52°) for the present latitude of the Nankai Trough is only slightly underestimated. The phenomenon of inclination shallowing is well known in sediments, and it often produces anomalies of up to 15° and occasionally more (King, 1955; Tauxe and Kent, 1984; Garcés et al., 1996). Overall, it seems reasonable to take geographic north as the reference direction. Second, the time interval represented by a sample is sufficiently long for geomagnetic secular variation to be averaged. Third, bedding is horizontal or subhorizontal.

We are aware of the response value of the SRM pickup coils, estimated to be ~20 cm, and know that only measurements taken every 20 cm are truly independent from each other. Hence, for more precise orientation studies, it is recommended to analyze discrete samples based on shore measurements.

Core twisting

We often noticed a change in magnetic declinations along the core, referred to here as core twisting, in Holes C0001E and C0001F (Fig. **F27**). Core twisting was observed because of the reference lines scribed along the liners before they were placed into the barrel. Some cores (e.g., 315-C0001H-7F) for which liners were visibly twisted after removal from the barrel show extremely rotated declinations, documenting such a phenomenon (Fig. **F28**). We also documented core twisting in many cores for which liners were undeformed and where sediment was seemingly intact. In these cases, we see conspicuous declination changes with depth, which reveal a progressive rotation of the core; degree of rotation is variable.

The severity of twisting likely depends on several factors, and we did not observe a particular trend. The most extreme example is Section 315-C0001F-7H-4 (Fig. **F28**), where from top to bottom the core experienced rotation of about two and a half turns (Movie **M1**). Be that as it may, the striking dispersion of declinations documents core twisting between or even within sections and needs to be further examined in future expeditions, as it is typically assumed to be a constant orientation of the cored material.

It is also interesting to note that NRM directions (i.e., before AF demagnetization) typically show better clustering than directions obtained at 20 mT, which sheds some light on the timing of the twisting. Whereas NRM often shows a cluster, some sections show a wide distribution of declinations at 20 mT (Fig. **F29**), possibly reflecting core twisting. Such a pattern suggests that rotation or twisting of the core occurs before the acquisition of the secondary magnetization or the drilling-induced overprint. Nevertheless, rotation with an axis parallel to the NRM directions (i.e., vertical along the core axis) would have little or no effect on its distribution. That means that a rotation or twist of the core parallel to the core axis cannot be totally excluded. A rotation of the liner could, for example, occur when it is pulled out of the core barrel on deck. It is important to note that core twisting was observed in cores obtained with the HPCS, which poses an interesting question as to how and when core twisting occurs. Further experiments and observations will be necessary to elucidate the timing and processes controlling such core deformation documented by paleomagnetism but otherwise typically imperceptible. Needless to say, the implications for physical properties that are directional in nature are important, for it is commonly assumed that cored material does not rotate within the liner.

Magnetic reversal stratigraphy

We used magnetic inclination after AF demagnetization at 20 mT to determine the polarity pattern. The magnetic polarity record was then identified using biostratigraphic datums (nannofossils and foraminifers) (see **"Biostratigraphy"**) and correlated with the geomagnetic polarity timescale (GPTS) of Gradstein et al. (2004). The identified chrons and subchrons are given in Table **T17.**

In Hole C0001E, below a somewhat noisy uppermost 8 m, magnetic inclination is dominantly positive to 86 m CSF (Fig. **F30**). This change from normal to reversed polarity (Section 315-C0001E-10H-6) is interpreted as the Brunhes/Matuyama Chron boundary dated at 0.781 Ma (Gradstein et al., 2004), owing to the identified nannofossil Zone NN19 (see **"Biostratigraphy"**). The Matuyama Chron (C1r) is characterized by a predominantly reversed polarity, although we noted the presence of a number of short events of normal polarity (e.g., 148 and 259 m CSF). A normal polarity interval between ~127 and ~131 m CSF is interpreted as a part of the Jaramillo Subchron (C1r.1n) (Sections 315-C0001E-3H-2 through 3H-4) (Fig. **F31**), although the upper and lower limits are absent. The portion of the Matuyama Chron between the base of the Jaramillo Subchron and the top of the Olduvai Subchron possibly shows as many as five short events of normal polarity. Given the constraints of onboard analysis (long-core measurement, partial demagnetization, and response of the pickup coils), with the present data set we cannot unambiguously determine whether the positive inclinations we observe within the Matuyama Chron between ~148 and ~160 m CSF reflect the geomagnetic field or whether they are instead artifacts. More detailed shore-based measurements will be needed to determine the meaning of such short positive inclination intervals within the Matuyama Chron, and our discrete sampling strategy on board was directed toward that goal.

In Hole C0001F (Fig. **F31**), we could reliably determine the top of the Olduvai Subchron (C2n) at 174.7 m CSF (Table **T17**). The bottom of the Olduvai Subchron occurs at 193.5 m CSF, although the subsequent older Matuyama Chron is only represented in 3.3 m of sediment. Below, we encountered a thick sandy unit (lithologic Subunit IIB) that is completely disturbed (see **"Lithology"**), preventing any continuous reliable paleomagnetic analysis. Silty layers, a few centimeters thick, interbedded within the sands might help in obtaining some occasional magnetic polarity readings. The age of the uppermost part of this sandy unit is roughly estimated as ~2 Ma from our magnetostratigraphic correlation (see below). Below the sandy unit, ChRM inclination is dominantly positive in the uppermost ~20 m of the section, interrupted by a short reversed interval at ~218–220 m CSF. The interpretation of such a normal interval as Gauss (C2An) is a possibility, given its proximity to the Olduvai Subchron, but this interpretation is not entirely supported by biostratigraphy data. Rather, nannofossil Zones NN13–NN15 and foraminifer Zone N18 are indicative of Chrons C3n to C2Ar (Fig. **F23**).

The reliability of the remanence in sediments of the middle and lower part of Hole C0001H needs to be carefully considered. We note that magnetization often does not reach an end vector by 20 mT in the interval from ~324 to 374 m CSF. Within this interval, many samples show traces of great circles upon progressive AF demagnetization (Figs. **F32, F33**). Such behavior is indicative of a higher coercive component that is not resolved by AF demagnetization applied onboard. Although we applied progressive thermal demagnetization on several discrete samples, this high-coercivity component could not be fully isolated (Fig. **F34**). The trend of great circles suggests that such a high-coercivity component often has negative inclination (Figs. **F32, F33**). Therefore, we suspect that the primary magnetization for the interval between 324 and 374 m CSF might indeed be negative.

There are two more issues affecting the overall data quality of Hole C0001H. The first, discussed earlier, is biscuiting. When the core is not uniformly magnetized (e.g., because of differential rotation of segments or biscuiting), data should be treated with caution. Results from Shipboard Scientific Party (2002) documented that across a rotated break between segments of uniform magnetization, x- and y-components, in particular, are underestimated. More detailed demagnetization on shore will allow us to determine a more reliable magnetic reversal stratigraphy. The second issue relates directly to the paleomagnetic behavior of sediments. Very often demagnetization diagrams show large scatter of end vectors at 20 mT in numerous cores. Erratic remanence behavior could be due to the acquisition of spurious magnetization in the magnetometer or perhaps to the presence of ferrimagnetic iron sulfides (greigite or pyrrhotite). The presence of pyrite has been documented in numerous parts of the hole, supporting the possible presence of ferrimagnetic iron sulfides as carriers of stable remanence.

As far as polarity, calcareous nannofossils are indicative of Zones NN15–NN13 (see **"Biostratigraphy"**), which correlate to Chron C3n or Gilbert Chron (Gradstein et al., 2004) for the interval of positive inclinations between 218 and 220 m CSF. Under this assumption, the polarity change at ~320 m CSF could be tentatively correlated to the bottom of Chron C3n.4n (Fig. **F35**). Nevertheless, the magnetostratigraphic record below ~220 m CSF is rather noisy, preventing any satisfactory correlation to the GPTS at this time. The correlation suggested here implies that the sandy unit was deposited sometime between ~2 and ~5 Ma (Fig. **F36**) and that the gross sediment accumulation rate in the upper ~200 m is ~10 cm/k.y.

Inorganic geochemistry

Interstitial water geochemistry

A total of 48 whole-round sections were collected for interstitial water analyses (14 samples from Hole C0001E, 16 samples from Hole C0001F, and 18 samples from Hole C0001H) (Table **T18**). One whole-round section was cut from each core when possible, with the exception of the first core sampled near the seawater/sediment interface. Here three samples (Core 315-C0001E-1H) were retrieved for interstitial water extraction. To obtain enough interstitial water for shipboard and shore-based analyses, 20 to 30 cm long sections were squeezed from samples retrieved from Holes C0001E and C0001F. Because sediment from Hole C0001H is more consolidated, ~45 cm long sections were used for pore water extraction.

Sulfate reduction and diagenesis of organic matter (alkalinity, phosphate, and ammonium)

The sulfate-methane transition (SMT) is a fundamental diagenetic boundary within many marine sediments. Microbial sulfate reducers utilize sulfate dissolved in interstitial water to oxidize sedimentary organic matter above the SMT. Below the SMT, methanogens actively generate methane as a byproduct of respiration. Microbially mediated anaerobic oxidation of methane at the SMT balances the downward flux of sulfate with the upward diffusive flux of methane following the generalized equation (Reeburgh, 1976; Borowski et al., 1996)

$$CH_4 + SO_4^{2-} \rightarrow HCO_3^- + HS^- + H_2O.$$

Sulfate concentrations decrease monotonically from the seawater value of ~28 mM to nearly 0 mM at ~14 m CSF at Site C0001. The flux of sulfate to the SMT, which is equal to the methane flux from below, is assessed using an estimate for the sulfate concentration-depth gradient and Fick's first law of diffusion:

$$J = D_0\phi^3(\delta C/\delta X),$$

where

D_0 = diffusion coefficient for sulfate (5.8×10^{-6} cm^2/s at 5°C),
ϕ = sediment porosity (0.65), and
$\delta C/\delta X$ = sulfate concentration gradient with depth (2.3 mM/m), based on the interval between Samples 315-C0001E-1H-4 and 2H-4.

The calculated sulfate flux is 1.2×10^{-3} mmol/cm^2/y (Fig. **F37**). Below the SMT, sulfate concentrations generally remain below 0.3 mM with a decreasing trend to the bottom of the hole. Sulfate concentrations that appear above 0.3 mM are likely contaminated with seawater during sampling and extraction procedures. The lack of significant sulfate with depth precludes the possibility of deep-sourced fluids containing sulfate at Site C0001.

Alkalinity and dissolved phosphate concentrations consistently increase to maximum values at 28–37 m CSF (Fig. **F37**). These increases in concentration result from microbial sulfate reduction of sedimentary organic matter (e.g., Berner, 1980). At greater depths, interstitial water alkalinity decreases, consistent with the removal of alkalinity by carbonate precipitation. This precipitation also affects Ca concentrations. Similarly, phosphate concentrations decrease with depth below the maximum, resulting from the removal from solution by carbonate or oxide phases.

Dissolved ammonium concentrations reach a maximum (~3 mM) between 105 and 175 m CSF, well below the alkalinity and phosphate maxima (Fig. **F37**). This increase in ammonium is a byproduct of microbial respiration. The decrease in ammonium with depth reflects the uptake of ammonium onto clay minerals by ion exchange, although alkalinity and phosphate concentrations progressively decrease downhole. Particularly in the upper accretionary unit below 200 m CSF, ammonium concentrations remain uniform below the transition between 200 and 225 m CSF.

Halogen concentrations (Cl and Br)

Chloride concentrations increase from a seafloor value of ~554 mM to 557 mM at 9 m CSF. They then decrease to ~545 mM at 100 m CSF at a local minima and then increase nearly monotonically below this interval (Fig. F37). Chloride is one of the most conservative tracers in interstitial water in marginal settings with the exception of hydrate-related processes. The ~4% dilution of the interstitial water at 100 m CSF and the several other anomalously low values at 263, 400, and 440 m CSF likely reflect an input of freshwater from the dissociation of gas hydrate. Although the dissociation of gas hydrate is the most likely freshwater source in this area, no evidence of gas hydrates, such as low-temperature anomalies, bubbling on the core surface, high-resistivity anomalies in LWD records, or recovery of visible gas hydrates, was observed at Site C0001.

Br concentrations in pore water are often affected by diagenetic processes. The decomposition of organic matter at depth liberates bromine to interstitial waters. As noted above in the case of chloride, bromine concentrations are also affected by dilution, presumably from the dissociation of gas hydrate. However, the small changes (~4%) observed above are at the level of the analytical noise in the data, indicating that diagenetic processes dominate in Br interstitial water profiles in this setting. Br concentrations generally increase with depth to 168 m CSF, below which concentrations remain ~1100 mM. This change coincides with the transition in ammonium concentrations from a parabolic shape to a constant value, suggesting that there is a change in the nature of microbial processes at this depth, possibly because of maturation of the available organic materials.

Major cations

Na concentrations increase from ~450 mM to a tight range from 470 to 490 mM. Within this 4% range, concentrations are scattered because of analytical uncertainties; nevertheless, there is a general trend of increasing concentrations with depth (Fig. F38). This increase is partially accounted for by the Cl increase and partially attributed to exchange reactions with clays. A fraction of these exchange reactions could be associated with ammonium. Other exchange reactions with K and Ca are likely. For example, the steady decrease in K concentrations with depth results from exchange reactions with clay mineral phases (Fig. F38).

Ca concentrations decrease in the upper 28 m of the sediment column where sulfate reduction occurs. Here, the extensive production of alkalinity during sulfate reduction results in the precipitation of carbonates and the removal of Ca from interstitial water. Below this depth, Ca concentrations increase; however, the increase is not as great as the decrease observed in the Mg data (Fig. F38). Seawater interactions with volcanics in the absence of high alkalinity generally show a 1:1 exchange between Mg and Ca. Below ~150 m CSF, Mg and Ca data form a linear trend with a slope of –0.74, indicating that even at depth carbonate precipitation occurs, controlling Ca concentrations and alkalinity.

Minor elements

Dissolved silica concentrations increase rapidly in the upper 4 m CSF in response to the dissolution of diatoms (Fig. F38). The steady increase in concentration with depth probably reflects thermal equilibrium with biogenic silicate phases, given the higher solubility at higher temperatures with depth. In contrast, B concentrations decrease systematically with depth, being removed from interstitial water. Li concentrations increase systematically with depth below the Li minima observed at 28 m CSF (Fig. F38). Similar to the case for B, Li concentration-depth profiles are likely governed by reactions with clay minerals.

Mn concentrations increase linearly to 5 µM at 250 m CSF. Below this depth, Mn concentrations increase rapidly to a local maximum of 12.3 µM at 301 m CSF and then decrease to 6.5 µM at 354 m CSF (Fig. F38). Mn concentrations then increase to 12 µM in the lowermost sections at ~440 m CSF. The high Mn concentration in the shallowest sample is likely the result of the dissolution of oxyhydroxide phases, resulting from microbial reactions. The increase in Mn concentrations downcore and the profile shape in general are probably a function of microbial processes and the deposit of Mn-rich carbonates or as-yet undetermined trace mineral phases. Similarly, the Fe concentration-depth profile shows an initial increase from seawater values, presumably resulting from microbial processes. Fe concentrations decrease to 28 m CSF and then increase linearly to ~100 m CSF (Fig. F38). Below 100 m CSF, the overall trend is increasing Fe concentrations with depth, yet there is substantial scatter in the data. This scatter could be related to isolated pockets where iron is liberated from organic material and subsequently reduced and removed into sulfide-rich phases or may be attributed to contamination and oxidation/removal during sample processing.

Sr and Ba concentrations increase with depth to ~230 m CSF, at which point there is an abrupt change in both concentration-depth trends (Fig. F39). Sr concentrations in the uppermost 8 m CSF are likely controlled by carbonate precipitation in an interval in which the alkalinity rises to its maximum. Increasing Sr and decreasing alkalinity with depth correlate to the apparent scatter in both data sets. These data are consistent with the precipitation of Sr-bearing carbonates, but artifacts caused during sample processing cannot be precluded. Ba concentrations in the upper 9 m are low because barium sulfate is insoluble and any available sulfate rapidly removes Ba from interstitial water. In contrast, beneath the sulfate reduction zone where sulfate concentrations are generally <0.3 mM, Ba concentrations increase, reaching a maximum value of 403 µM at 223 m CSF. This increase with depth is nearly monotonic with the exception of a decrease in a sand layer at 203 m CSF. Beneath the 230 m CSF interval, Ba appears to behave erratically except for the fact that it remains closely correlated with Sr in every interval. Within this interval, sulfate and Ba concentrations are within the same range (~50–300 µM) and there is an inverse correlation between sulfate (from contamination) and Ba concentrations. This correlation suggests that the scatter in the Ba data reflect contamination issues resulting from drilling and sampling procedures.

Trace elements

Concentrations of the transition metals Mo, V, Zn, and Cu were measured by inductively coupled plasma–mass spectrometry (ICP-MS) aboard the ship. Ten of these samples were then analyzed on shore (Table **T18**). This combined data set of transition metal profiles is affected by redox conditions within the sediment column. For example, Mo concentrations decrease in the upper 9 m, likely caused by microbial processes. Below this interval, the Mo concentration-depth profile is similar to that of Mn and to a lesser degree Fe (Fig. **F39**). In contrast, Zn concentrations increase with depth similar to those of Mo. The general V concentration-depth trend is one of decreasing concentration with depth to 11 nM at the base of the core. Similarly, the Cu concentration-depth profile is not consistently correlated to any other dissolved species that was measured. Instead, the Cu profile shows a remarkable degree of mobilization to 6160 µM at 253 m CSF, probably influenced by microbial processes.

Rb, CS, Pb, and U concentrations were measured with ICP-MS on board the ship, and 10 samples that included Y were measured ashore. Rb concentrations decrease rapidly in the uppermost 28 m of the sediment section, similar to the K concentration-depth profile (Fig. **F39**). This initial removal of K results from clay-interstitial water interactions. At greater depths the decrease may reflect thermal equilibrium with clay minerals. Cs concentrations are almost twice the value of bottom seawater. Between 200 and 220 m CSF, Cs concentrations drop from 3.5 to 1.7 nM. A similar but smaller offset is observed in Rb data at this depth. Such gradients, if real, cannot be supported over long periods of time because diffusion tends to smooth such anomalies. Pb concentrations are generally <2 nM but have local maxima with the highest measured concentration of 10.1 nM Pb at 175 m CSF (Fig. **F39**). Uranium concentrations are depleted overall, relative to bottom seawater values of ~14 nM, with a significant degree of scatter in measured values (Fig. **F39**). There are numerous distinct increases in U concentrations; the two largest, which increase with the exception of the first sampled depth, are at 150 (6.0 nM) and 217 m CSF (5.5 nM). The mechanism that produces these higher values cannot be determined at this time. Y concentrations in pore water are generally greater than that of seawater (0.3 pM), but no trends are evident in the small data set (Fig. **F40**).

$\delta^{18}O$ and δD of interstitial water

Both $\delta^{18}O$ and δD values decrease from seawater values (~0‰) to –2.5‰ and –8‰, respectively, at the bottom of Unit I (Fig. **F40**). These decreasing trends likely result from the interaction of interstitial water with clay minerals. Such decreases, particularly the large decrease in δD values, were attributed to membrane filtration of clay minerals. In contrast, $\delta^{18}O$ values continue to decrease in Unit II; however, δD values remain constant at around –10‰. Throughout this unit there is an increase in the chlorinity, possibly resulting from hydration reactions that may then cause the resulting decrease in the $\delta^{18}O$ values. There is not enough carbonate to have an affect on $\delta^{18}O$, considering the huge amount of oxygen in interstitial water.

Organic geochemistry

Hydrocarbon gas composition

Methane is the predominant hydrocarbon present in all Site C0001 cores. Concentrations of methane and ethane, along with methane to ethane (C_1/C_2) ratios, are shown in Table **T19.** Minor amounts of ethane (<10 ppmv) were detected in most sections, and no heavier hydrocarbons were detected. The vertical distributions of headspace methane and ethane are shown in Figure **F41.** Methane concentrations increase rapidly from 3.6 ppmv in the near-surface sample (1.6 m CSF) to 36,330 ppmv at 34 m CSF (Fig. **F42**). Concentrations decrease to 100 m CSF and remain nearly constant to 231 m CSF. Below this depth, methane concentrations are relatively high; the highest value (43,884 ppmv) occurs at 278 m CSF. Vertical distribution of ethane is similar to that of methane (Fig. **F41**). The C_1/C_2 ratio ranges from 1065 to 6818 with the exception of a low abnormality (342) at 192 m CSF (Fig. **F43**). The C_1/C_2 ratio gradually decreases with depth in Unit I and slightly increases with depth in Unit II. The increase of methane concentrations and the C_1/C_2 ratio in Unit II indicates a greater contribution of biogenic methane at depth. The C_1/C_2 ratio is mostly >1000, suggesting that methane found at Site C0001 is biogenic, not thermogenic, in origin. The calculated SMT depth is 27 m CSF (Fig. **F41**). This inverse correlation suggests that methane results from methanogenesis, which is inhibited in the presence of sulfate.

Sediment carbon, nitrogen, and sulfur composition

A total of 143 mud and mudstone samples were collected at Site C0001 next to whole-round samples for pore water and geotechnical tests. All samples were analyzed for inorganic carbon, total carbon, nitrogen, and sulfur (see **"Organic geochemistry"** in the "Expedition 315 methods" chapter for analytical procedures). Values of inorganic carbon, calcium carbonate ($CaCO_3$), total organic carbon (TOC), total nitrogen, organic carbon to total nitrogen (C/N) ratio, and total sulfur are listed in Table **T20** and presented in Figure **F44.**

Calcium carbonate content calculated from inorganic carbon content varies from 0.2 to 31.9 wt%. In Unit I, concentrations are highly variable and range from 0.5 to 31.9 wt% with an average of 12.5 wt%. Concentrations tend to decrease with depth, although absolute values are considerably scattered. In Unit II, concentrations are more consistent and the average value is 3.2 wt%. Low carbonate contents throughout Unit II indicate deposition below the CCD.

TOC content ranges from 0.01 to 0.67 wt% with an average of 0.37 wt%. Total nitrogen contents are <0.15 wt%, and the average value is 0.09 wt%. The C/N ratio shows little variation with depth except for high values at 168 and 184 m CSF; the average value is 4.4. This value is more enriched in nitrogen than the expected value for marine organic matter (6–9) if the fraction of inorganic ammonium in the total nitrogen can be ignored. Clay-bound nitrogen substances, including inorganic ammonium, cause C/N ratios to decrease. This effect may explain the low C/N ratio.

Total sulfur content ranges from 0.12 to 4.85 wt% with an average of 0.52 wt%. In Unit I, concentrations are fairly uniform. Four spike peaks are observed at 85, 103, 181, and 353 m CSF, and their concentrations are >2.0 wt%. Between 200 and 260 m CSF in Subunit IIA, concentrations are relatively higher. Below this depth, concentrations decrease and then remain constant.

Microbiology

Sample information

A total of 38 whole-round cores were taken from Holes C0001E, C0001F, and C0001H for microbiological analysis. Table **T21** shows the depths of the three types of whole-round cores. Some whole-round cores were subsampled on board for cell fixing, deoxyribonucleic acid (DNA) and ribonucleic acid (RNA) extraction, and culturing studies. Onboard work mainly included preserving whole-round cores and subsamples for shore-based work, fixing cells for cell detection and counting, and setting up enrichment cultures of sulfate-reducing bacteria.

Cell detection with epifluorescence microscopy

A total of 12 fixed cell samples were selected from the entire depth with roughly equal intervals and were stained with double-stranded DNA-binding SYBR Green I stain. Cells were detected in core samples from 0.5 to 448 m CSF (Table **T22**). Cells were rod, oval, and coccoidal in shape (Fig. **F45**). Cells were also detected in both seawater gel and kill mud, which shows that these drilling muds are a potential source of microbial contamination if mixed with sediment core material. In a control sample of 15 mL filtered phosphate-buffered saline and in a sediment sample without SYBR Green I staining, only a very few green particles were detected.

Cultivation experiments

More than 200 enrichment cultures were established during Expedition 315 with the aim to culture sulfate-reducing microorganisms. Cultures were monitored for sulfate reduction based on the formation of black iron sulfide precipitate, which indicates production of biogenic hydrogen sulfide in the iron-containing medium. During the expedition, blackening of the growth medium was observed in only a few sediment cultures incubated at 9° or 37°C and in seawater gel cultures incubated at 37°C. At 9°C, sulfate reduction was first observed after 3 weeks of incubation; at 37°C, some cultures turned dark within 1 week. Rod- and oval-shaped cells were detected in the cultures by phase-contrast microscopy. Some of the cells formed long chains.

Physical properties

Porosity and density

At Site C0001, 638 discrete samples were analyzed for moisture and density (MAD) (Blum, 1997). These were taken in Holes C0001B (15 samples), C0001E (194 samples), C0001F (221 samples), and C0001H (208 samples).

Figure **F46A** shows porosity versus depth in a composite section of all drill holes at Site C0001. Porosity from discrete samples decreases systematically with depth in lithologic Subunit IA from an average of 63.6% in the uppermost 10 m to an average of 54.7% from 190 to 195 m CSF. Average porosity between ~195 and 205 m CSF (Subunit IB) is 47.7%. The porosity trend is offset in Unit II to higher values and decreases with depth from an average of ~59% at ~213 m CSF to ~50% at the bottom of Hole C0001F (~450 m CSF) (Fig. **F46A**). Similar porosity trends are evident in data from whole-core multisensor core logger (MSCL) measurements; however, porosity values are highly scattered and larger than those derived from discrete samples (Fig. **F46A**). If we exclude the outliers at the upper limit of the data set, a corridor of dense data points plots immediately above the data on discrete samples. MSCL-porosity is 60%–70% near the top of the hole and linearly decreases downhole to values between 52% and 62% at the contact with Subunit IC sandy deposits. Porosity values derived from MAD measurements of sand lithologies probably do not reflect true formation index properties because of drilling disturbance of the unconsolidated material. Unit II silty clays and mudstones are offset again to higher values (56%–68% porosity) and then steadily decrease to ~53%–65% near the bottom of Hole C0001F (Fig. **F46A**). Porosities derived from MSCL data are systematically higher than those from discrete MAD measurements for a variety of reasons, including drilling disturbance and mixing of drilling fluid with the sediment, incomplete filling of the core liner leading to anomalously high void ratios, and gas expansion that generates voids and cracks not present in the undisturbed formation.

Figure **F46B** shows bulk density on discrete samples and derived from MSCL measurements on whole-round cores (MSCL-W; see the **"Expedition 315 Methods"** chapter for details). Bulk densities of discrete samples scatter between ~1.6 and 1.7 g/cm^3 just below the seafloor and increase nearly linearly to 1.70–1.75 g/cm^3 at 175 m CSF (Fig. **F46B**), roughly coinciding with the base of lithologic Subunit IA. Subunit IB shows slightly higher wet bulk densities (1.75–1.90 g/cm^3). At the top of the Unit II accreted sediments, a shift to lower densities is observed (~1.70–1.80 g/cm^3) (Fig. **F46B**). Bulk densities in the accretionary prism facies show a downhole increase to values ranging between 1.80 and 1.90 g/cm^3 at 450 m CSF.

Similar to the porosity data set, bulk densities from the MSCL-W parallel the overall downhole trend for discrete samples but are consistently offset to lower values (Fig. **F46B**).

Figure **F46C** shows the grain density trend at Site C0001 versus depth. Average grain density in the upper 195 m (Subunit IA) is 2.71 g/cm^3 and increases slightly with depth. Grain density in Unit II shows the same subtle continuous increase with depth. This increase may be attributed to higher clay mineral contents in the accreted strata relative to the overlying hemipelagic mud (i.e., clay with grain densities = ~2.75 g/cm^3, quartz = 2.65 g/cm^3), the latter of which is more abundant in calcite (see bulk powder XRD analytical results in **"X-ray diffraction mineralogy"**).

Explanations for the offset in porosity and density between Units I and II (Fig. **F46A, F46B**) can be divided into two categories: methodological or geological.

Two methodological artifacts cause overestimation of porosity. First, upon oven drying at 105°C, pore water and water contained in some hydrous minerals are removed. In particular, water contained in smectite interlayers is completely removed after oven drying at 105°C for 24 h, at least for mineral compositions generally found in marine sediments (Colten-Bradley, 1987; Brown and Ransom, 1996; Henry, 1997). Because the magnitude of this effect depends on the abundance of hydrous clay, we anticipate a larger porosity overestimate in Unit II than in the overlying slope apron. Second, ESCS and RCB coring may disturb the sediment somewhat and cause a secondary, artificial change in porosity and wet bulk density although samples were carefully chosen from a relatively undisturbed portion.

One possible geological reason for the observed offset in the physical property data is that the consolidation behavior (and therefore compaction state) is highly dependent on sediment grain size distribution and sediment composition. In addition, the accreted material may suffer deformation and a certain degree of lateral shortening in addition to compaction. If this deformation, which is attested by faulting and formation of shear zones (see **"Structural geology"**), cannot be accommodated by pore space reduction and pore fluid drainage, overpressures may result. Such supra-hydrostatic fluid pressures hinder compaction and are not unknown to accretionary complexes (e.g., see Screaton et al., 1990; Saffer and Bekins 2002). However, given the shallow depth as well as the highly permeable sands overlying the accreted Unit II, it is highly unlikely that these latter materials could support enhanced fluid pressures over significant time spans to counteract compaction.

Shear strength

Results from vane and penetrometer shear strength measurements are presented in Figure **F47A.** Results obtained in the uppermost 30 m from Hole C0001B (Expedition 314) are included in the plot.

Shear strength generally increases with depth from ~10 kPa at the seafloor to ~150 kPa at 195 m CSF with a clear negative correlation between porosity and strength. Below 195 m CSF, excessive cracking and separation of the core material occurred and the vane shear measurement technique was abandoned. Penetrometer measurements were conducted to a maximum depth of 247 m CSF. Circled measurements on Figure **F47A** were derived from cores obtained by the ESCS. A high degree of sample disturbance was noted in these cores, and the measured strengths may not reflect actual sediment shear strength values. Penetrometer-based strength exceeds vane-based strength by an average of 37% over a comparable measurement range.

Thermal conductivity

Thermal conductivity measurements were conducted on whole-round HPCS cores (<230 m CSF) with the needle probe and on split samples from RCB cores (>230 m CSF) with the half-space probe.

Thermal conductivities of HPCS cores (<230 m CSF) range from 0.81 to 1.45 W/(m·K). At 200–230 m CSF, core recovery was poor and the sediment disturbed, which resulted in a relatively large variation in thermal conductivity in this depth interval (Fig. **F47C**). In comparison, thermal conductivities of RCB cores (>230 m CSF) are more tightly constrained, ranging from 1.09 to 1.31 W/(m·K). Uncertainties in the measurements notwithstanding, thermal conductivities generally increase with depth (Fig. **F47C**).

Color spectroscopy

Color reflectance measurement results are presented in Figure **F48.** In Subunits IA and IB, values of L* ranged from 30 to 50. Some high values of ~70 correspond to ash layers. Values of a* ranged from –2 to 1, and those of b* ranged from 2 to 6. At the top of this unit, slight decreases in a* and b* values were observed. In Subunit IC, the value of L* is relatively lower than values found in Subunits IA and IB, ranging from 25 to 45. Compared to values in Subunits IA and IB, values of a* are higher, ranging from 0 to 3, and those of b* are lower, ranging from 0 to 4. In Unit II, the value of L* ranged from 30 to 50. Values of a* ranged from –2 to 1, and those of b* ranged from 0 to 4. There is no significant anomaly of these values with depth.

Downhole temperature

Downhole temperature was measured with the APCT3. Starting at a depth of 12 m CSF, measurements were obtained from every third core. In total, seven data points are available to 165.5 m CSF (Table **T23**). Below this depth, the APCT3 tool was not used when getting close to HPCS refusal in Hole C0001H because this special cutting shoe is not compatible with RCB coring. Data points show a nearly linear increase in temperature with depth, except for one outlier at 123 m CSF. The data delineate a temperature gradient of 0.044°C/m (Fig. **F49**) when discounting the 6.98°C temperature obtained at 127 m CSF, whereas the gradient would be 0.0043°C/m with this point.

The calculation of heat flow was obtained by using the Excel add-in Program Solver. First total resistance estimated by integration of 1/(thermal conductivity) was used to calculate temperature with the following formula:

$$T_c = R \times Q + T_{bw},$$

where

T_c = calculated temperature,
R = total resistance,
Q = heat flow, and
T_{bw} = bottom water temperature.

Thermal conductivity was measured on core samples and heat flow and bottom water temperature are unknown parameters. Heat flow and bottom water temperature were 47 mW/m^2 and 2.12°C from mean square error minimization. Temperatures were then extrapolated downhole assuming constant heat flow (Fig. **F49**). Resultant values of heat flow and bottom water temperature were 47 mW/m^2 and 2.12°C, respectively.

Discrete sample *P*-wave velocity and electrical conductivity

P-wave velocity and electrical conductivity were measured on discrete samples between 230.19 and 456.83 m CSF. Measurements were performed in three orthogonal directions on cubes. Data tables in Microsoft Excel format are given as supplementary material (see C0001_DS_VP_EC.XLS in 315_PHYS_PROPS in **"Supplementary material"**). Cubes were generally taken such that cube axes *x*, *y*, and z correspond to the core referential. There were, however, exceptions noted on the log sheets when dipping beds were recognized (see the **"Expedition 315 methods"** chapter). Variations of electrical conductivity and P-wave velocity with depth are consistent with the evolution of porosity. Porosity and conductivity decrease with depth from 230 to 350 m CSF, whereas P-wave velocity increases, as may be expected from a consolidation trend. From 350 to 400 m CSF, porosity, electrical conductivity, and P-wave velocity remain constant on average. Porosity and electrical conductivity decrease and P-wave velocity increases again from 400 to 456.85 m CSF (Fig. **F50**). These changes are not correlated with major lithologic changes. Electrical conductivity and P-wave velocity are generally smaller in the z-direction than they are in the x- and y-directions (Fig. **F51**). However, the anisotropy of the samples in the x, y plane is comparable to the transverse anisotropy (see the **"Expedition 315 methods"** chapter). This indicates overprinting of the transverse anisotropy resulting from normal basinal compaction by tectonic strain in the accretionary wedge. Shore-based sample reorientation is needed for further interpretation.

Core-log-seismic integration

Cores taken from Holes C0001B, C0001E, and C0001F were cross-correlated based on MSCL-W magnetic susceptibility data. Cores from Hole C0001B provide a more continuous record of the uppermost 40 m of sediment than those from Hole C0001E; Core 315-C0001E-3H was almost completely missing because of a jammed core liner. The fitted profiles and depth shifts applied to Hole C0001E cores are given in Figure **F52.** Uncertainty of the depth correlation is <10 cm. The lowermost core in Hole C0001E (315-C0001E-13H) overlaps the uppermost core in Hole C0001F (315-C0001F-1H). A distinctive pair of magnetic susceptibility peaks, corresponding to ash layers, was found at 110.0 and 110.4 m CSF in Core 315-C0001E-13H and at 112.9 and 113.1 m CSF in Core 315-C0001F-1H. This leads us to estimate an offset of 2.7 m between strata in Holes C0001E and C0001F.

Gamma ray logs show quasi-periodic oscillations of 10 m wavelengths in the interval from 50 to 120 m CSF (Fig. **F53**). Considering the sedimentation rates (see **"Biostratigraphy"** and **"Paleomagnetism"**), these may correspond to 100,000 y eccentricity cycles (see Fig. **F22** in the "Expedition 315 methods" chapter). Independent of their interpretation, these regular oscillations provide a reliable basis for core-log correlation over this interval, which comprises cores from Holes C0001E and C0001F. In the interval from 120 to 200 m CSF, the gamma ray log alone does not provide unique correlation solutions, but additional constraints arise from the sand layers of lithologic Subunit IC. These are found, with intercalated mud intervals, between 196.76 and 206.93 m CSF-B (IODP Method B; see the **"Expedition 315 methods"** chapter) in cores and are well imaged as conductive layers in the resistivity-at-the-bit image between 192 and 199 m LSF. This match constrains the position of the unconformity between the accretionary prism and overlying slope sediment. It also constrains the stratigraphic offset between Holes C0001F and C0001D to 4.75 m at the top of the sand and 8 m at the base. Correlations in the 120–200 m interval were refined from gamma ray nearest peak correlations. A good fit of the MSCL and LWD gamma ray data is obtained in the lower part of Hole C0001D (from 212 to 230 m CSF) with offsets of 7 to 9 m. This suggests a lateral variation of sand thickness from 7 m in Hole C0001D to ~10 m in Hole C0001F.

Taking into account this 9 m shift of the base of Hole C0001F, it is logical to fit the magnetic susceptibility peaks within Unit II at 231.08 and 233.04 m CSF in Core 315-C0001H-1R with those located ~8 m deeper at 239.49 and 240.37 m CSF-B in Core 315-C0001F-21X (Fig. **F52**) and to infer an upward shift of ~1 m of the uppermost part of Hole C0001H with respect to the LWD hole. Further downhole, correlation between Holes C0001H and C0001D relies primarily on a limited number of cores with good recovery and distinctive gamma ray profiles: Cores 315-C0001H-4R (262 m CSF), 7R (295 m CSF), 11R (327 m CSF), 12R (332 m CSF), 14R (355 m CSF), and 16R (372–373 m CSF). There are no reliable constraints in natural gamma ray values from 373 m CSF to the bottom of the cored hole at 456.8 m CSF. The fit of the gamma ray data from Holes C0001E, C0001F, and C0001G is summarized in Table **T24.**

In Hole C0001H, sonic and resistivity logs can be compared with measurements on samples. Sample resistivity is computed from the mean of two complex conductivity measurements made in the horizontal plane at a 90° angle. A correction for in situ temperature (T, in degrees Celsius) is then applied, assuming the resistivity (R) of the samples varies in the same way as that of seawater (Bourlange et al., 2003):

$$R(T) = R(25°\text{C})/[1 + 0.02(T - 25)].$$

Temperature at a given depth is computed based on heat flow determination (47 mW/m^2) and thermal conductivity measurements on cores made during this expedition (see **"Thermal conductivity"**). LWD ring resistivity is compared with temperature-corrected sample resistivity in Figure **F54.** Data from measured samples follow the LWD trend, but values tend to be higher on average, notably near the top and bottom of the cored interval (220–300 and 439–460 m CSF). One possible explanation for the deviation in the upper interval could be clay surface conductivity, which depends less on temperature than seawater conductivity (Revil et al., 1998). The temperature extrapolated at the bottom of Hole C0001H is ~20°C, close to laboratory temperature (21.5° ± 0.2°C), so the deviation observed in the lowermost cores (Cores 315-C0001H-25R and 26R) probably requires another explanation.

P-wave velocity measured on samples is lower than in situ values of *P*-wave velocity from LWD logs but follows the same trends: increasing from 230 to 320 m CSF, nearly constant from 320 to 400 m CSF, and then increasing again to from 400 m CSF to the base of the borehole (456.8 m CSF) (Fig. **F55**). *P*-wave velocity is dependent on temperature, fluid pressure, and confining pressure. A 2.4% correction is applied to account for the variation of the *P*-wave velocity of seawater between the sea surface and 2200 m depth (Fofonoff, 1985), and an additional empirical correction of 1% per 100 m below the seafloor is applied to account for the effect of confining pressure. The corrected velocities closely follow the 10–50 m wavelength variations in the LWD data, except in the lower part of the borehole, where values measured on samples increase more rapidly than those of the LWD data. The same was observed for resistivity. Several explanations are feasible:

- Sampling bias, if only the more lithified (higher velocity and resistivity) layers were recovered in the last few cores,
- Increase of borehole diameter, or
- Fluid pressure greater than hydrostatic in the formation or in the borehole, causing dilatancy.

Caliper data from the Azimuthal Density Neutron tool and measurement-while-drilling annular pressure data do not indicate an increase of borehole diameter or of borehole fluid pressure above 450 m LSF. In fact, conditions in the LWD hole deteriorate only below 500 m LSF. Sampling bias and/or elevated formation fluid pressure remain possible explanations.

References

Berner, R.A., 1980. *Early Diagenesis: A Theoretical Approach:* Princeton, NJ (Princeton Univ. Press).

Blum, P., 1997. Physical properties handbook: a guide to the shipboard measurement of physical properties of deep-sea cores. *ODP Tech. Note,* 26. **doi:10.2973/odp.tn.26.1997**

Borowski, W.S., Paull, C.K., and Ussler, W., III, 1996. Marine pore-water sulfate profiles indicate in situ methane flux from underlying gas hydrate. *Geology,* 24(7):655–658. **doi:10.1130/0091-7613(1996)024<0655:MPWSPI>2.3.CO;2**

Bourlange, S., Henry, P., Moore, J.C., Mikada, H., and Klaus, A., 2003. Fracture porosity in the décollement zone of Nankai accretionary wedge using logging-while-drilling resistivity data. *Earth Planet. Sci. Lett.,* 209(1–2):103–112. **doi:10.1016/S0012-821X(03)00082-7**

Brown, K.M., and Ransom, B., 1996. Porosity corrections for smectite-rich sediments: impact on studies of compaction, fluid generation, and tectonic history. *Geology,* 24(9):843–846. **doi:10.1130/0091-7613(1996)024<0843:PCFSRS>2.3.CO;2**

Brunner, C.A., Andres, M., Holbourn, A.E., Siedleck, S., Brooks, G.R., Molina Garza, R.S., Fuller, M.D., Ladner, B.C., Hine, A.C., and Li, Q., 2002. Quaternary planktonic foraminiferal biostratigraphy, ODP Leg 182 sites. *In* Hine, A.C., Feary, D.A., Malone, M.J. (Eds.), *Proc. ODP, Sci. Results,* 182: College Station, TX (Ocean Drilling Program), 1–16. **doi:10.2973/odp.proc.sr.182.011.2002**

Colten-Bradley, V.A., 1987. Role of pressure in smectite dehydration—effects on geopressure and smectite-to-illite transformation. *AAPG Bull.,* 71:1414–1427.

Cowan, D.S., 1982. Origin of "vein structure" in slope sediments on the inner slope of the Middle America Trench off Guatemala. *In* Aubouin, J., von Huene, R., et al., *Init. Repts. DSDP,* 67: Washington, DC (U.S. Govt. Printing Office), 645–650. **doi:10.2973/dsdp.proc.67.132.1982**

Fofonoff, N.P., 1985. Physical properties of seawater: a new salinity scale and equation of state for seawater. *J. Geophys. Res.,* 90(C2):3332–3342. **doi:10.1029/JC090iC02p03332**

Garcés, M., Parés, J.M., and Cabrera, L., 1996. Further evidence for inclination shallowing in red beds. *Geophys. Res. Lett.,* 23(16):2065–2068. **doi:10.1029/96GL02060**

Gradstein, F.M., Ogg, J.G., and Smith, A. (Eds.), 2004. *A Geologic Time Scale 2004:* Cambridge (Cambridge Univ. Press). **http://www.stratigraphy.org/**

Henry, P., 1997. Relationship between porosity, electrical conductivity, and cation exchange capacity in Barbados wedge sediments. *In* Shipley, T.H., Ogawa, Y., Blum, P., and Bahr, J.M. (Eds.), *Proc. ODP, Sci. Results,* 156: College Station, TX (Ocean Drilling Program), 137–149. **doi:10.2973/odp.proc.sr.156.020.1997**

King, R.F., 1955. The remanent magnetism of artificially deposited sediments. *Geophys. J. Int.,* 7(S3):115–134. **doi:10.1111/j.1365-246X.1955.tb06558.x**

Korig, D.E., and Lundberg, N., 1990. Deformation bands from the toe of the Nankai accretionary prism. *J.Geophys. Res.,* 95(B6):9099–9109. **doi:10.1029/JB095iB06p09099**

McFadden, P.L., and Reid, A.B., 1982. Analysis of paleomagnetic inclination data. *Geophys. J. R. Astron. Soc.,* 69:307–319.

Moore, G.F., Taira, A., Klaus, A., et al., 2001. *Proc. ODP, Init. Repts.,* 190: College Station, TX (Ocean Drilling Program). **doi:10.2973/odp.proc.ir.190.2001**

Ogawa, Y., 1980, Beard-like veinlet structure as fracture cleavage in the Neogene siltstone in the Miura and Boso peninsulas, central Japan. *Kyushu Daigaku Rigakubu Kenkyu Hokoku, Chishitsugaku,* 13(2):321–327.

Pickering, K.T., Underwood, M.B., and Taira, A., 1993a. Open-ocean to trench turbidity-current flow in the Nankai Trough: flow collapse and flow reflection. *In* Hill, I.A., Taira, A., Firth, J.V., et al., *Proc. ODP, Sci. Results,* 131: College Station, TX (Ocean Drilling Program), 35–43. **doi:10.2973/odp.proc.sr.131.104.1993**

Pickering, K.T., Underwood, M.B., and Taira, A., 1993b. Stratigraphic synthesis of the DSDP-ODP sites in the Shikoku Basin, Nankai Trough, and accretionary prism. *In* Hill, I.A., Taira, A., Firth, J.V., et al., *Proc. ODP, Sci. Results,* 131: College Station, TX (Ocean Drilling Program), 313–330. **doi:10.2973/odp.proc.sr.131.135.1993**

Reeburgh, W.S., 1976. Methane consumption in Cariaco Trench waters and sediments. *Earth Planet. Sci. Lett.,* 28(3):337–344. **doi:10.1016/0012-821X(76)90195-3**

Revil, A., Cathles, L.M., III, Losh, S., and Nunn, J.A., 1998. Electrical conductivity in shaly sands with geophysical applications. *J. Geophys. Res.,* 103(B10):23925–23936. **doi:10.1029/98JB02125**

Saffer, D.M., and Bekins, B.A., 2002. Hydrologic controls on the morphology and mechanics of accretionary wedges. *Geology,* 30(3):271–274. **doi:10.1130/0091-7613(2002)030<0271:HCOTMA>2.0.CO;2**

Screaton, E.J., Wuthrich, D.R., and Dreiss, S.J., 1990. Permeabilities, fluid pressures, and flow rates in the Barbados Ridge complex. *J. Geophys. Res.,* 95(B6):8997–9007. **doi:10.1029/JB095iB06p08997**

Shipboard Scientific Party, 2001a. Site 1175. *In* Moore, G.F., Taira, A., Klaus, A., et al., *Proc. ODP, Init. Repts.,* 190: College Station, TX (Ocean Drilling Program), 1–92. **doi:10.2973/odp.proc.ir.190.106.2001**

Shipboard Scientific Party, 2001b. Site 1176. *In* Moore, G.F., Taira, A., Klaus, A., et al., *Proc. ODP, Init. Repts.,* 190: College Station, TX (Ocean Drilling Program), 1–80. **doi:10.2973/odp.proc.ir.190.107.2001**

Shipboard Scientific Party, 2002. Site 808. *In* Mikada, H., Becker, K., Moore, J.C., Klaus, A., et al., *Proc. ODP, Init. Repts.,* 196: College Station, TX (Ocean Drilling Program), 1–68. **doi:10.2973/odp.proc.ir.196.104.2002**

Tauxe, L., 1998. *Paleomagnetic Principles and Practice:* Dordrecht, Netherlands (Kluwer Acad. Publ.).

Tauxe, L., and Kent, D.V., 1984. Properties of a detrital remanence carried by hematite from study of modern river deposits and laboratory redeposition experiments. *Geophys. J. R. Astron. Soc.,* 76(3):543–561.

Underwood, M.B., Moore, G.F., Taira, A., Klaus, A., Wilson, M.E.J., Fergusson, C.L., Hirano, S., Steurer, J., and the Leg 190 Shipboard Scientific Party, 2003. Sedimentary and tectonic evolution of a trench-slope basin in the Nankai subduction zone of southwest Japan. *J. Sediment. Res.,* 73(4):589–602. **doi:10.1306/092002730589**

Zijderveld, J.D.A., 1967. AC demagnetization of rocks: analysis of results. *In* Collinson, D.W., Creer, K.M., and Runcorn, S.K. (Eds.), *Methods in Palaeomagnetism:* New York (Elsevier), 254–286.

Publication: 5 March 2009
MS 315-123

Figure F1. 3-D seismic inline section showing location of Site C0001. VE = vertical exaggeration.

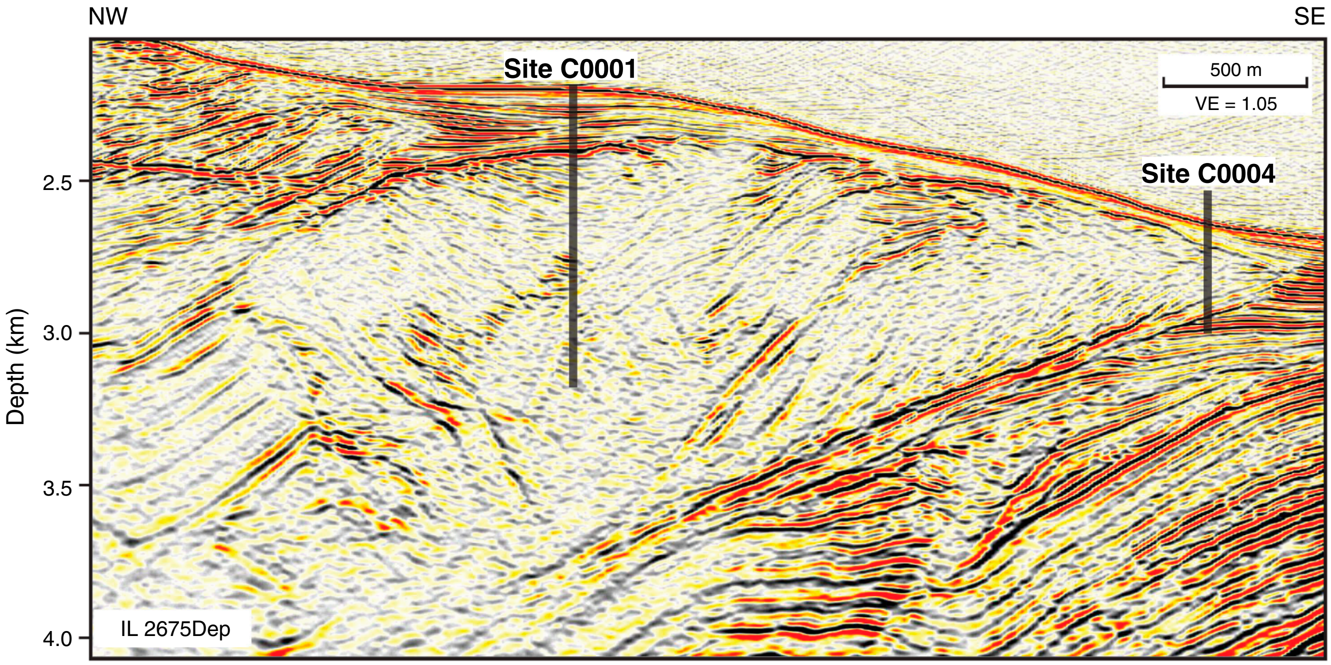

Figure F2. 3-D seismic cross-line section showing location of Site C0001. VE = vertical exaggeration.

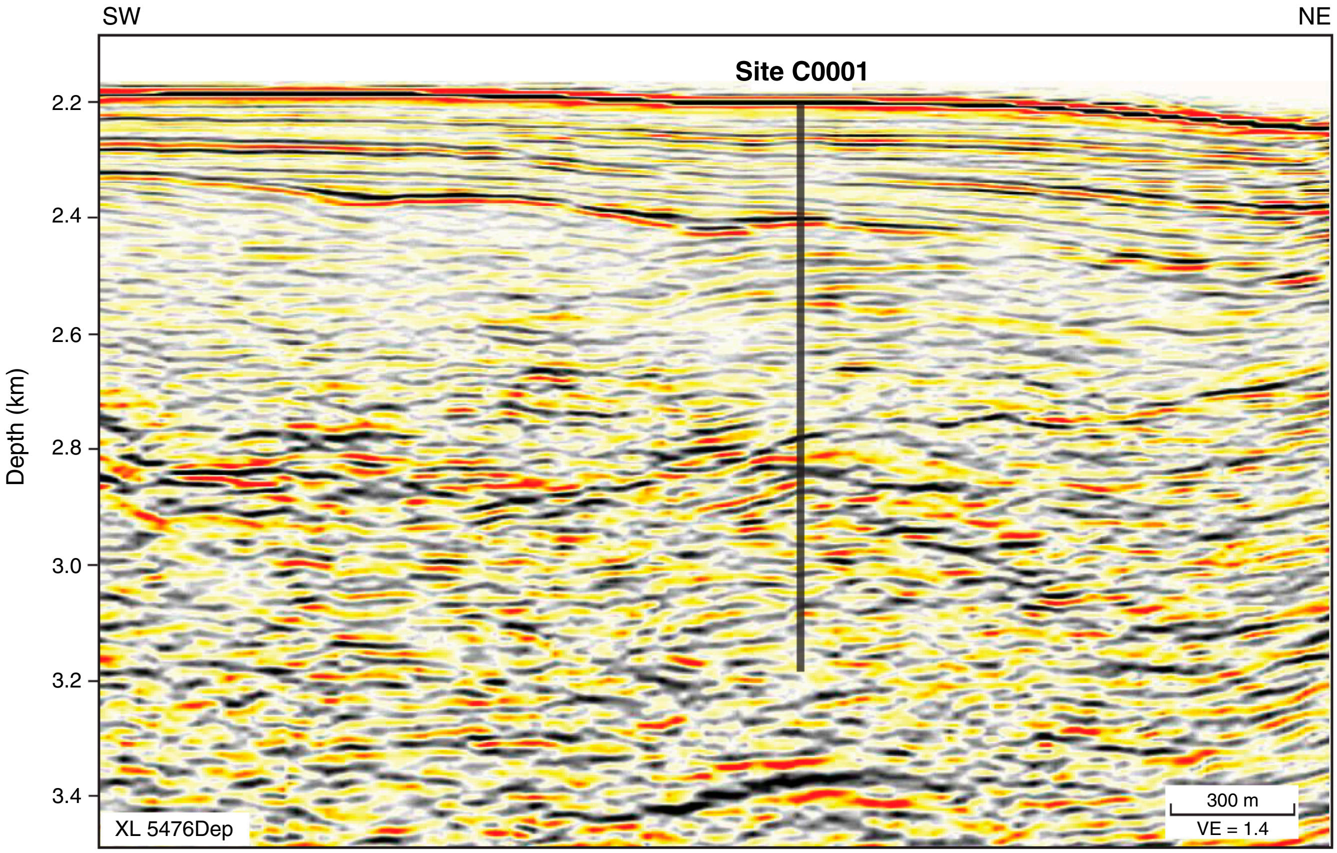

Figure F3. Locations of drill holes, Site C0001. Solid lines = seismic profile coverage.

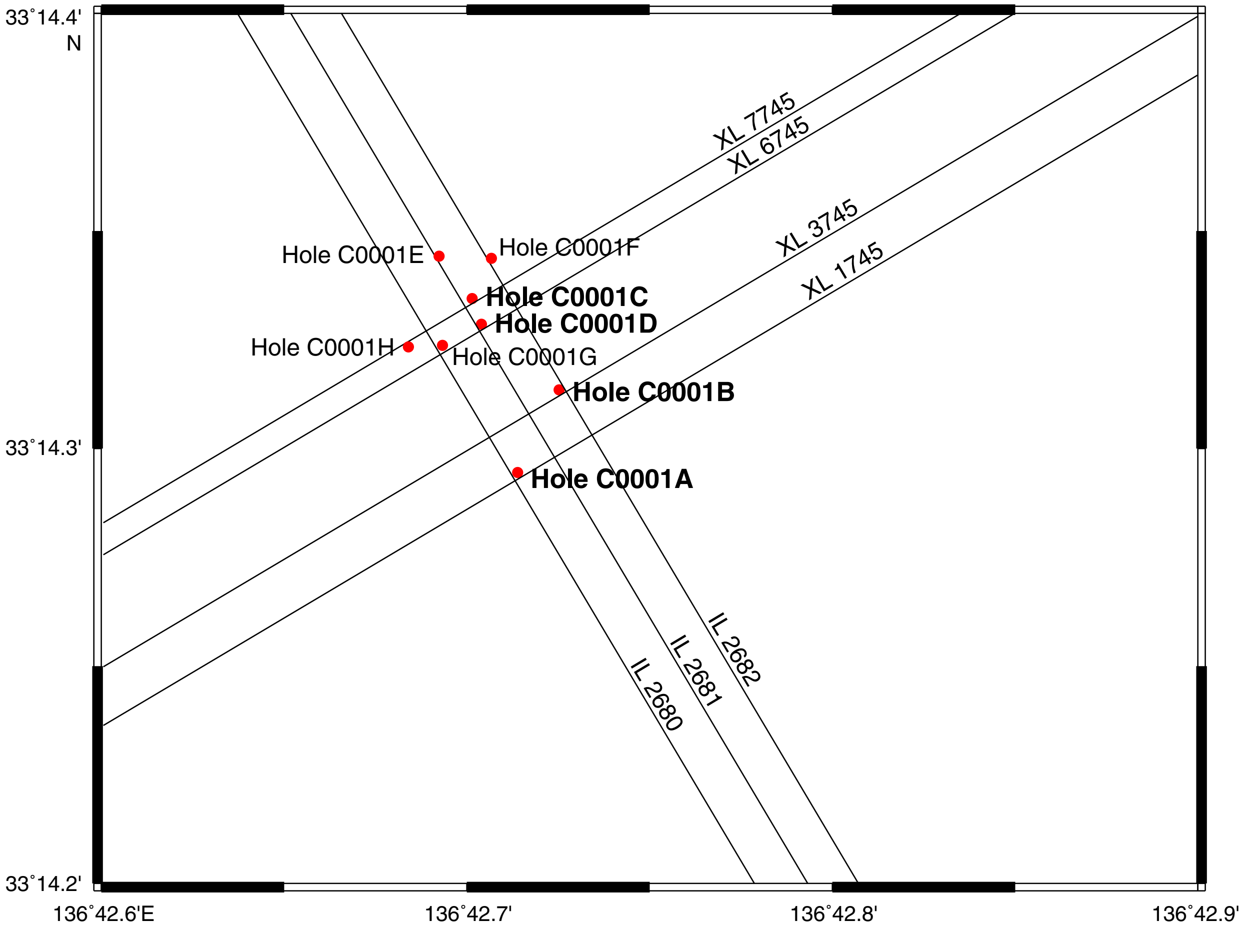

Figure F4. Lithology, Site C0001. CSF = core depth below seafloor.

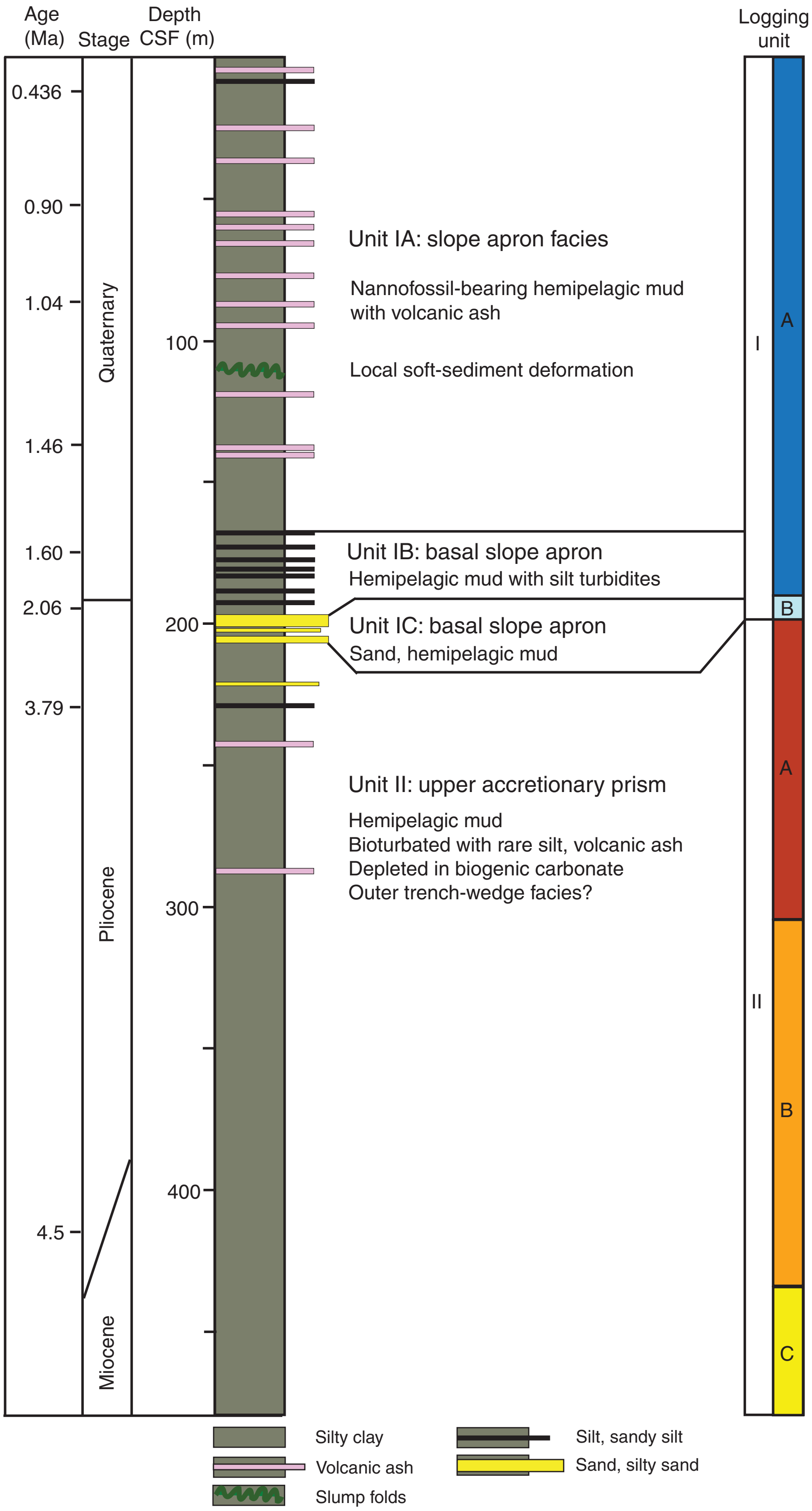

Figure F5. Photomicrographs of biogenic components, Unit I (Sample 315-C0001E-7H-3, 70 cm). **A.** Plane-polarized light. **B.** Cross-polarized light.

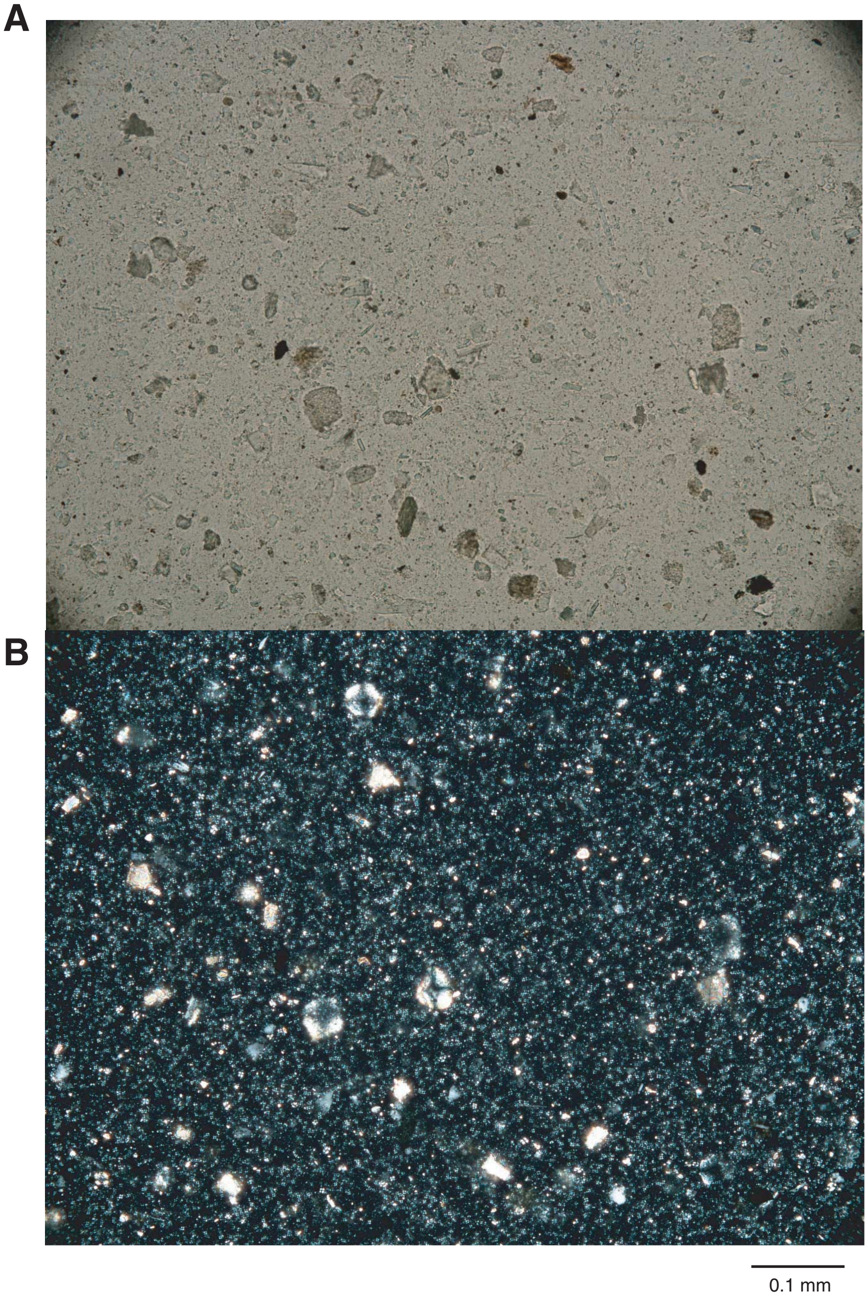

Figure F6. Photographs of ash layers, Subunit IA. **A.** Volcanic dark ash layer (Sample 315-C0001F-9H-2, 67–85 cm). **B.** Volcanic white ash layer (Sample 315-C0001F-9H-6, 117.5–131.5 cm).

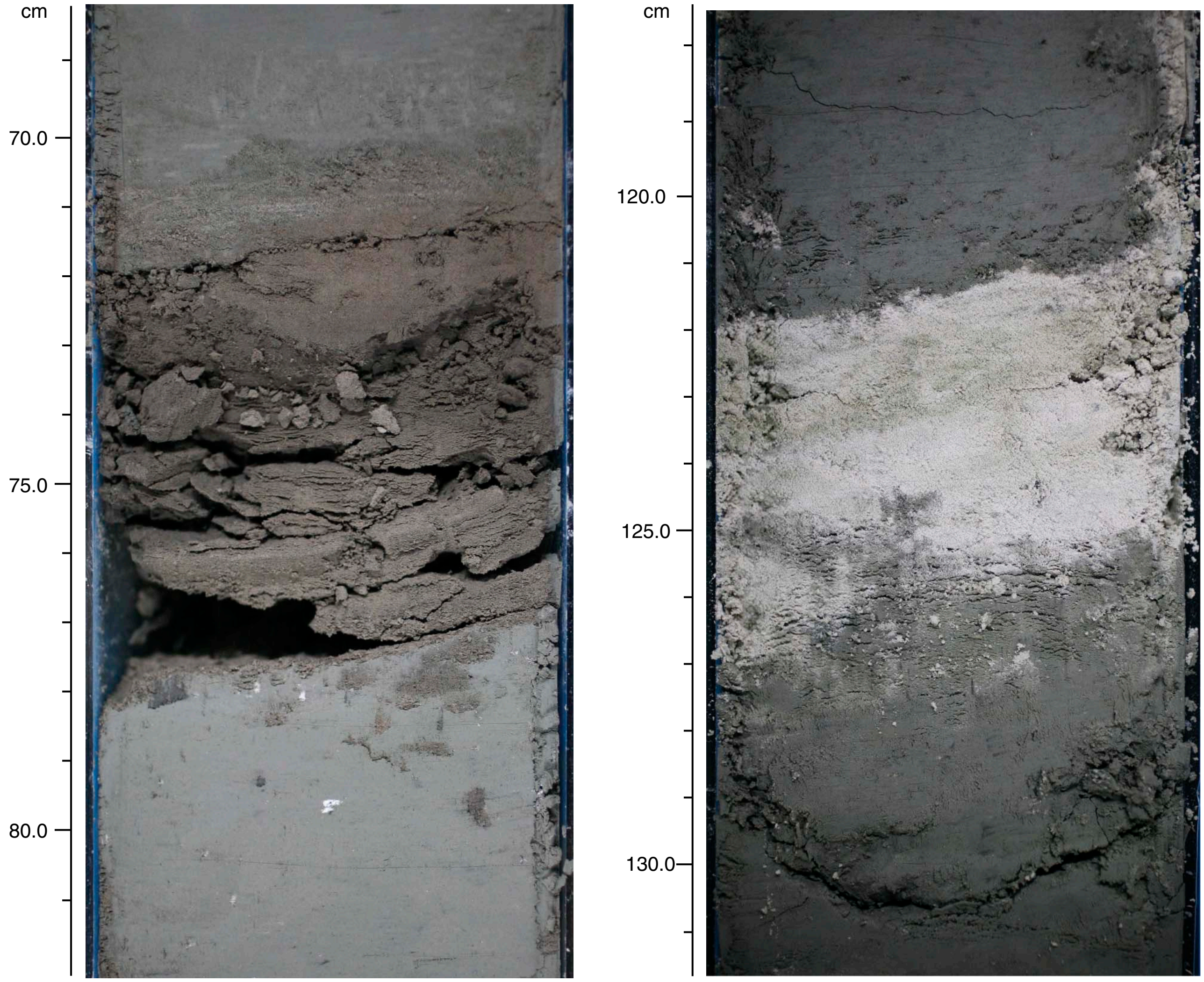

Figure F7. Depth distribution of ash layers and sand-silt beds.

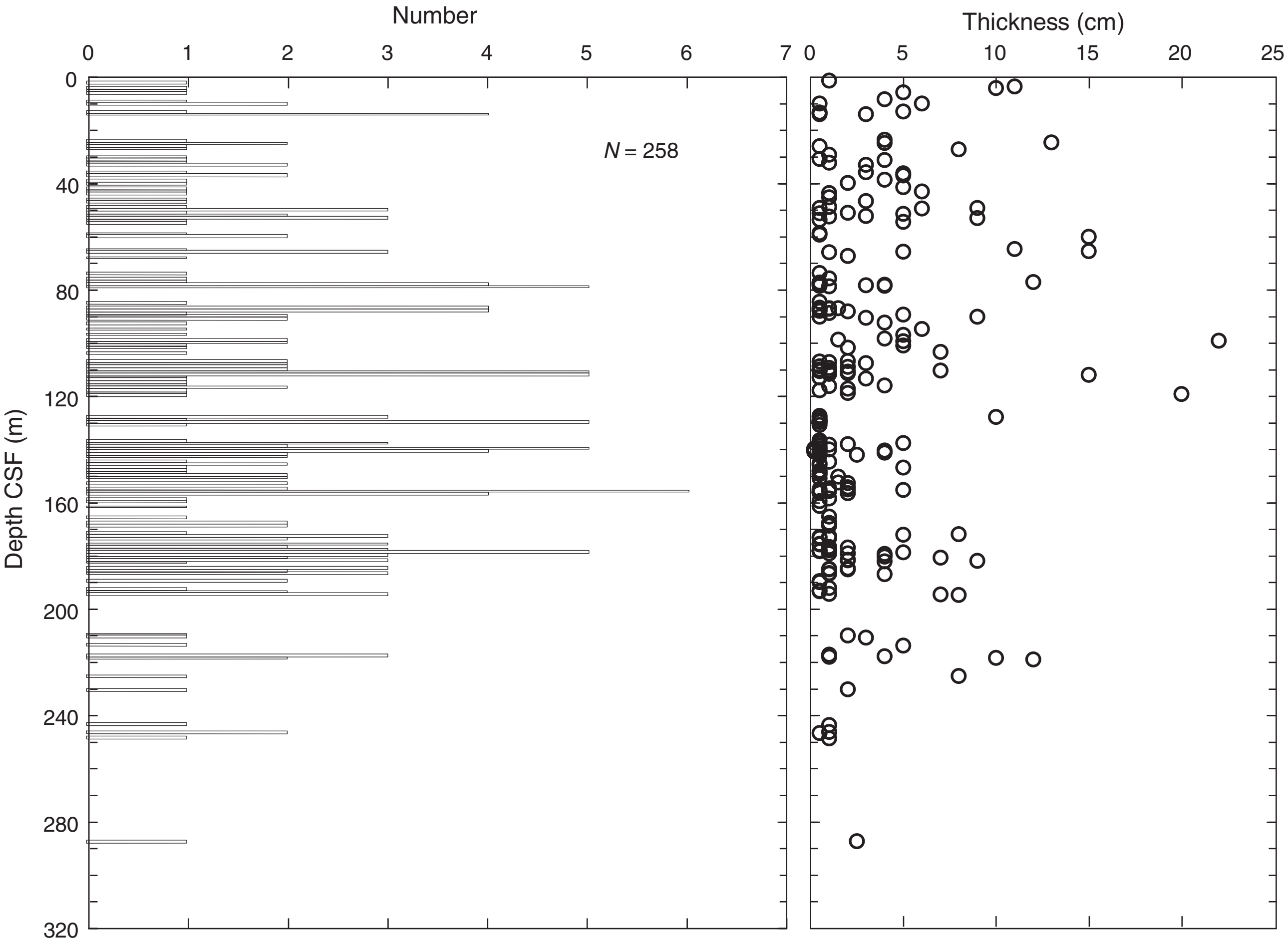

Figure F8. Photomicrographs of sand, Subunit IC (Sample 315-C0001F-11H-1, 9 cm). **A.** Plane-polarized light. **B.** Cross-polarized light.

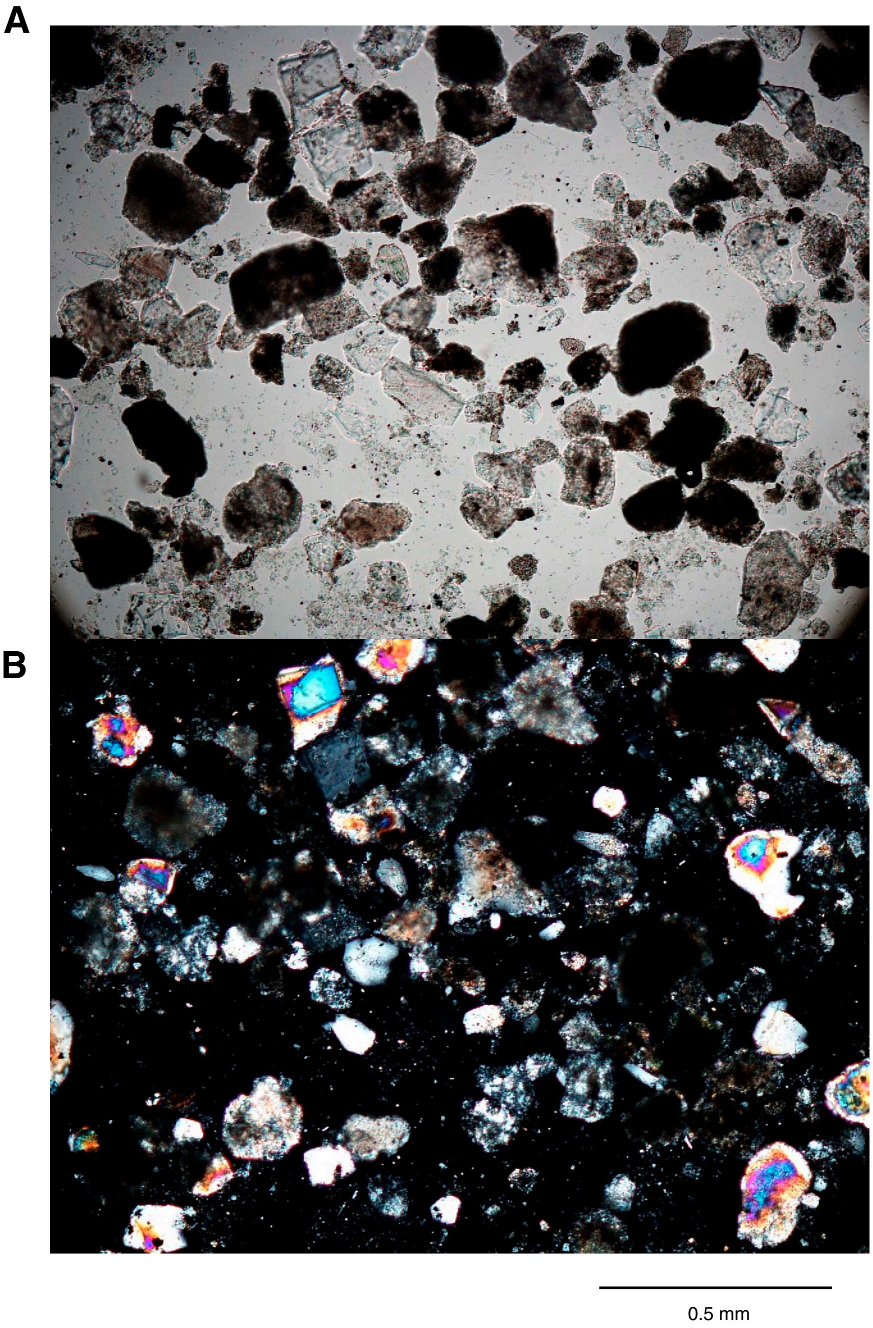

Figure F9. Bulk powder XRD. CSF = core depth below seafloor.

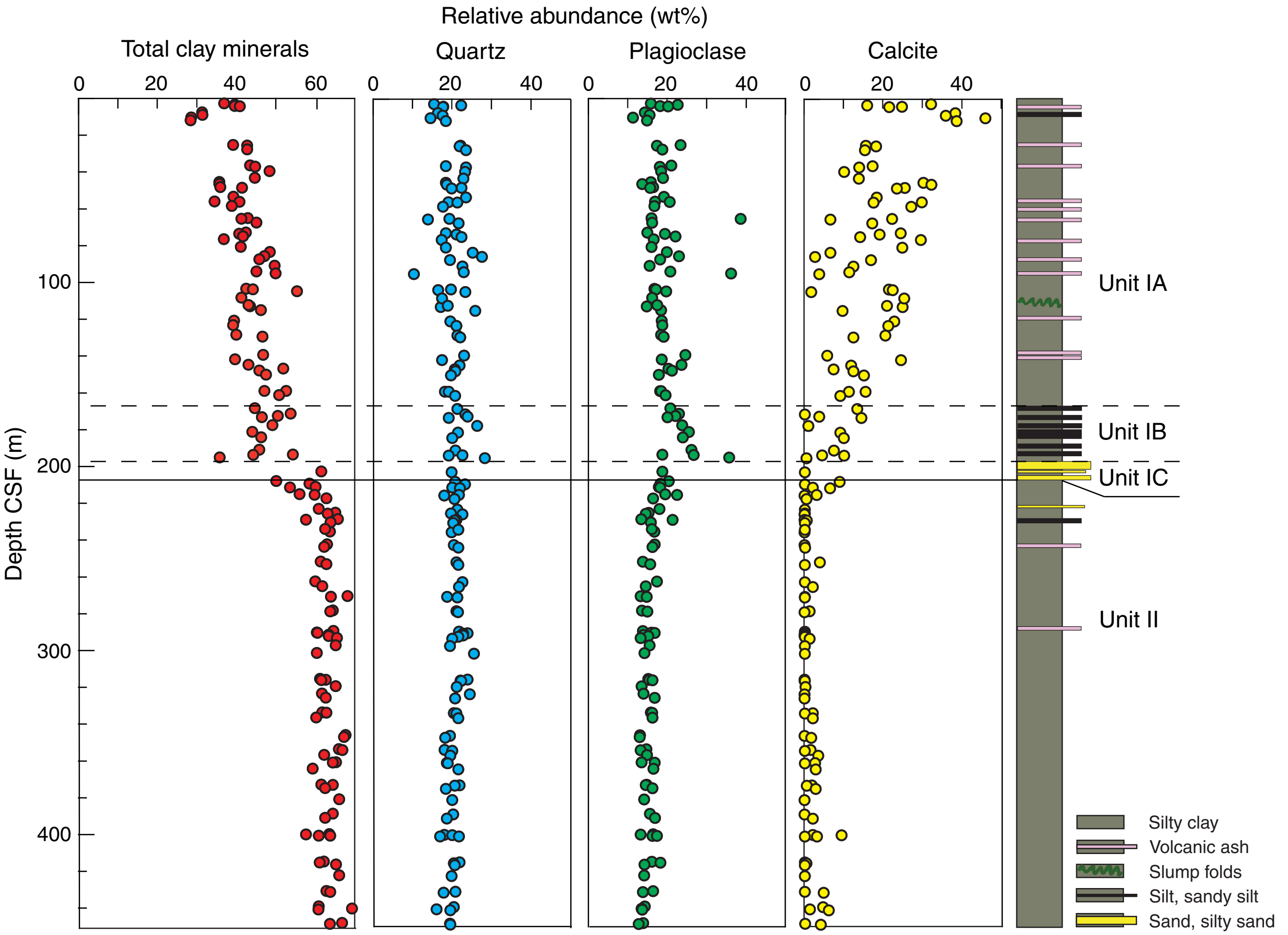

Figure F10. X-ray diffraction (XRD) calcite vs. coulometric carbonate, Site C0001. Dashed line = 1:1 match, solid line = best-fit linear regression. *R* = correlation coefficient.

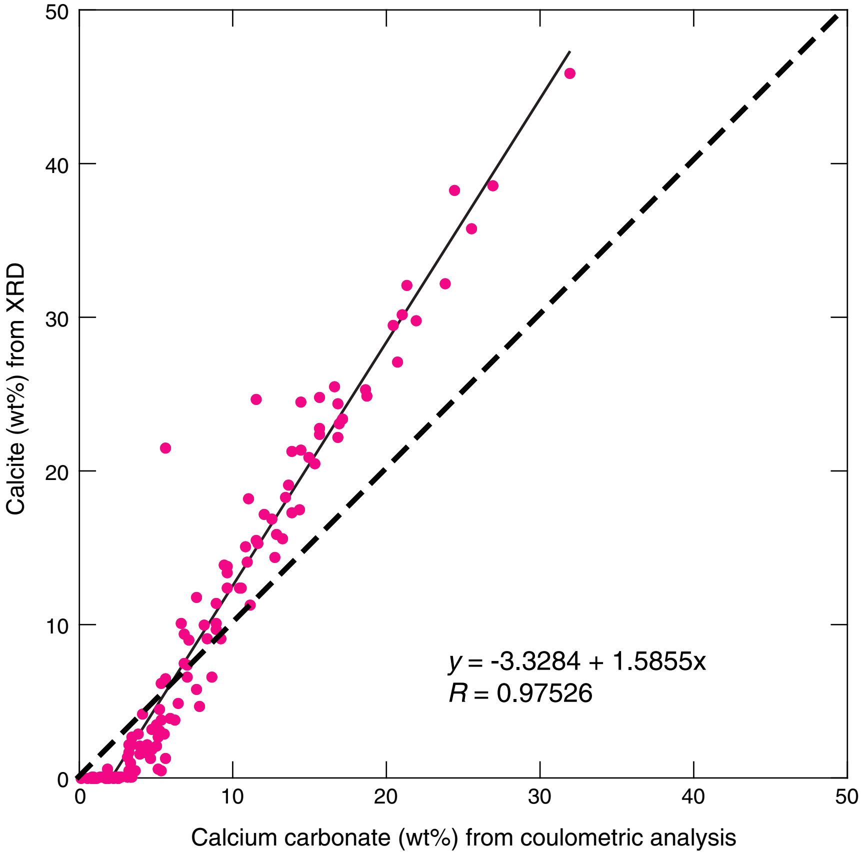

Figure F11. Photographs of faults on core halves. **A.** Normal fault cutting sand beds (interval 315-C0001F-5H-9, 89–103 cm). **B.** CT scan of the normal fault shown in A. **C.** Thrust fault cutting inclined bedding (interval 315-C0001E-10H-1, 73–80 cm). **D.** Slickenlines on a thrust fault plane (interval 315-C0001H-4R-3, 69–71 cm).

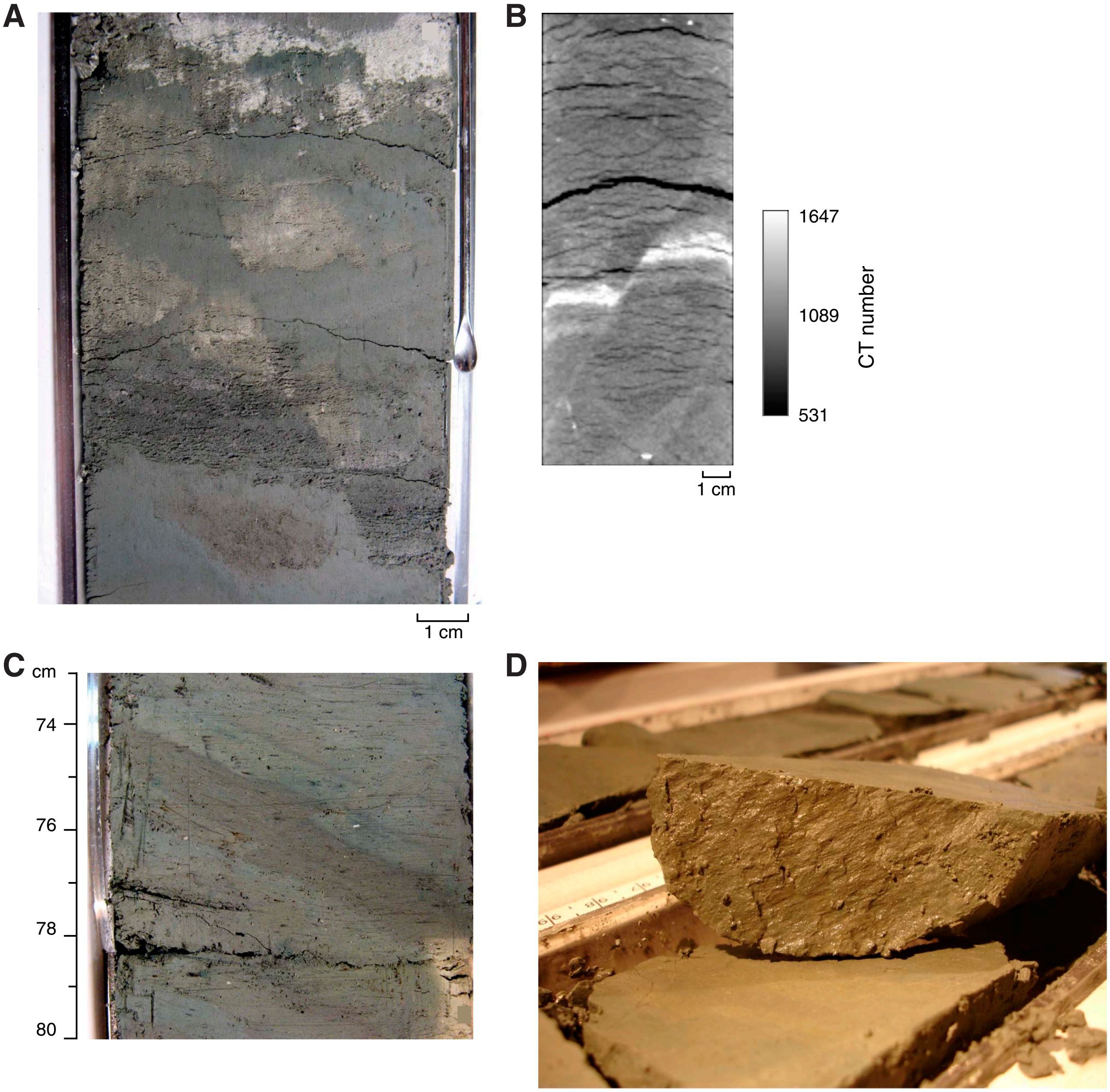

Figure F12. Shear zone structures. **A.** Anastomosing normal shear zone (Section 315-C0001H-11R-6). **B.** Shear zone seen in CT scan. **C.** Photomicrograph of slab section of an anastomosing normal shear zone (interval 315-C0001H-12R-3, 75–102 cm). **D.** Same as C (cross-polarized light with compensation). Clays are preferentially oriented subparallel to shear zone walls. Note coarser and darker infill compared with wall rock.

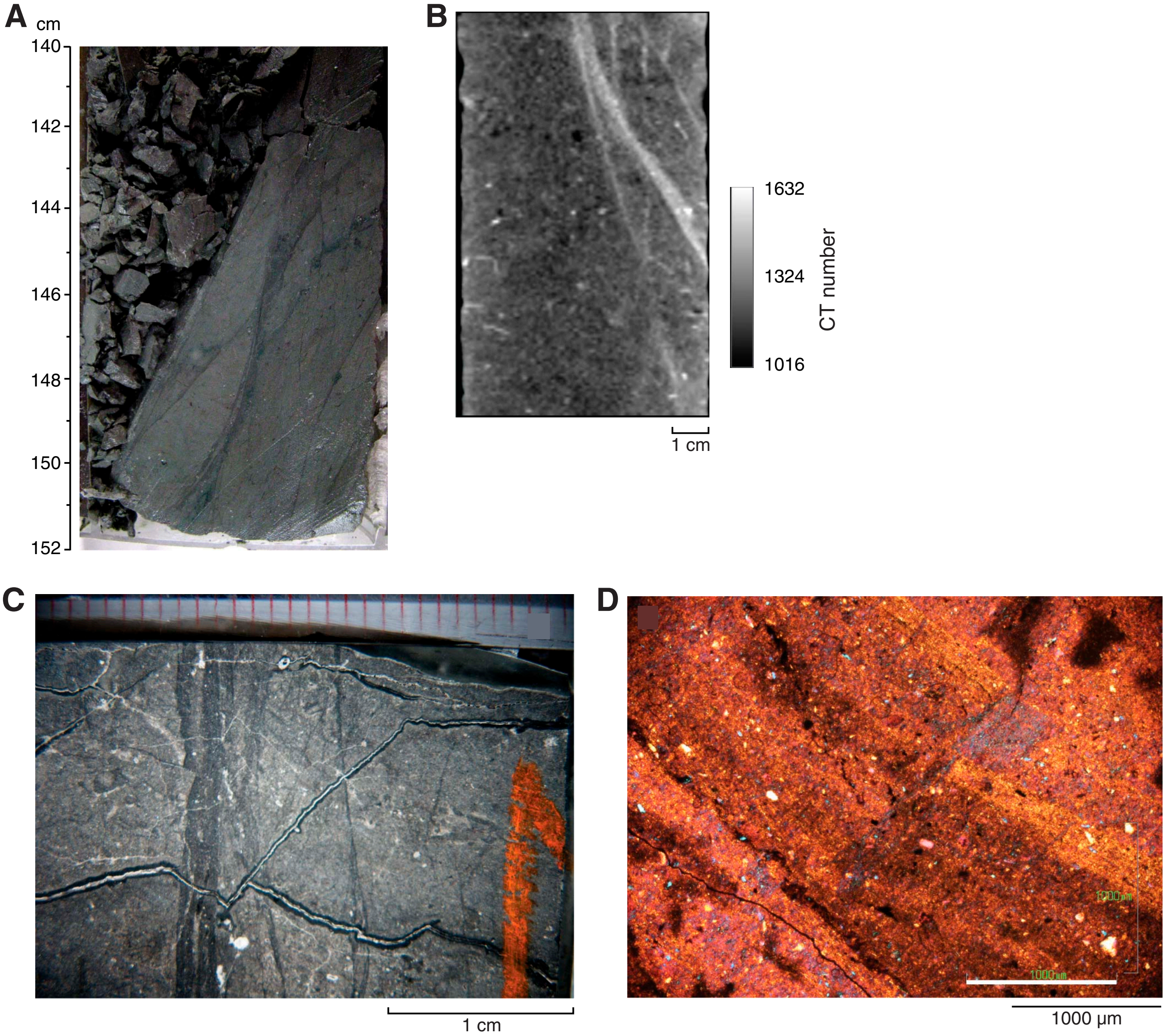

Figure F13. Vein structures. **A.** Archive core half (interval 315-C0001H-13R-2, 90–94 cm). Note black color and regular spacing between bands. **B.** Photomicrograph of slab section (interval 315-C0001H-13R-2, 90–94 cm). Veins are S-shaped, subparallel, branching, and anastomosing, sometimes with a normal offset of bioturbation features. **C.** CT scan image (Section 315-C0001F-15H-5). Veins are brighter, reflective, and therefore denser than the host rock. **D.** Photomicrograph of vein infill (interval 315-C0001H-11R-6, 94–102 cm) (plane-polarized light). Note darker color.

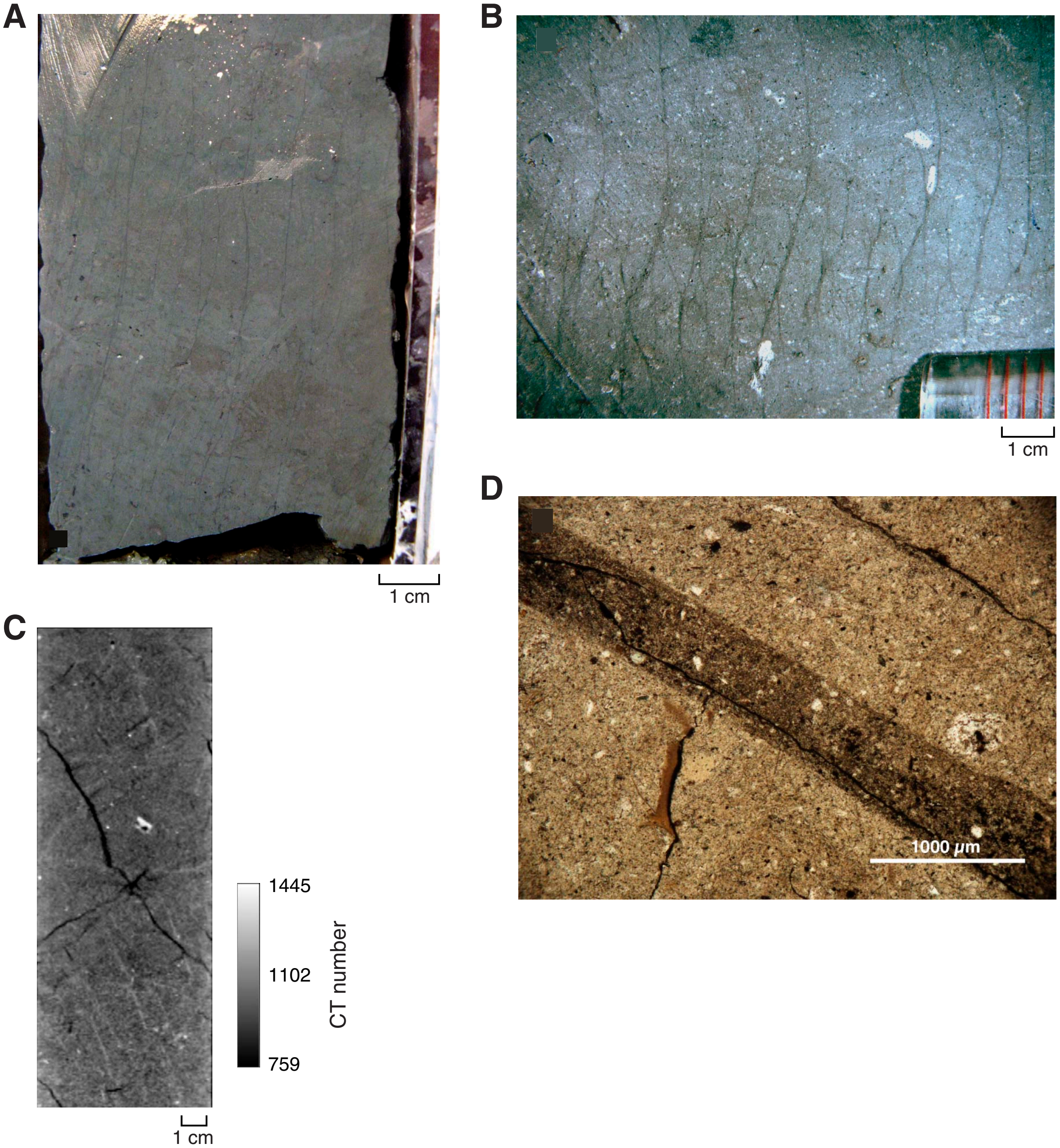

Figure F14. Structural data summary, Site C0001. Red = Hole C0001E, green = Hole C0001F, blue = Hole C0001G. CSF-B = core depth below seafloor, IODP Method B (see the **"Expedition 315 Methods"** chapter).

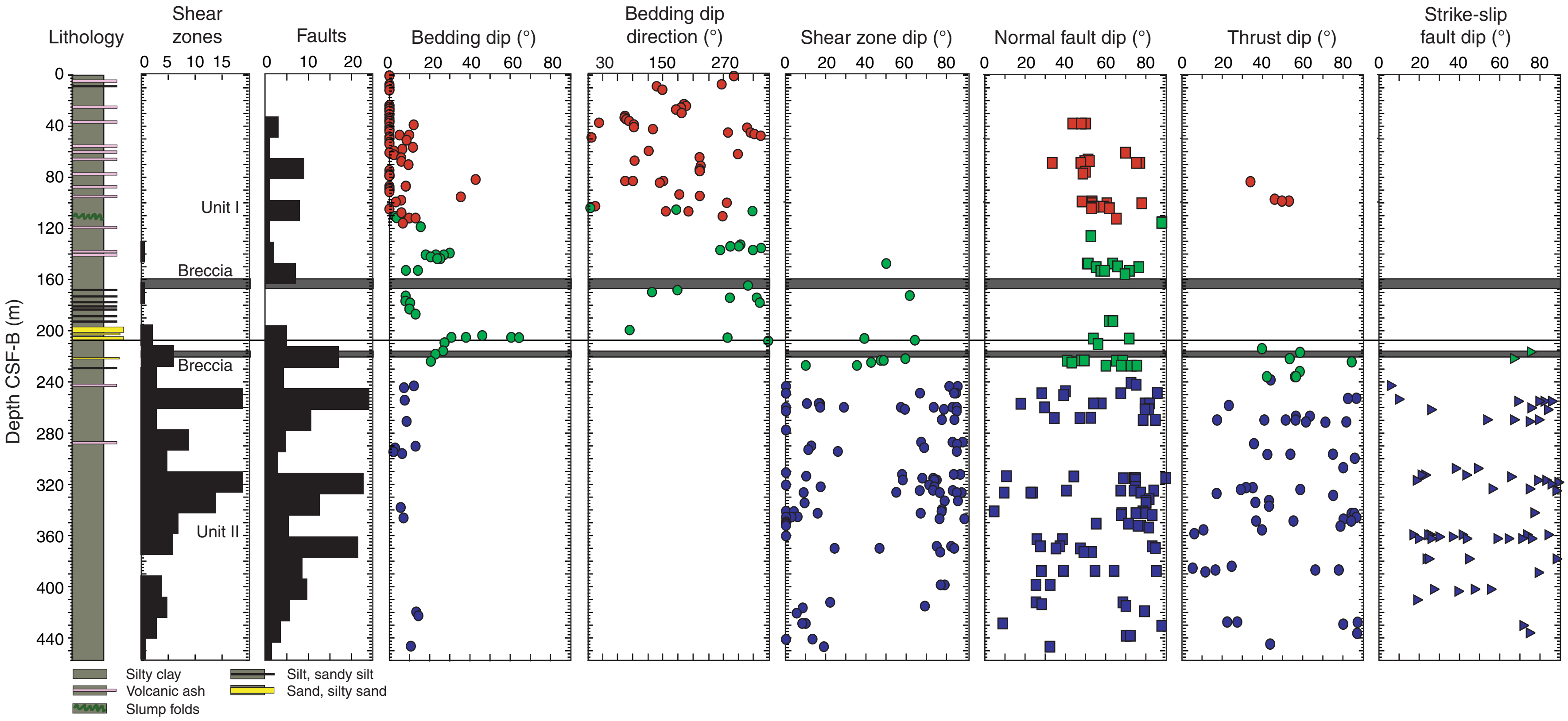

Figure F15. Frequency distribution with depth of faults and shear zones in cores shown on a seismic reflection profile across Site C0001.

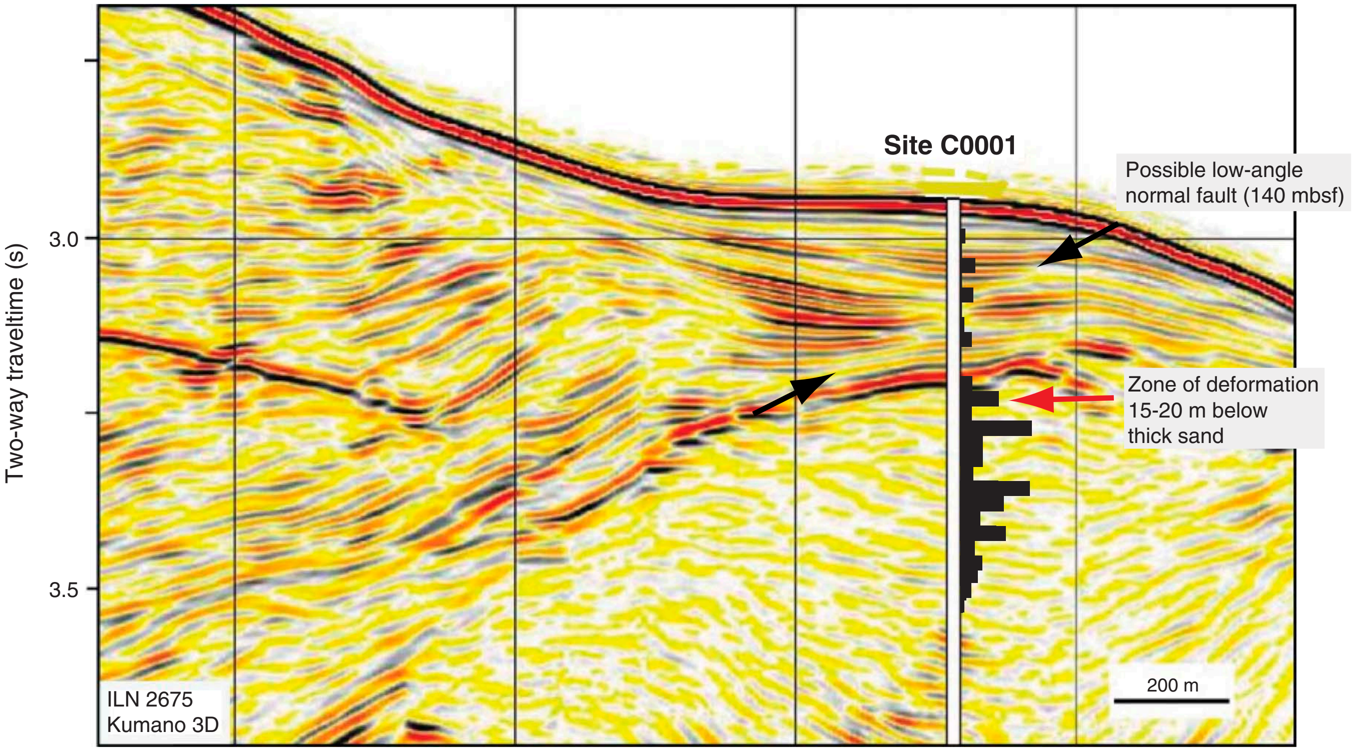

Figure F16. Lower hemisphere, equal area projections of normal faults above ~220 m CSF. **A.** Fault planes (great circles) with striae (dots) and slip vectors (arrows) of the hanging walls relative to the footwalls. Black dots and arrows = data with slickenlines, red dots and arrows = slip directions assumed in the dip directions and slip vectors inferred from offset. **B.** Kinematic solution for the populations of normal faults shown in A with P (compression, red) and T (extension, blue) axes for each fault and compressional (transparent) and associated extensional (gray shaded) quadrants. **C.** Tangent lineations. Arrows = movement direction of footwall with respect to hanging wall.

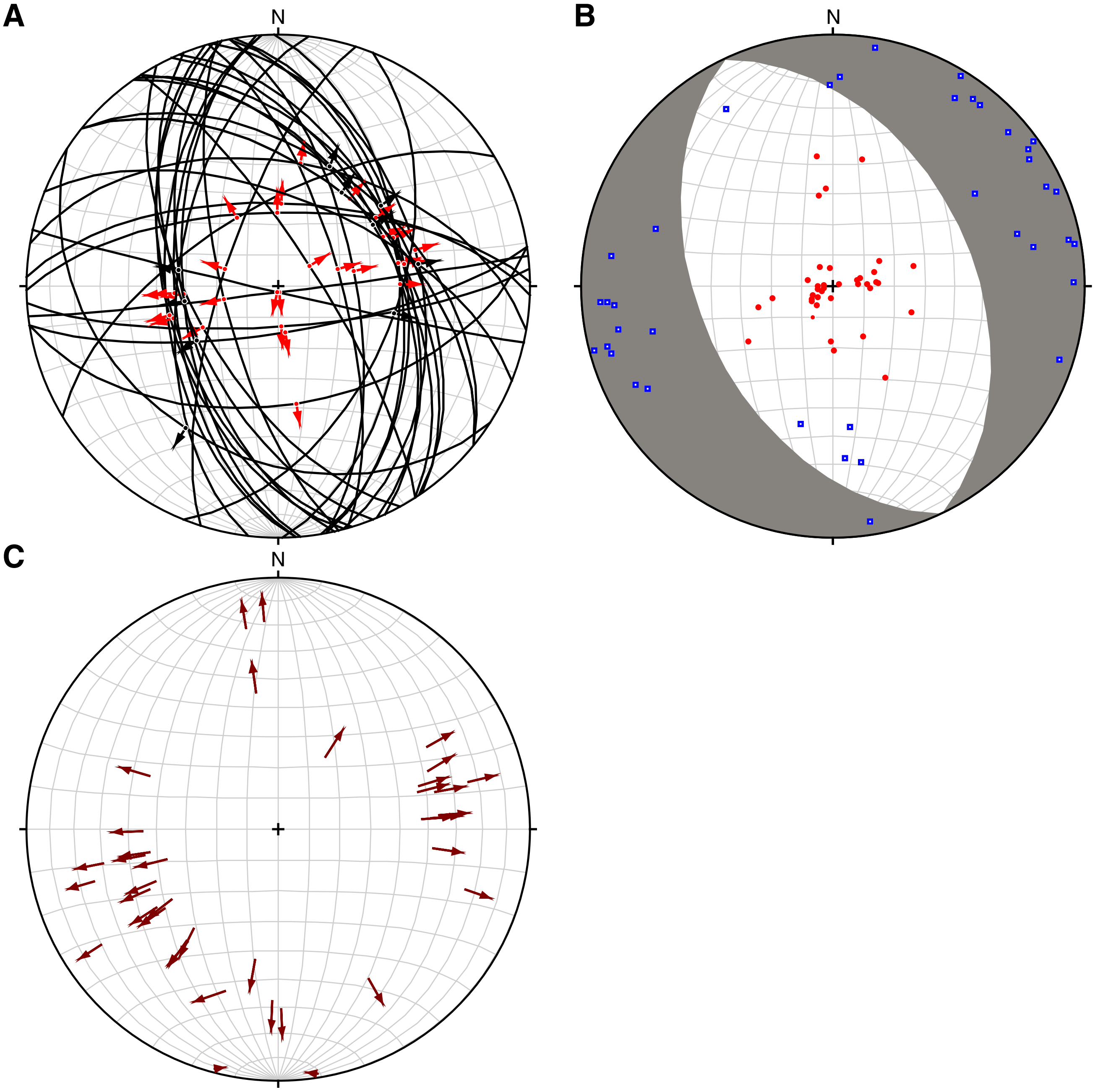

Figure F17. Lower hemisphere, equal area projections of thrust faults above ~220 m CSF and their kinematic solutions. **A.** Fault planes (great circles) with striae (dots) and slip vectors (arrows) of the hanging walls relative to the footwalls. Black dots and arrows = data with slickenlines, red dots and arrows = slip directions assumed in the dip directions and slip vectors inferred from offset. **B.** Kinematic solution for the populations of thrust faults shown in A with P (compression, red) and T (extension, blue) axes for each fault and compressional (transparent) and associated extensional (gray shaded) quadrants. **C.** Tangent lineations. Arrows = movement direction of footwall with respect to hanging wall.

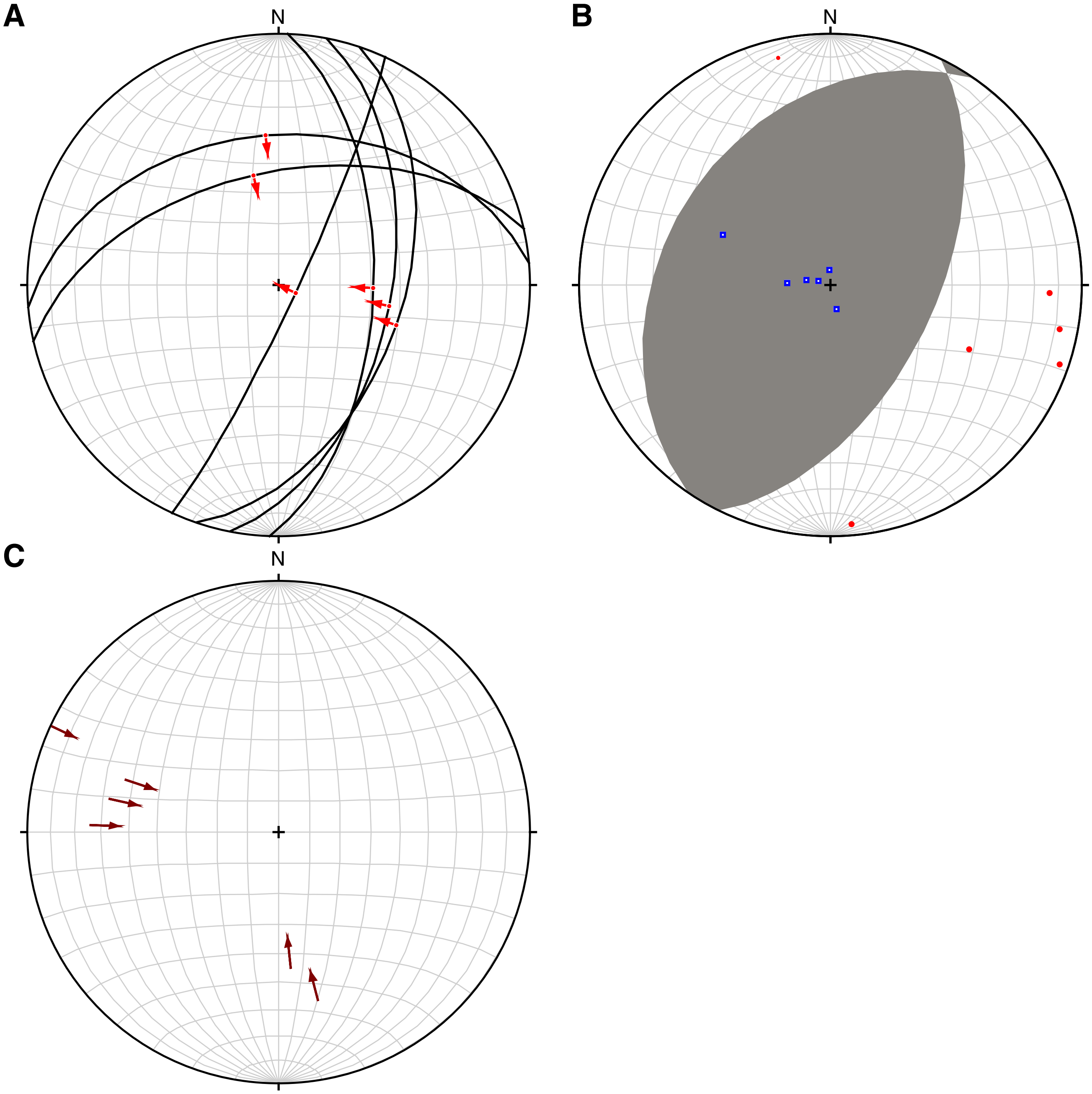

Figure F18. Lower hemisphere, equal area projections of normal faults below ~220 m CSF and their kinematic solutions. **A.** Fault planes (great circles) with striae (dots) and slip vectors (arrows) of the hanging walls relative to the footwalls. Black dots and arrows = data with slickenlines, red dots and arrows = slip directions assumed in the dip directions and slip vectors inferred from offset. **B.** Kinematic solution for the populations of normal faults shown in A with P (compression, red) and T (extension, blue) axes for each fault and compressional (transparent) and associated extensional (gray shaded) quadrants. **C.** Tangent lineations. Arrows = movement direction of footwall with respect to hanging wall.

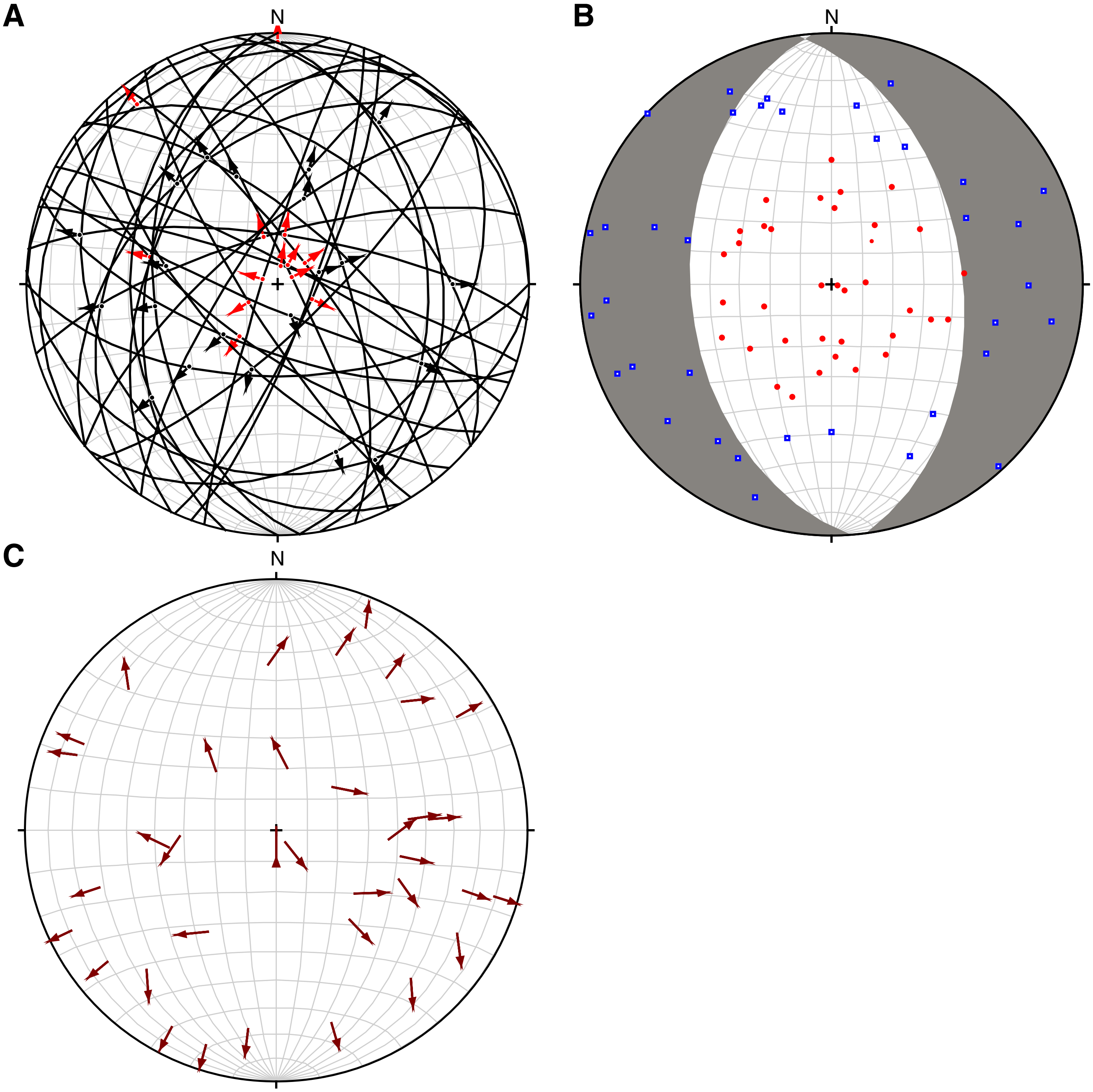

Figure F19. Lower hemisphere, equal area projections of thrust faults below ~220 m CSF and their kinematic solutions. **A.** Fault planes (great circles) with striae (dots) and slip vectors (arrows) of the hanging walls relative to the footwalls. Black dots and arrows = data with slickenlines, red dots and arrows = slip directions assumed in the dip directions and slip vectors inferred from offset. **B.** Kinematic solution for the populations of normal faults shown in A with P (compression, red) and T (extension, blue) axes for each fault and compressional (transparent) and associated extensional (gray shaded) quadrants. **C.** Tangent lineations. Arrows = movement direction of footwall with respect to hanging wall.

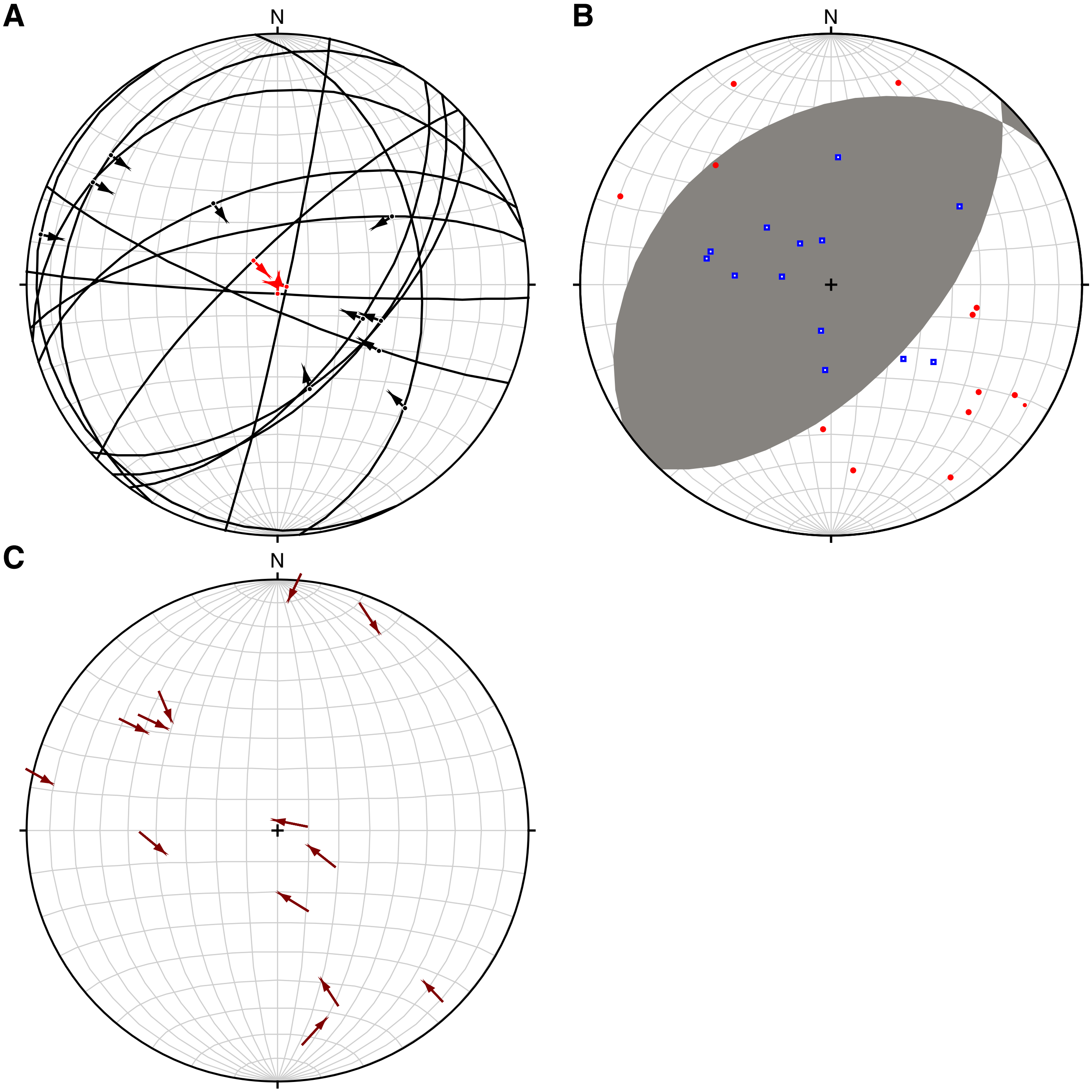

Figure F20. Lower hemisphere, equal area projections of shallow-dipping (<50°) strike-slip faults below the deformed zone. **A.** Fault planes (great circles) with striae (dots) and slip vectors (arrows) of the hanging walls relative to the footwalls. **B.** Tangent lineations. Arrows = movement direction of footwall with respect to hanging wall.

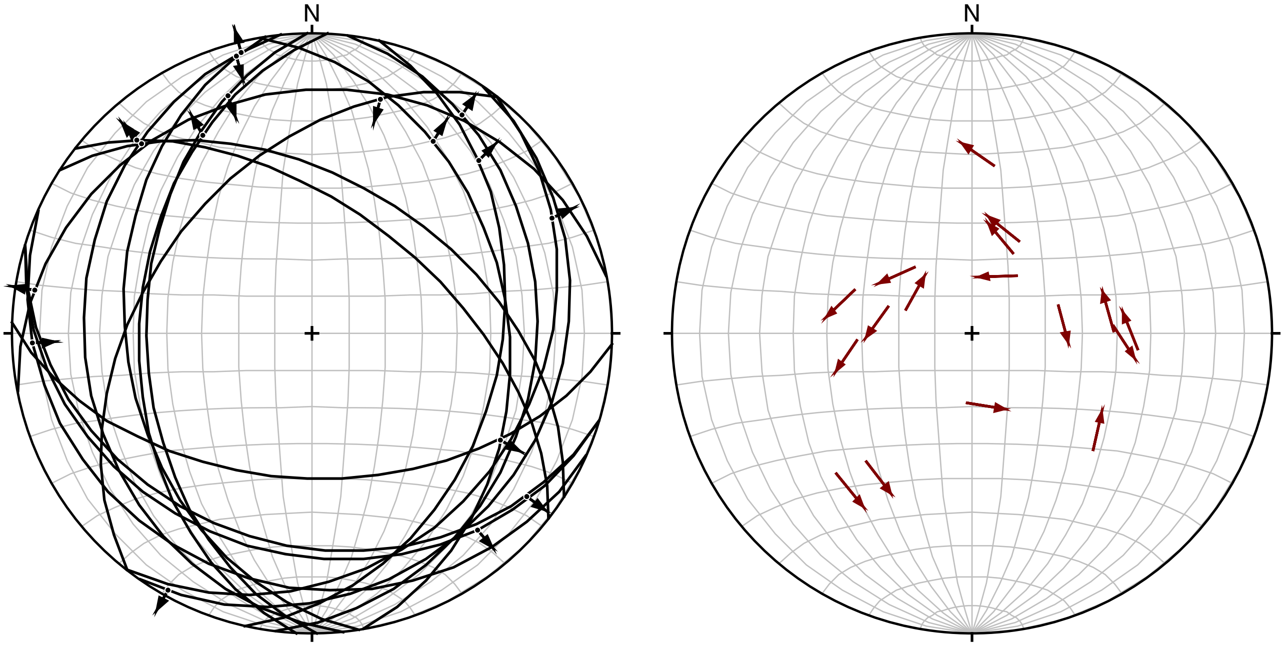

Figure F21. Lower hemisphere, equal area projections of steeply dipping (?50°) strike-slip faults below the deformed zone and their kinematic solutions. **A.** Fault planes (great circles) with striae (dots) and slip vectors (arrows) of the hanging walls relative to the footwalls. Black dots and arrows = data with slickenlines, red dots and arrows = slip directions assumed in the dip directions and slip vectors inferred from offset. **B.** Kinematic solution for the populations of strike-slip faults shown in A with P (compression, red) and T (extension, blue) axes for each fault and compressional (transparent) and associated extensional (gray shaded) quadrants. **C.** Tangent lineations. Arrows = movement direction of footwall with respect to hanging wall.

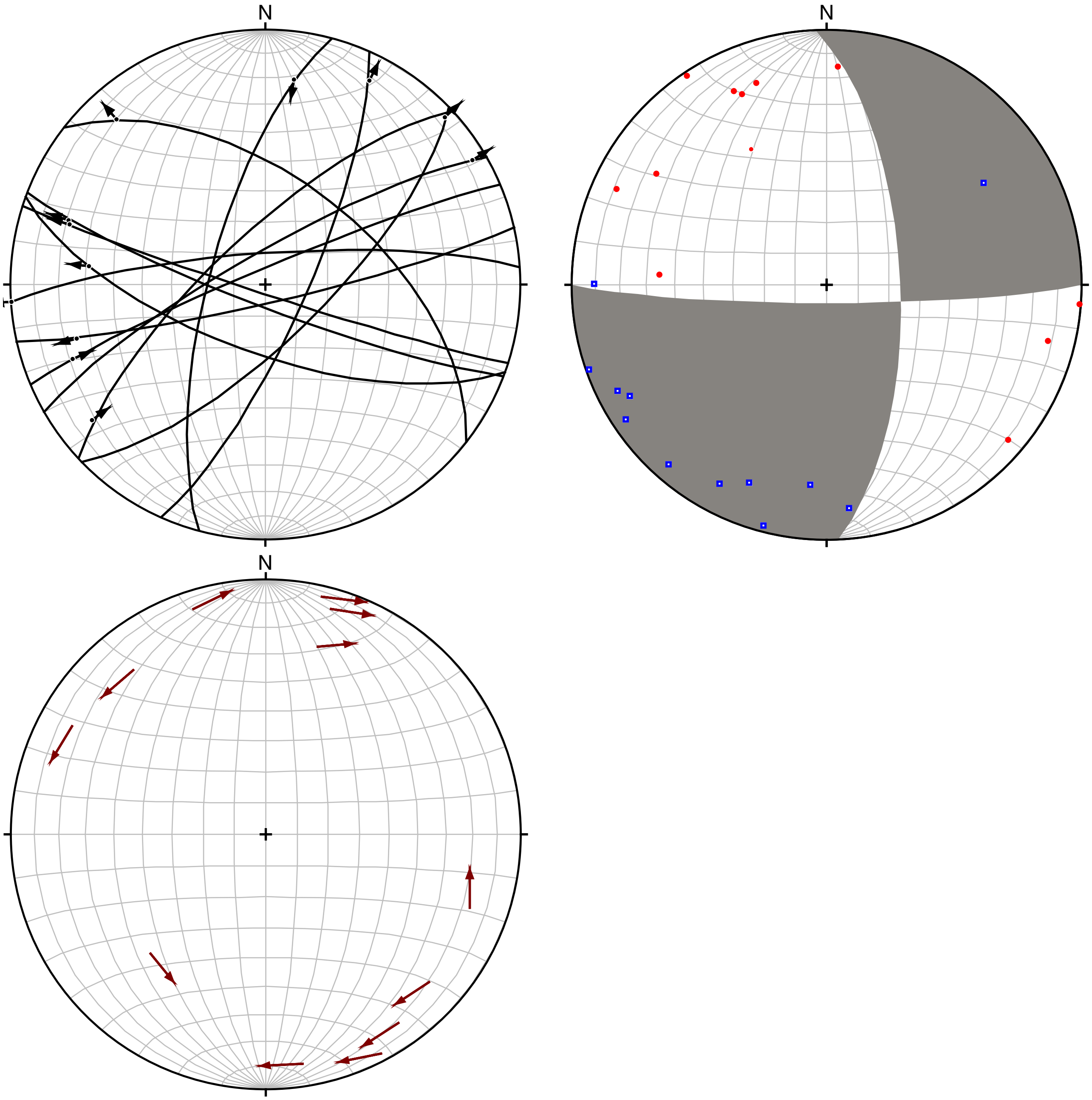

Figure F22. One possible interpretation of kinematic data. **A.** Stress field imposed by southeast–northwest plate convergence. **B, C.** Lithostatic load becomes progressively dominant, causing first a permutation of the σ_2 and σ_3 principal stress axes, and then between the σ_2 and σ_1 principal stress axes. Vertical principal stress axes are not shown.

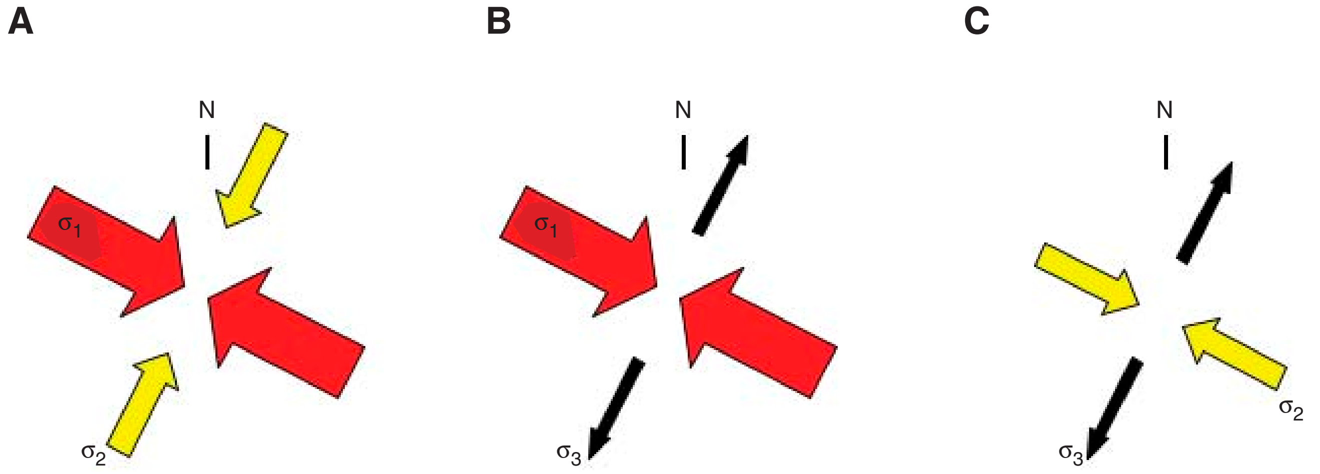

Figure F23. Biostratigraphic age model. Gray area = biostratigraphic gap. CSF = core depth below seafloor.

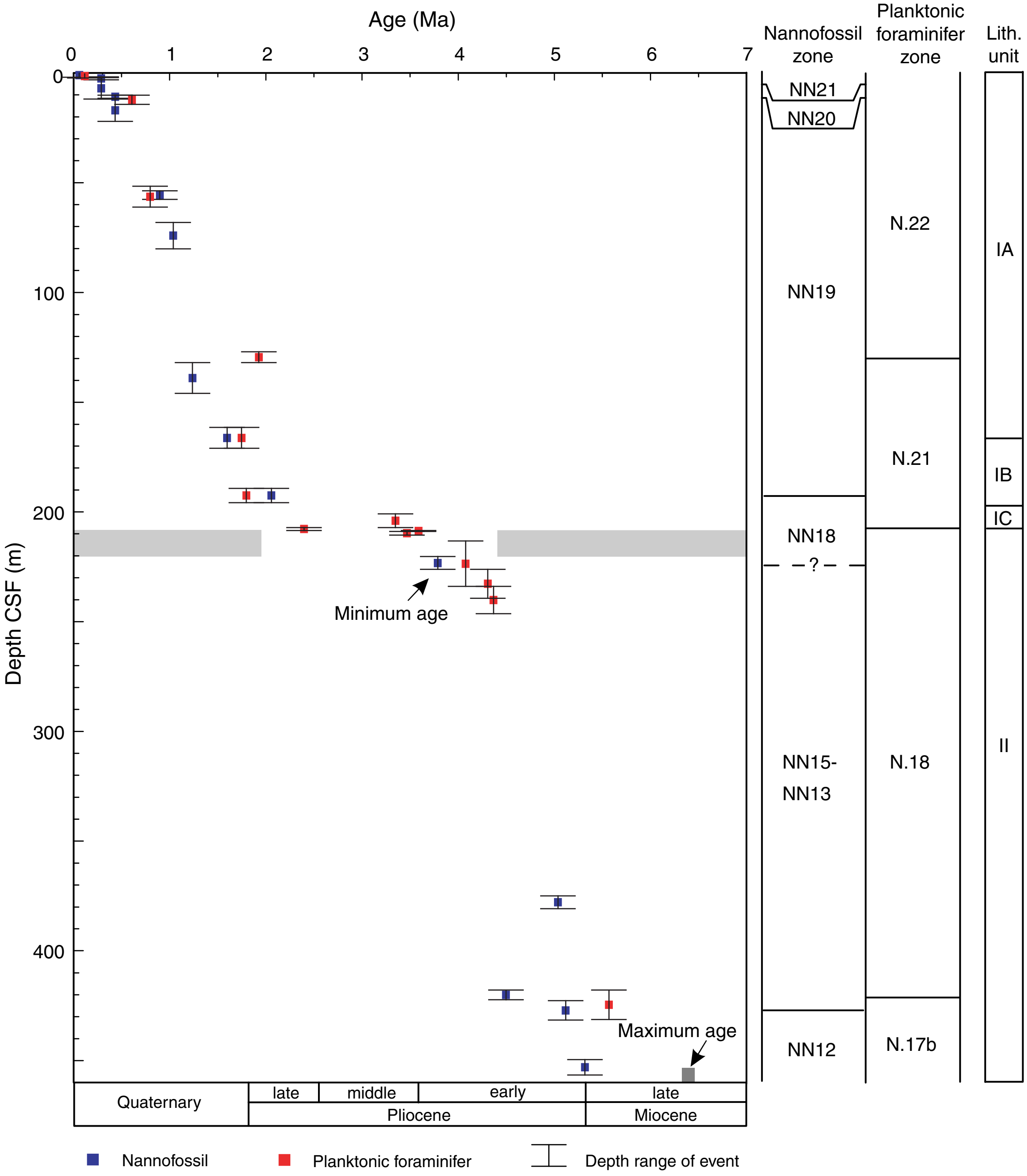

Figure F24. Lower hemisphere equal area projection of natural remanent magnetization (NRM) and 20 mT demagnetized directions, Section 315-C0001E-4H-7. N = direction of the single line at the bottom of the archive half (see Fig. **F18** in the "Expedition 315 methods" chapter). NRM directions are biased toward steep inclinations because of drilling-induced magnetization. Note remanent magnetization directions after blanket AF demagnetization at 20 mT are much more scattered.

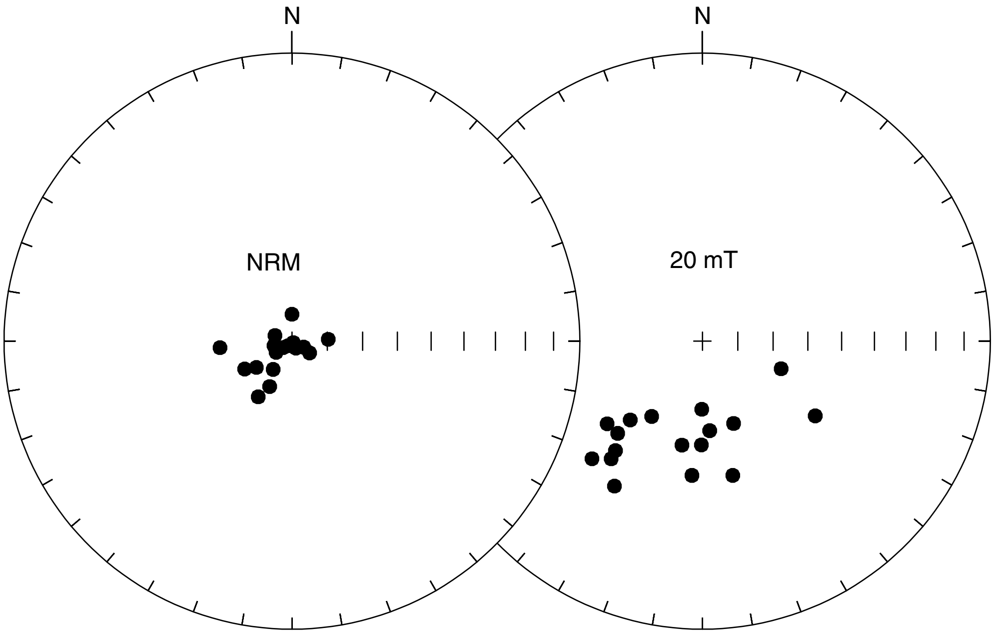

Figure F25. Magnetic intensity before (black) and after (red) AF demagnetization at 20 mT, Holes C0001E and C0001F. Blue = magnetic susceptibility. CSF = core depth below seafloor.

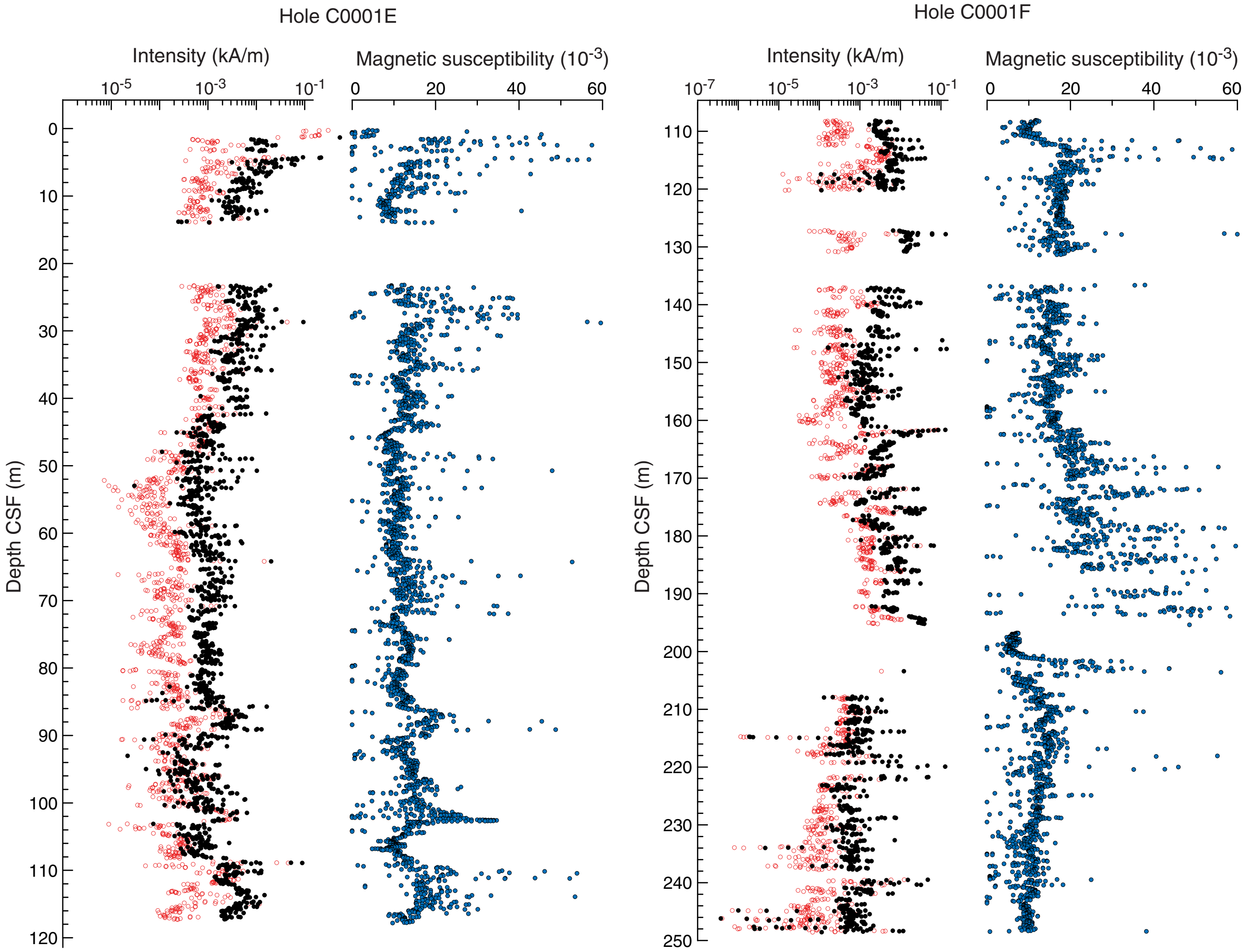

Figure F26. Section averaged directions and normal and reversed inclinations, Holes C0001E and C0001F. N = direction of the single line at the bottom of the archive half (see Fig. F18 in the "Expedition 315 methods" chapter), Inc = mean inclination (obtained using the method of McFadden and Reid [1982] with "incfish" program; Tauxe, 1998).

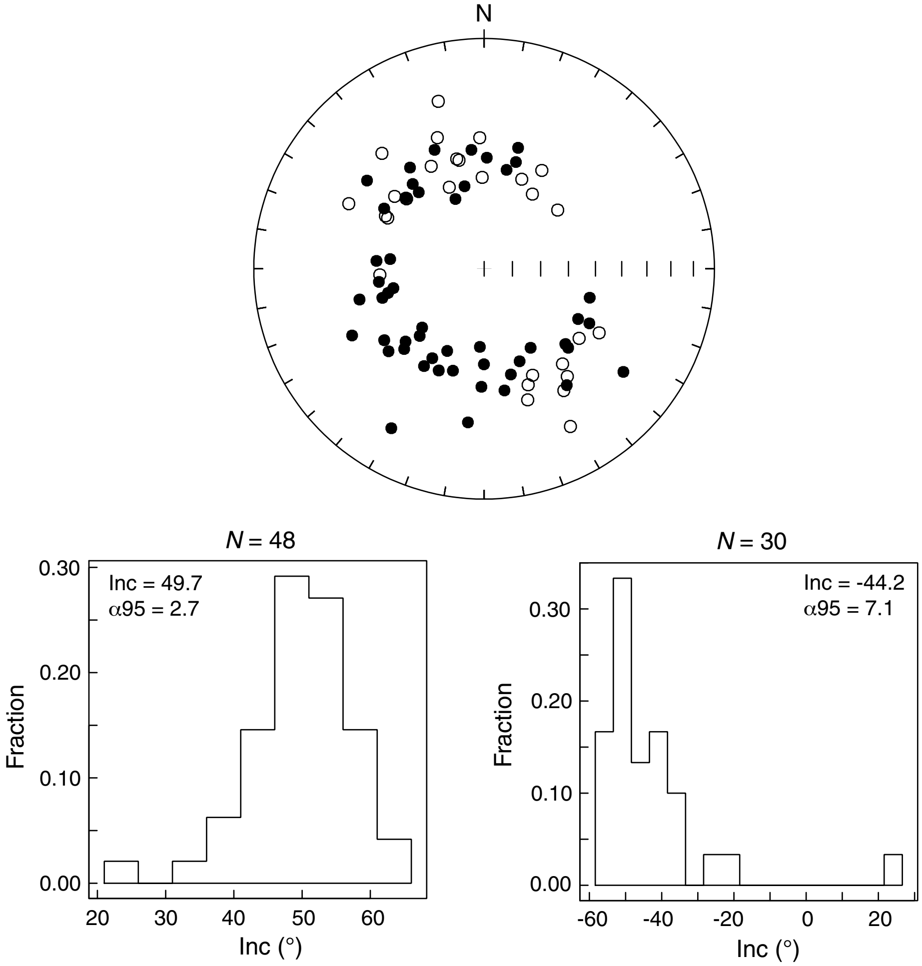

Figure F27. Lower hemisphere equal area projection of directions after 20 mT demagnetization of each section of Core 315-C0001E-5H. N = direction of the single line at the bottom of the archive half (see Fig. **F18** in the "Expedition 315 methods" chapter), arrows = mean declination. Note change of mean declination with depth.

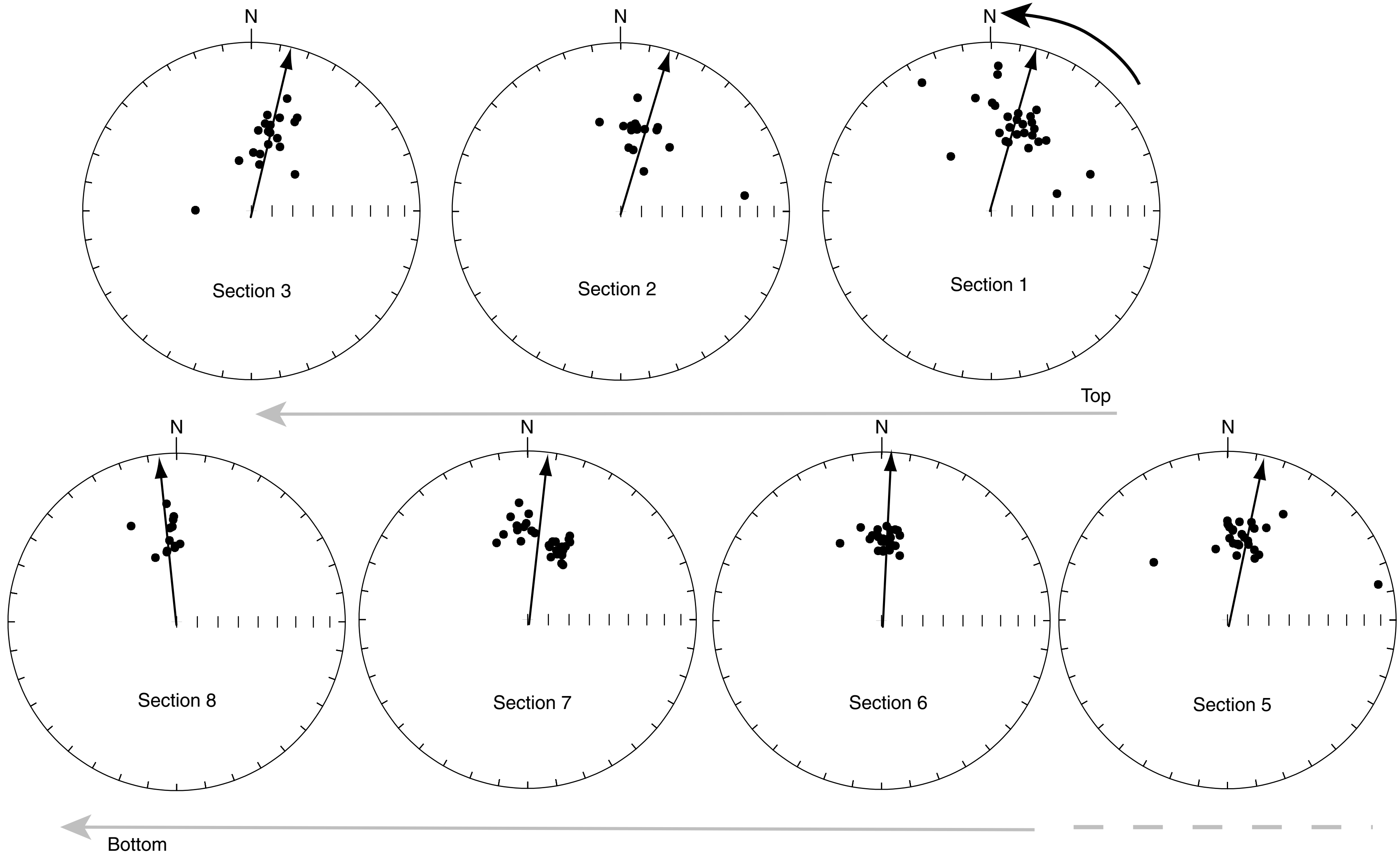

Figure F28. Severe core twisting in Section 315-C0001F-7H-4, as indicated by progressive change in declination. See discussion in text.

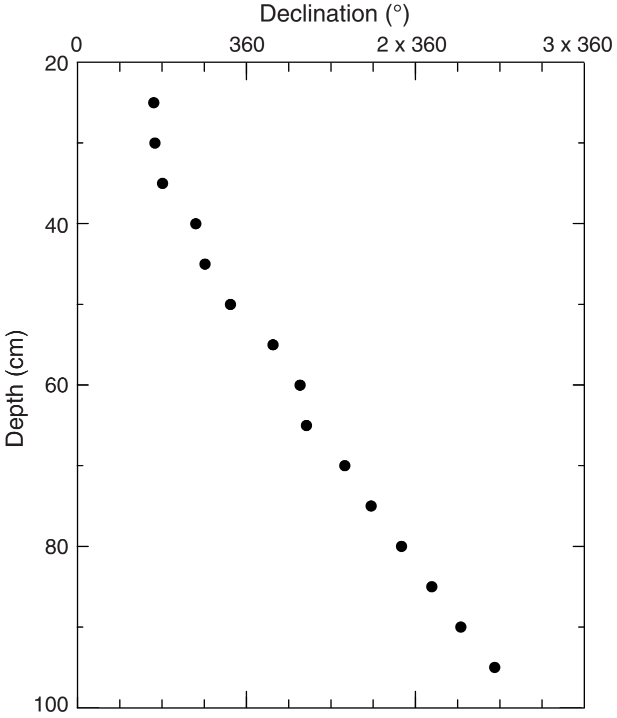

Figure F29. Lower hemisphere equal area projection of dispersion of magnetization direction before and after demagnetization, Sections 315-C0001F-1H-2 and 315-C0001F-7H-4. N = direction of the single line at the bottom of the archive half (see Fig. F18 in the "Expedition 315 methods" chapter). Top diagrams show clustering of natural remanent magnetization (NRM) directions, with a downward and very steep mean direction. Remanence directions after 20 mT show a larger dispersion interpreted as core twisting.

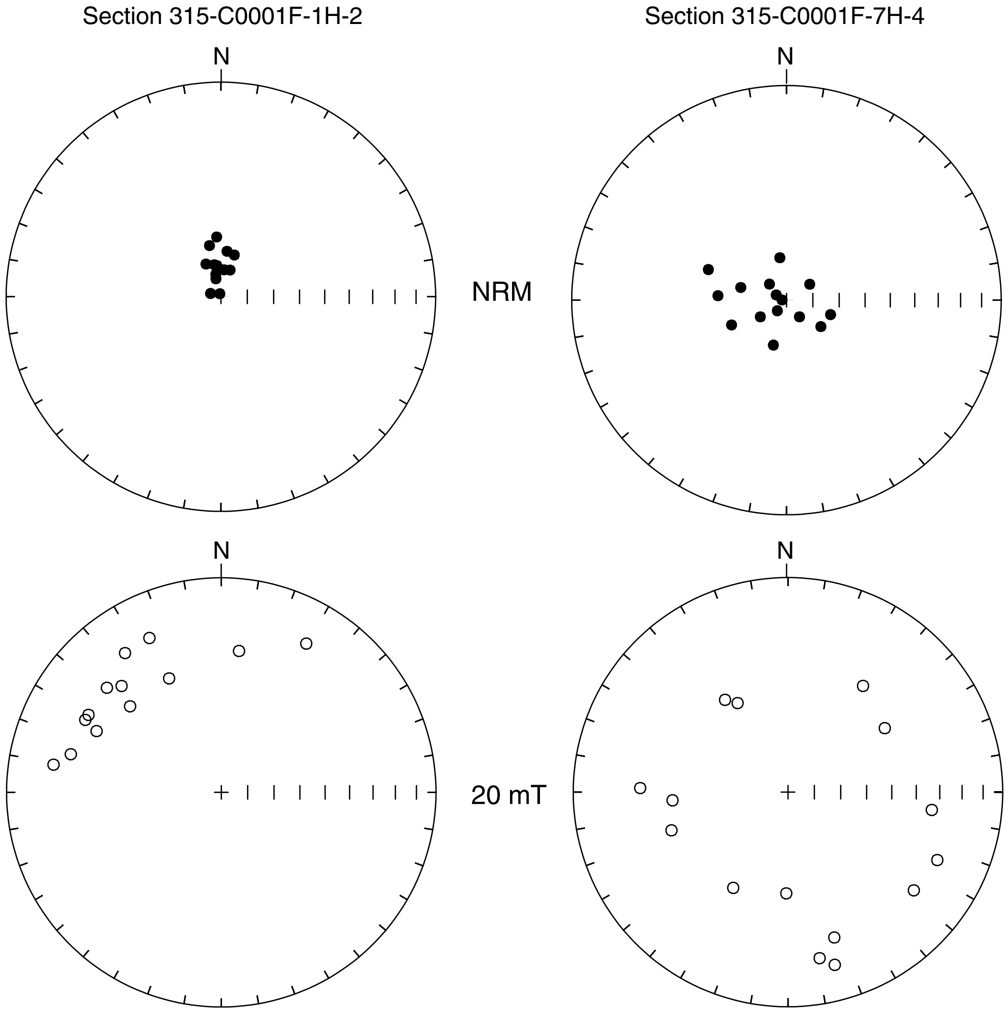

Figure F30. Remanence inclination after 20 mT AF demagnetization, 0–120 m core depth below seafloor (CSF) (Hole C0001E and upper part of Hole C0001F). Black = normal polarity, white = reversed polarity.

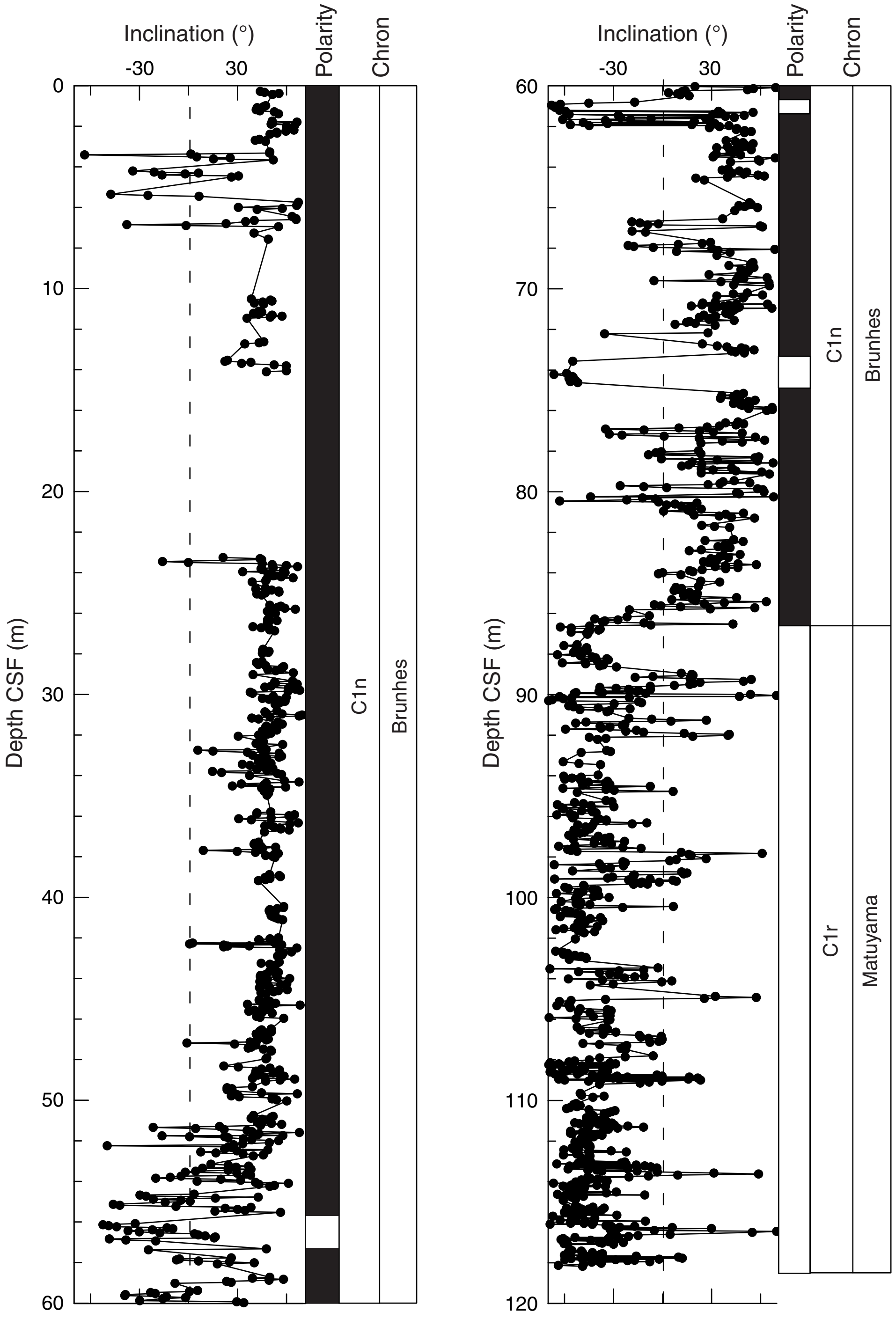

Figure F31. Remanence inclination after 20 mT AF demagnetization, 120–230 m core depth below seafloor (CSF) (Hole C0001F). Black = normal polarity, white = reversed polarity.

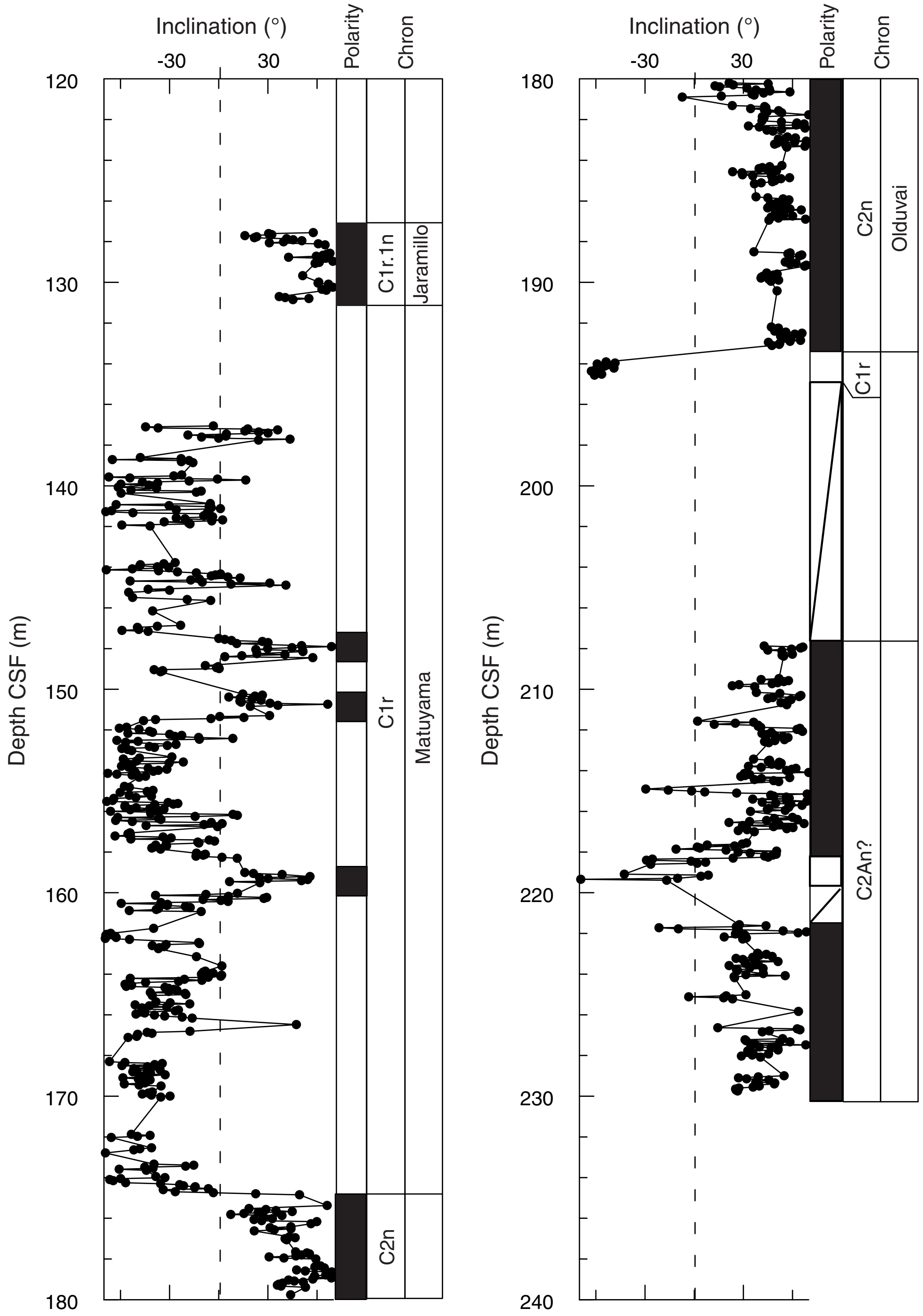

Figure F32. Progressive AF demagnetization displayed by vector end-point diagram (Zijderveld, 1967), lower hemisphere equal area projection, and normalized change in the intensity (Sample 315-C0001H-24R-4, 22–33 cm). Data points = magnetization vector for individual demagnetization steps projected onto horizontal (dots) and vertical (squares) plane. Dashed line = decay curve of vector difference sum. Note that characteristic magnetization direction is defined above 40 mT.

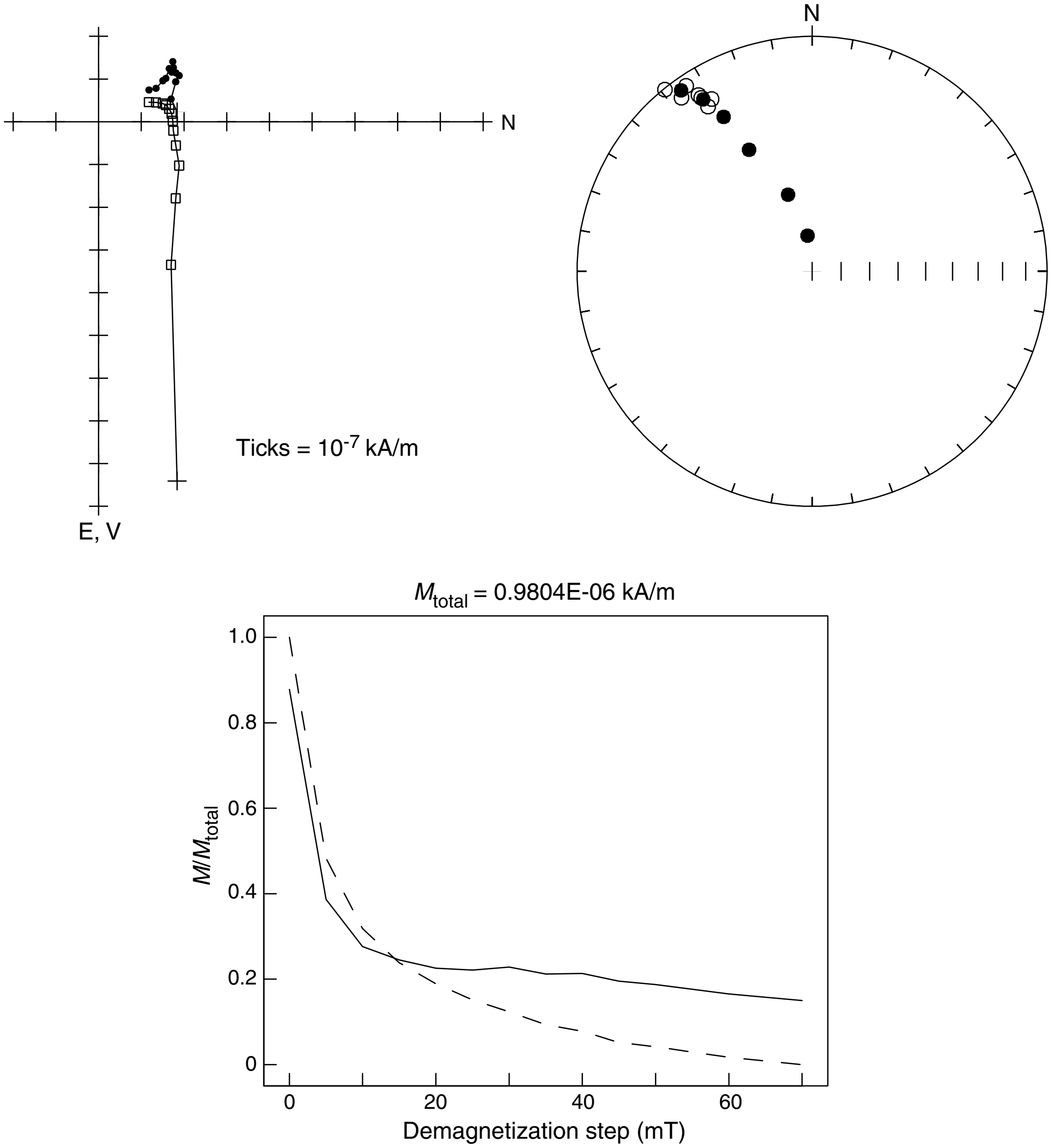

Figure F33. Progressive AF demagnetization displayed by vector end-point diagram (Zijderveld, 1967), lower hemisphere equal area projection, and normalized change in the intensity (Sample 315-C0001H-24R-1, 80–82 cm). Data points = magnetization vector for individual demagnetization steps projected onto horizontal (dots) and vertical (squares) plane. Dashed line = decay curve of vector difference sum. Note that characteristic magnetization direction is not yet defined at a maximum field of 20 mT. Demagnetization trend on stereonet projection shows a great circle with an approximately north-northeast–south-southwest orientation, dipping to the west-northwest. Progression of end vectors suggests a higher coercivity component with negative inclination.

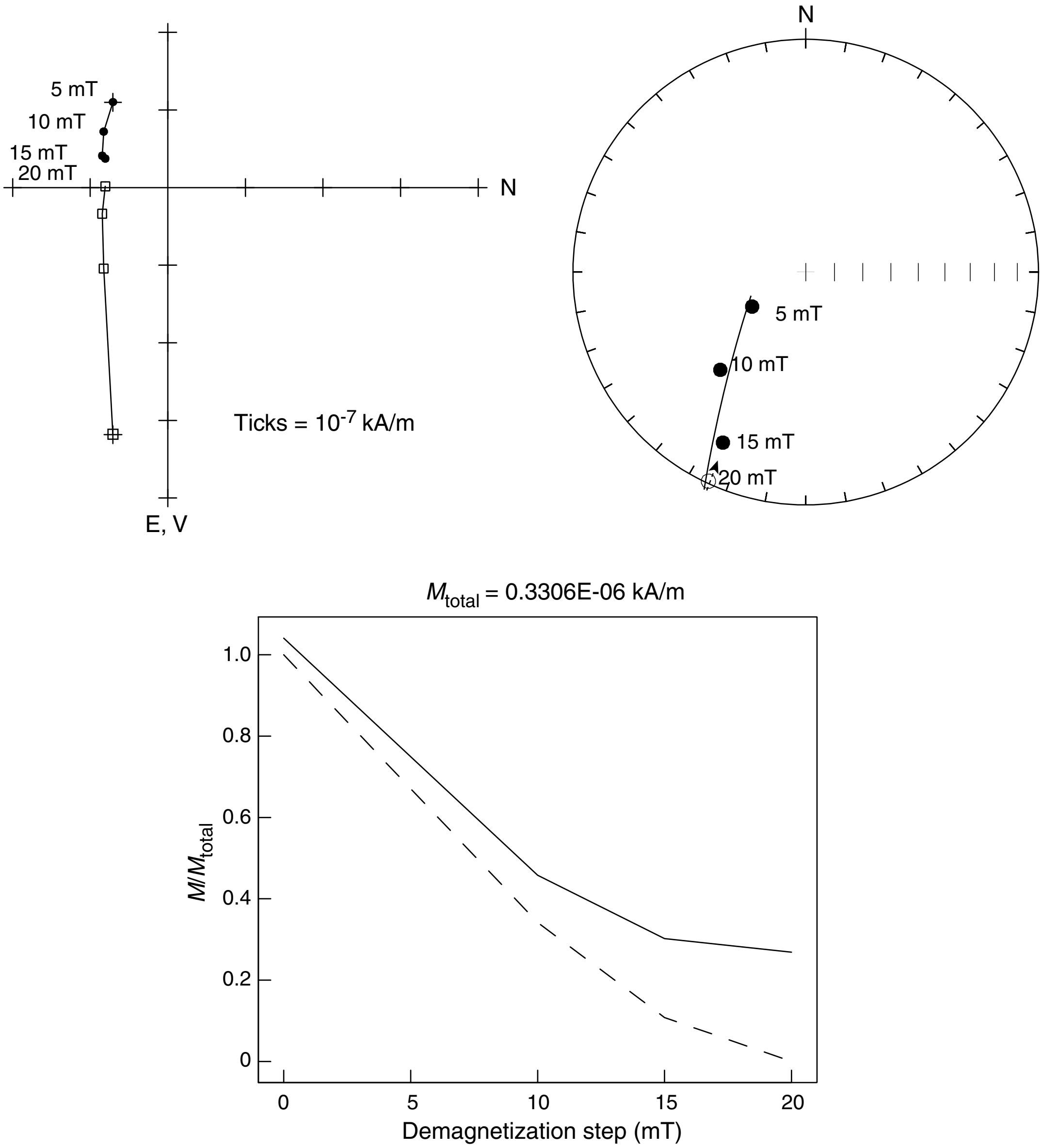

Figure F34. Progressive AF demagnetization displayed by vector end-point diagram (Zijderveld, 1967), lower hemisphere equal area projection, and normalized change in the intensity (Sample 315-C0001H-25R-2, 35–37 cm). Data points = magnetization vector for individual demagnetization steps projected onto horizontal (dots) and vertical (squares) plane. Dashed line = decay curve of vector difference sum. Note that most of the remanence has a very steep downward inclination, suggestive of drilling overprint.

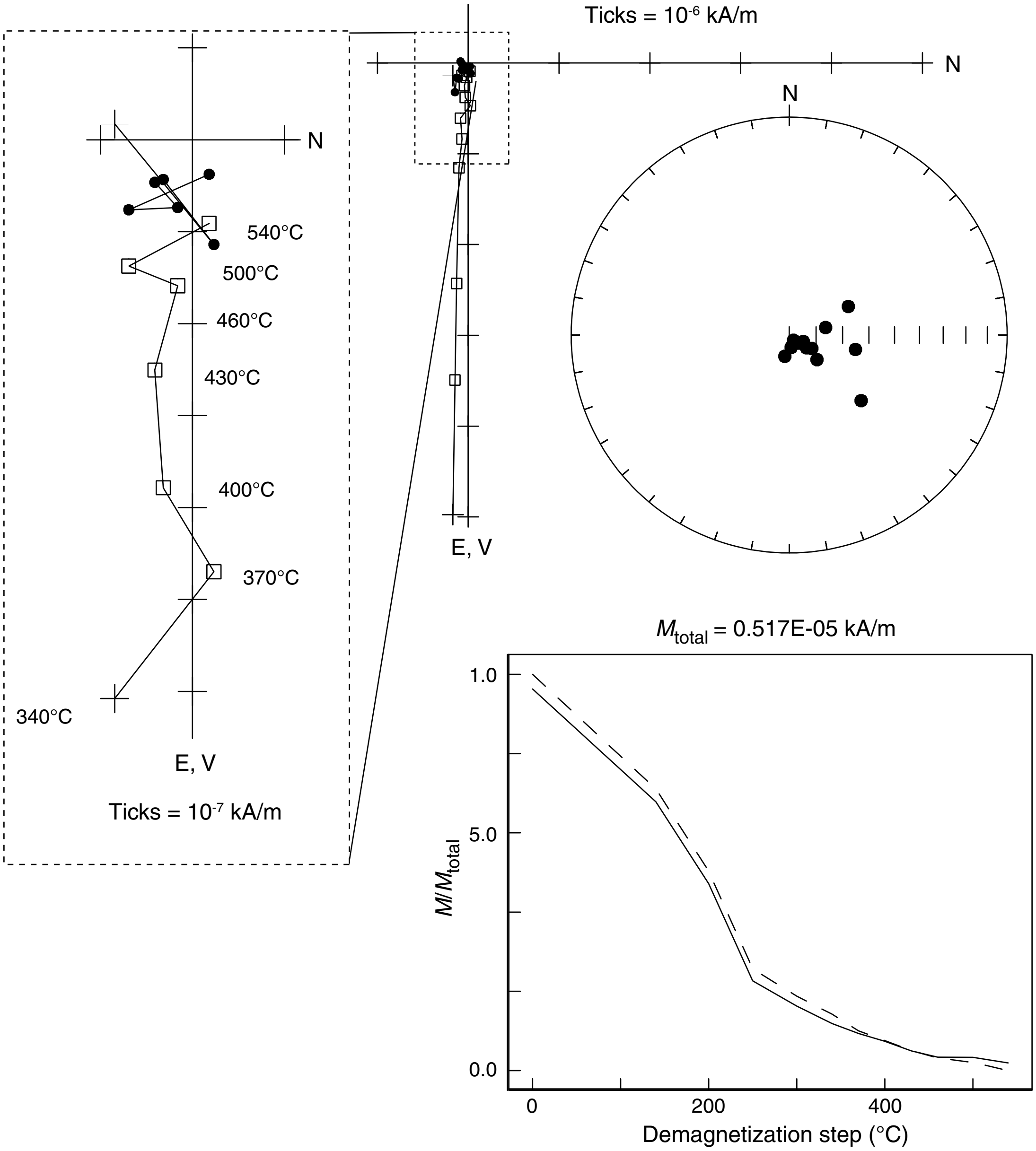

Figure F35. Remanence inclination after 20 mT AF demagnetization, 240–450 m core depth below seafloor (CSF) (Hole C0001H). Black = normal polarity, white = reversed polarity, crossed out areas = no data (see text for discussion).

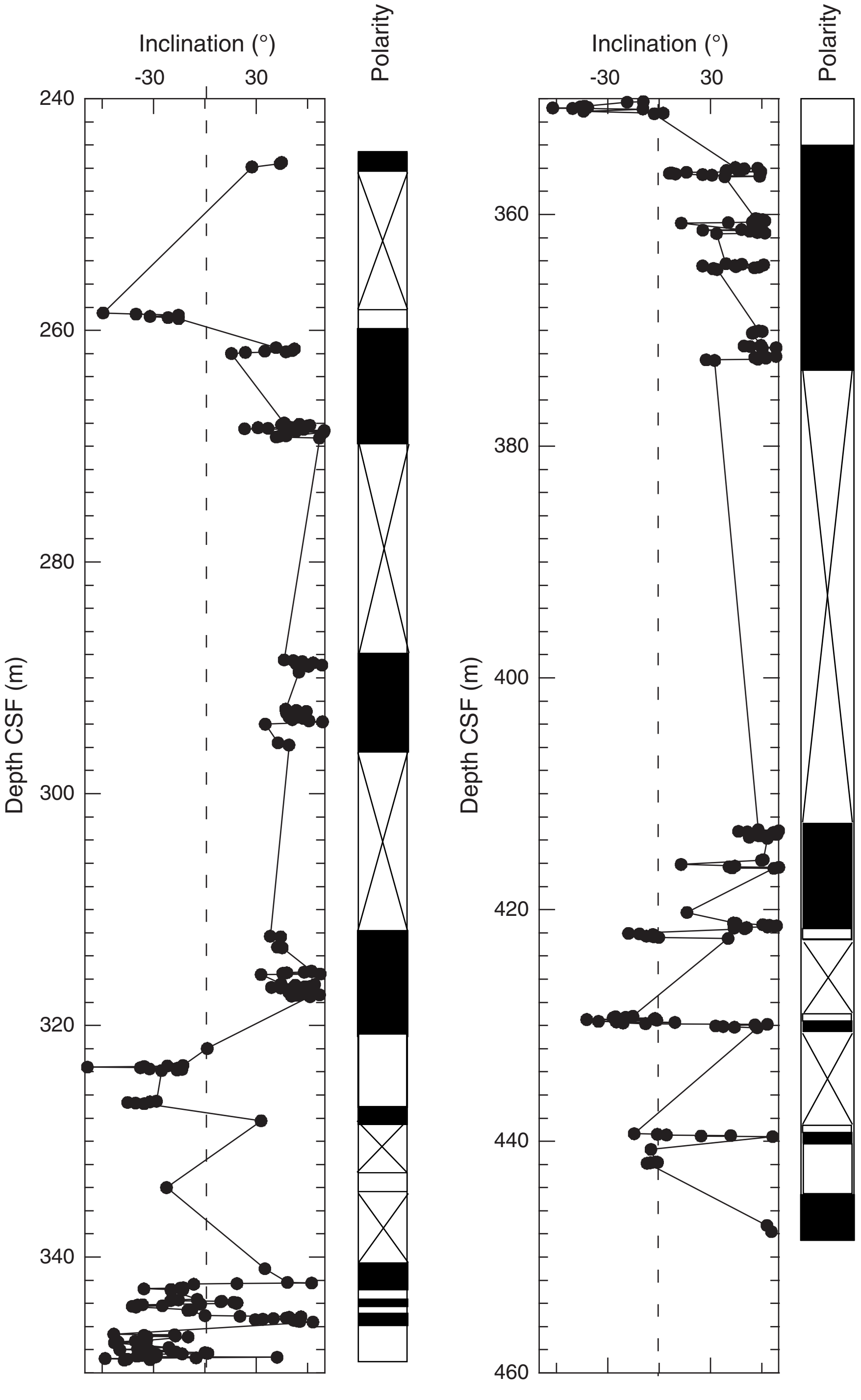

Figure F36. Age-depth curve based on magnetostratigraphic interpretation, Site C0001. Dashed lines = tentative interpretation based on biostratigraphic results. CSF = core depth below seafloor.

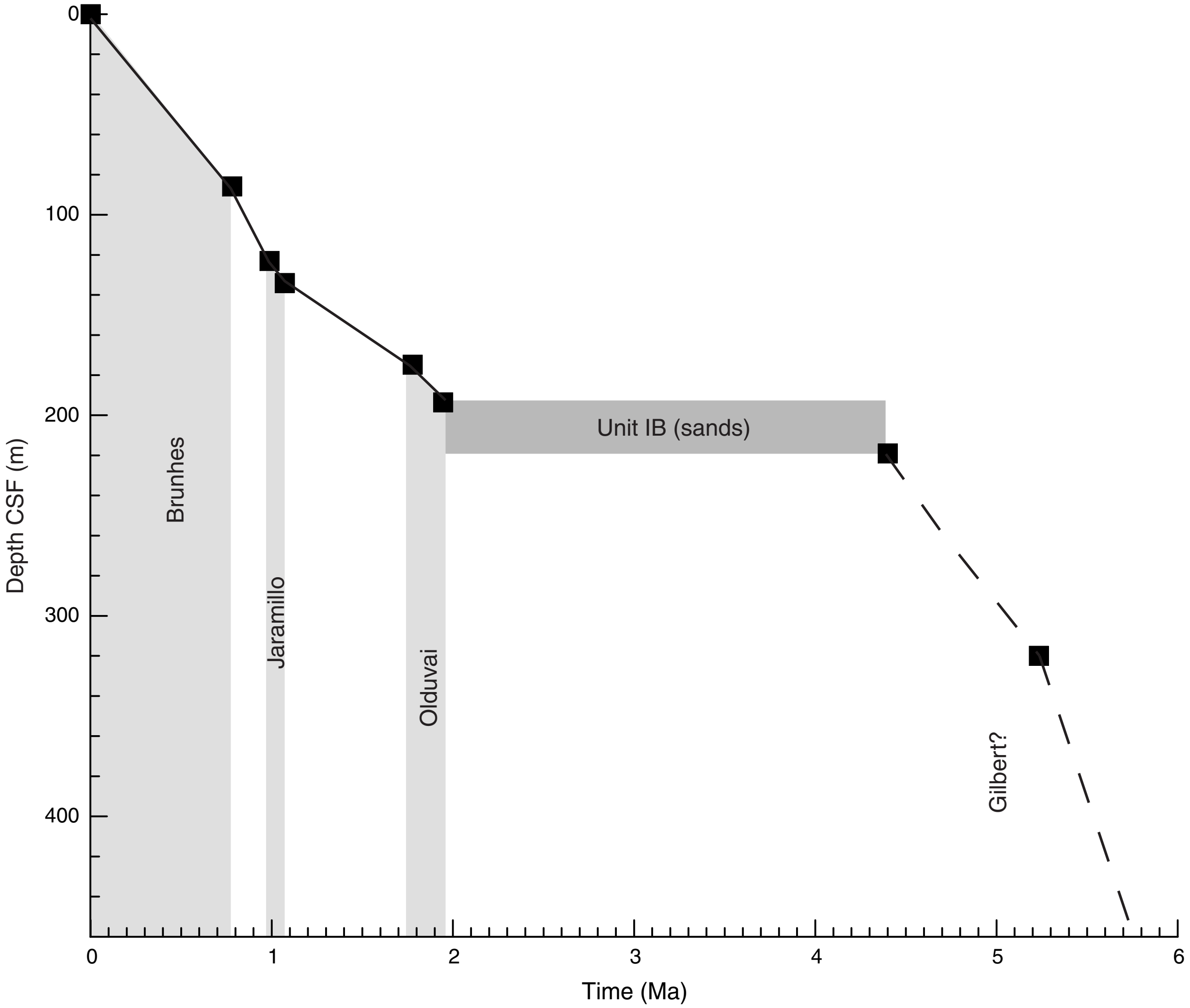

Figure F37. Concentrations of sulfate, phosphate and ammonium, major halogens (Cl and Br), and pH, alkalinity, and salinity in interstitial waters, Site C0001. Salinity is calculated as total dissolved solutes. Stars = standard seawater values. CSF = core depth below seafloor.

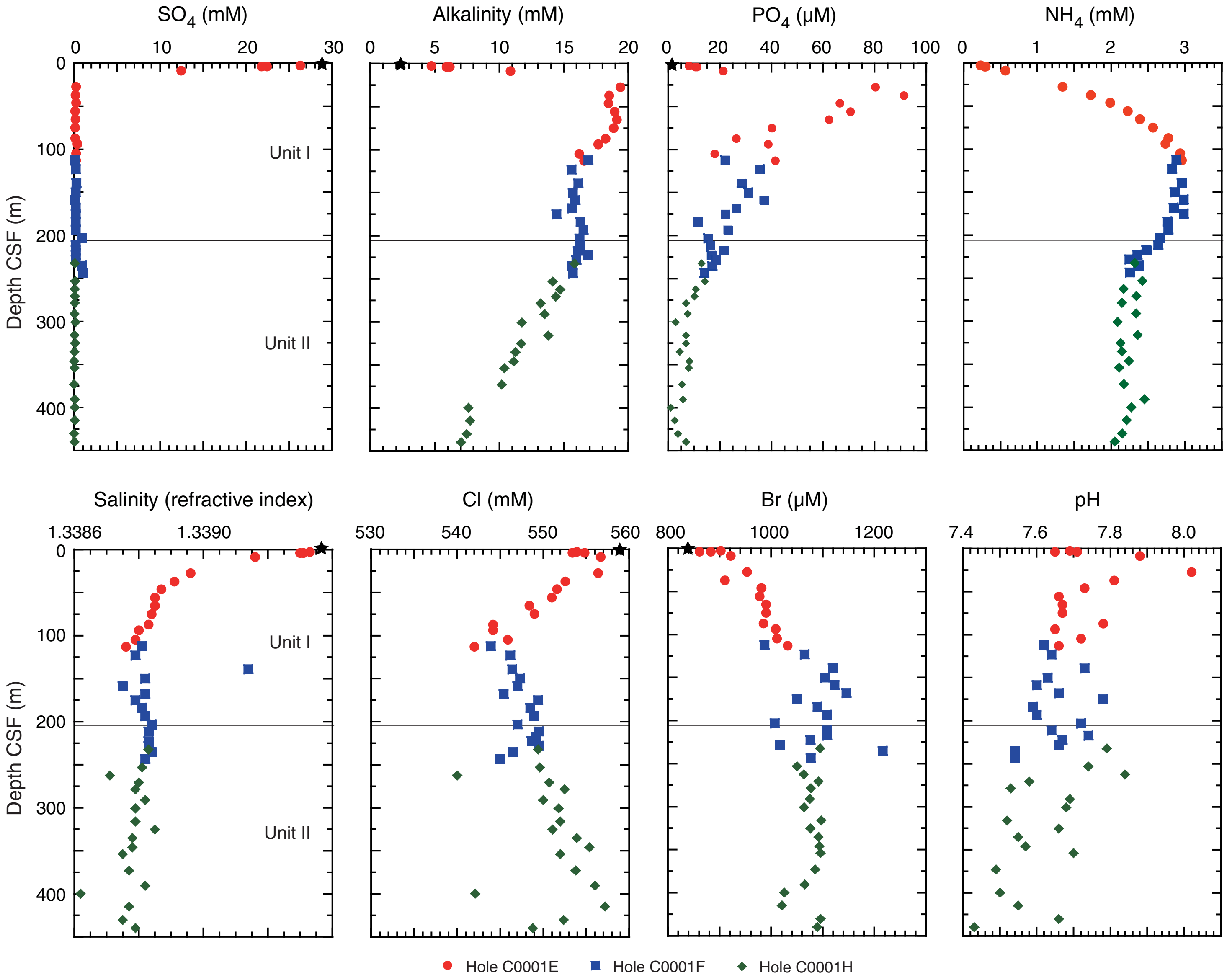

Figure F38. Concentrations of major (Na, K, Ca, and Mg) and minor (Si, B, Li, Mn, and Fe) cations in interstitial waters, Site C0001. Stars = standard seawater values. CSF = core depth below seafloor.

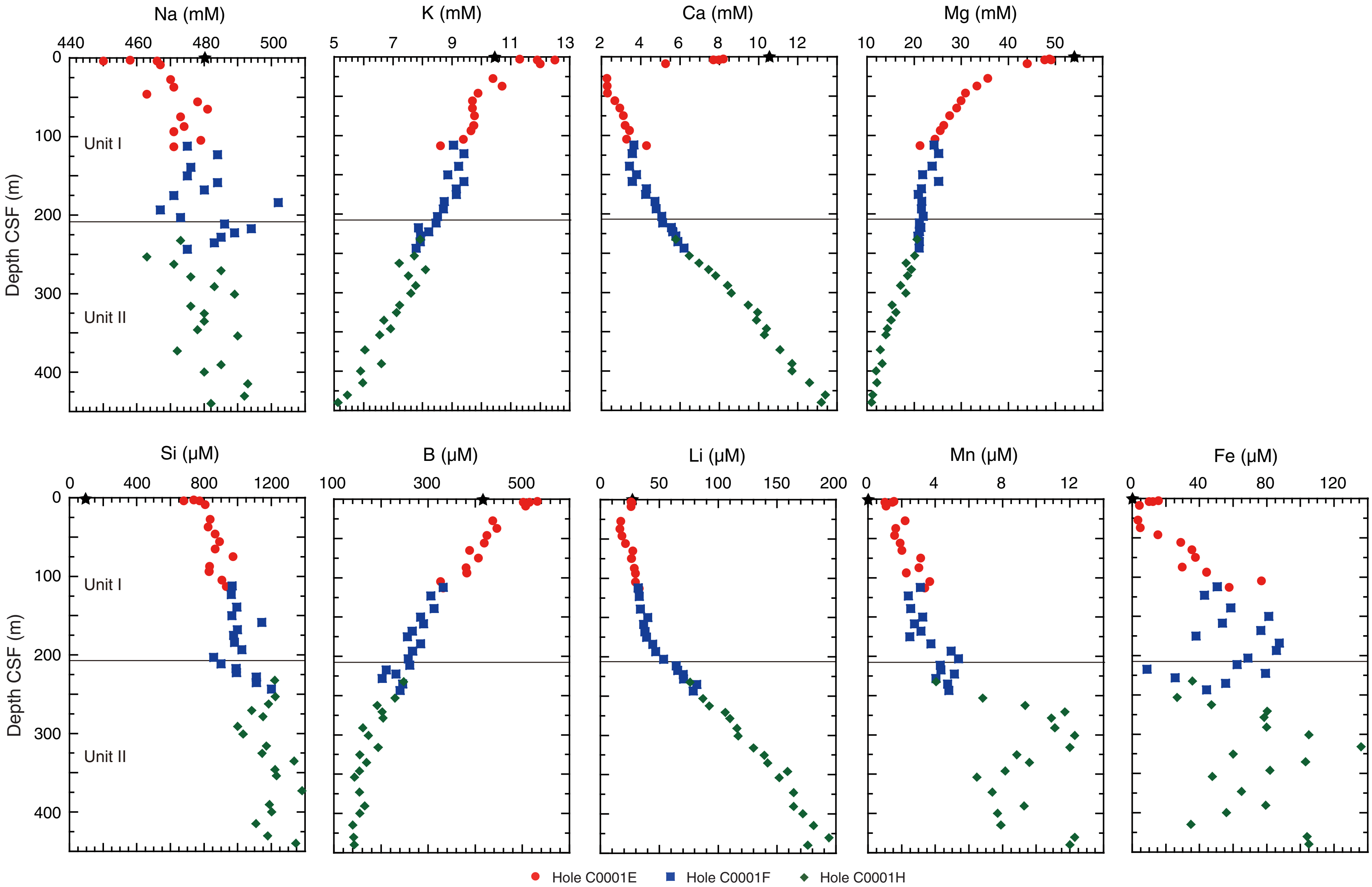

Figure F39. Concentrations of minor cations (Sr and Ba) and trace elements (Mo, V, Zn, Cu, Rb, Cs, Pb, and U), Site C0001. Stars = standard seawater values. CSF = core depth below seafloor.

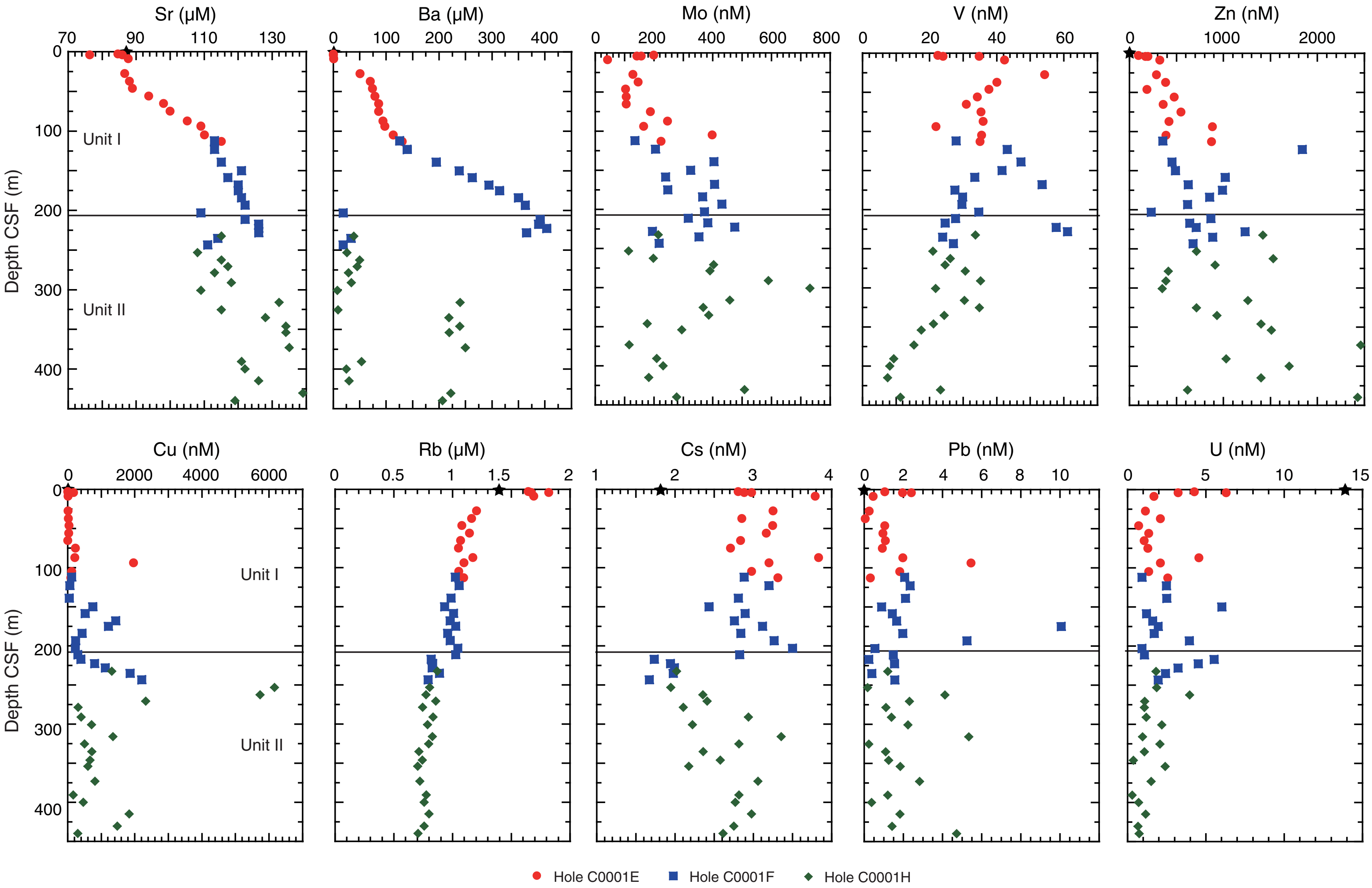

Figure F40. Concentration of Y and oxygen and hydrogen isotopic composition of interstitial water, Site C0001. Stars = standard seawater value. VSMOW = Vienna standard mean ocean water. CSF = core depth below seafloor.

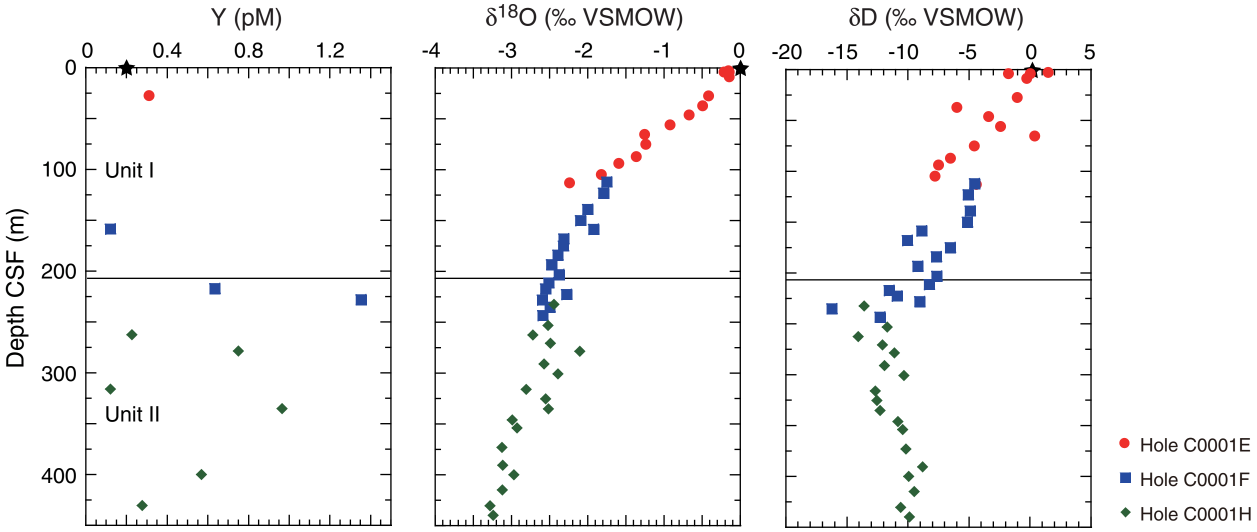

Figure F41. Methane and ethane concentrations in headspace samples, Site C0001. CSF = core depth below seafloor.

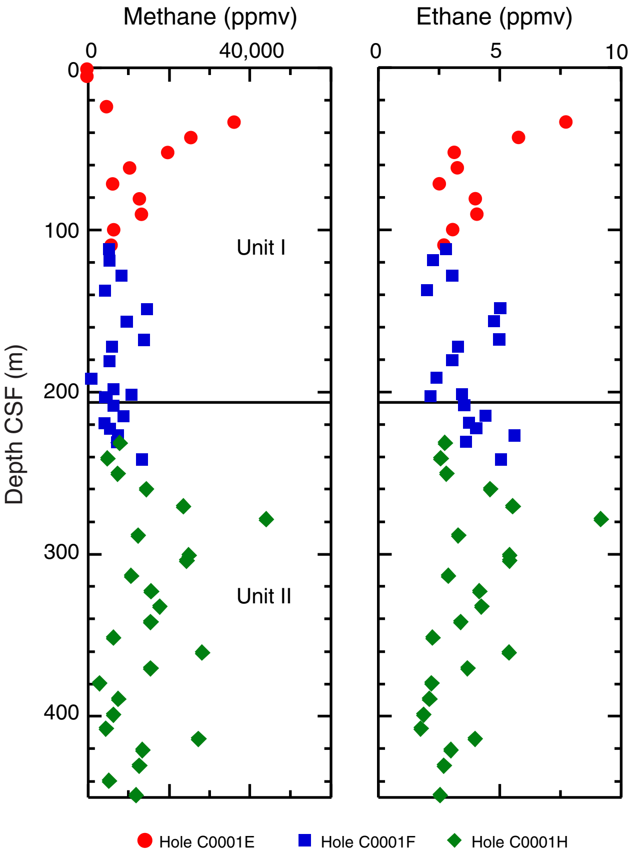

Figure F42. Methane and dissolved sulfate concentrations, Site C0001. CSF = core depth below seafloor.

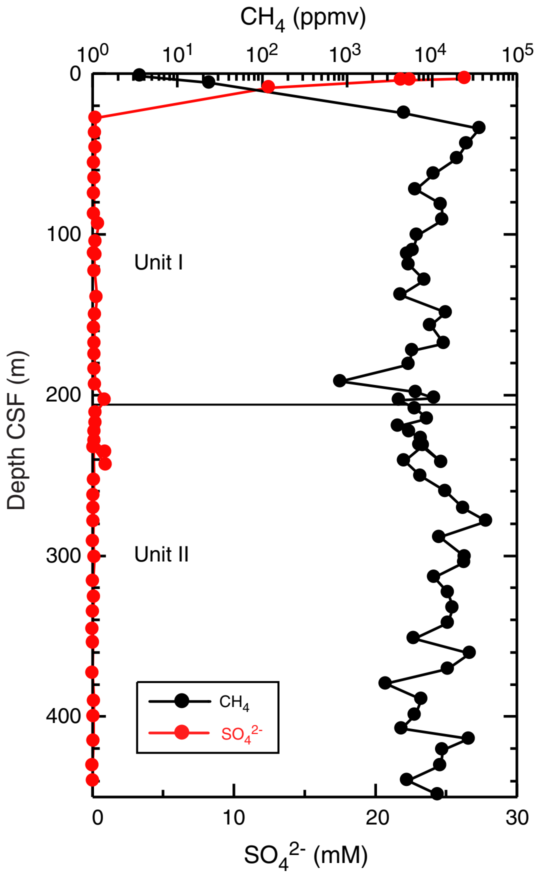

Figure F43. Methane to ethane ratio, Site C0001. CSF = core depth below seafloor.

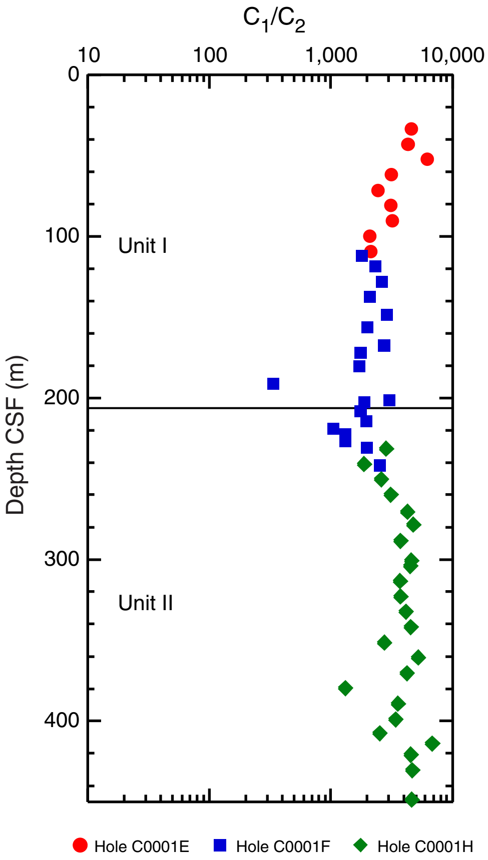

Figure F44. Inorganic carbon (IC), calcium carbonate ($CaCO_3$), total organic carbon (TOC), total nitrogen (TN), carbon to nitrogen (C/N) ratio, and total sulfur (TS) in sediments, Site C0001. CSF = core depth below seafloor.

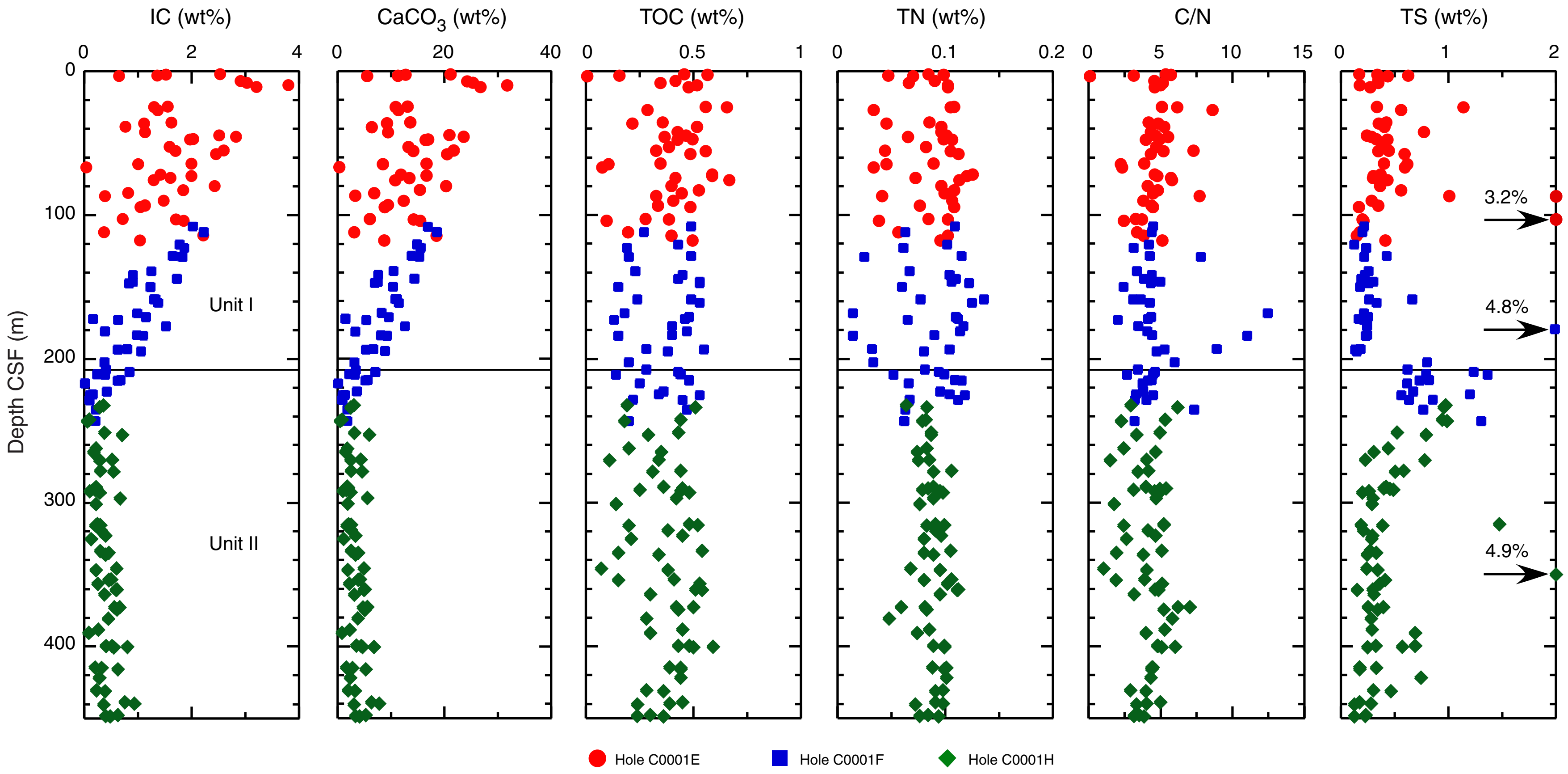

Figure F45. Epifluorescence image of SYBR Green I stained sample of fixed cells (Section 315-C0001H-25R-1) (448 m core depth below seafloor).

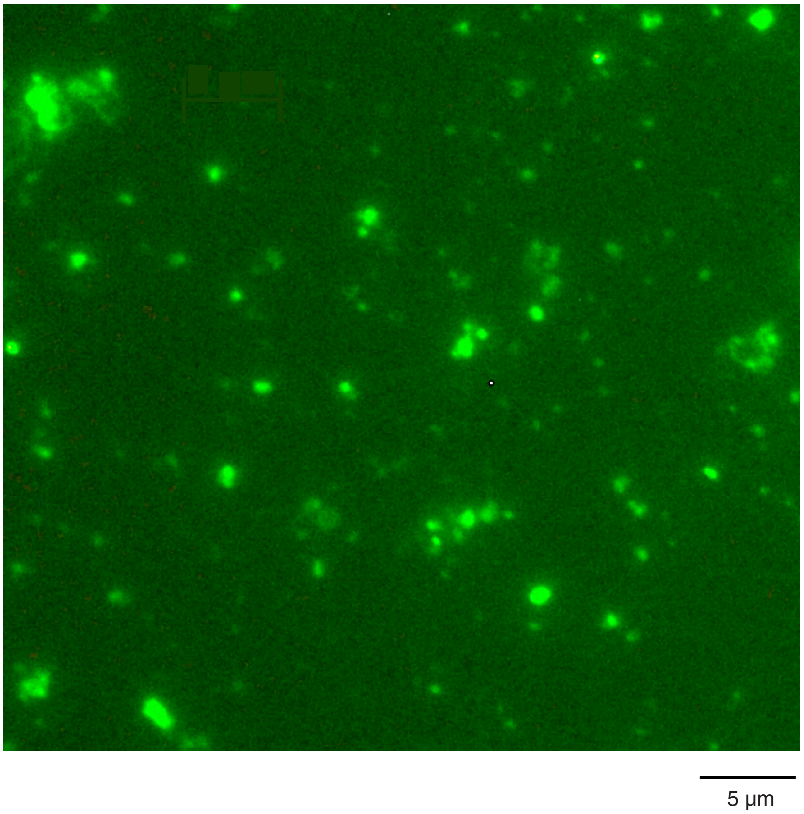

Figure F46. Physical property measurements, Site C0001. **A.** Moisture and density (MAD) and multisensor core logger (MSCL) for whole-round core sections (MSCL-W) porosity. **B.** MAD and MSCL-W bulk density. **C.** MAD grain density. CSF = core depth below seafloor.

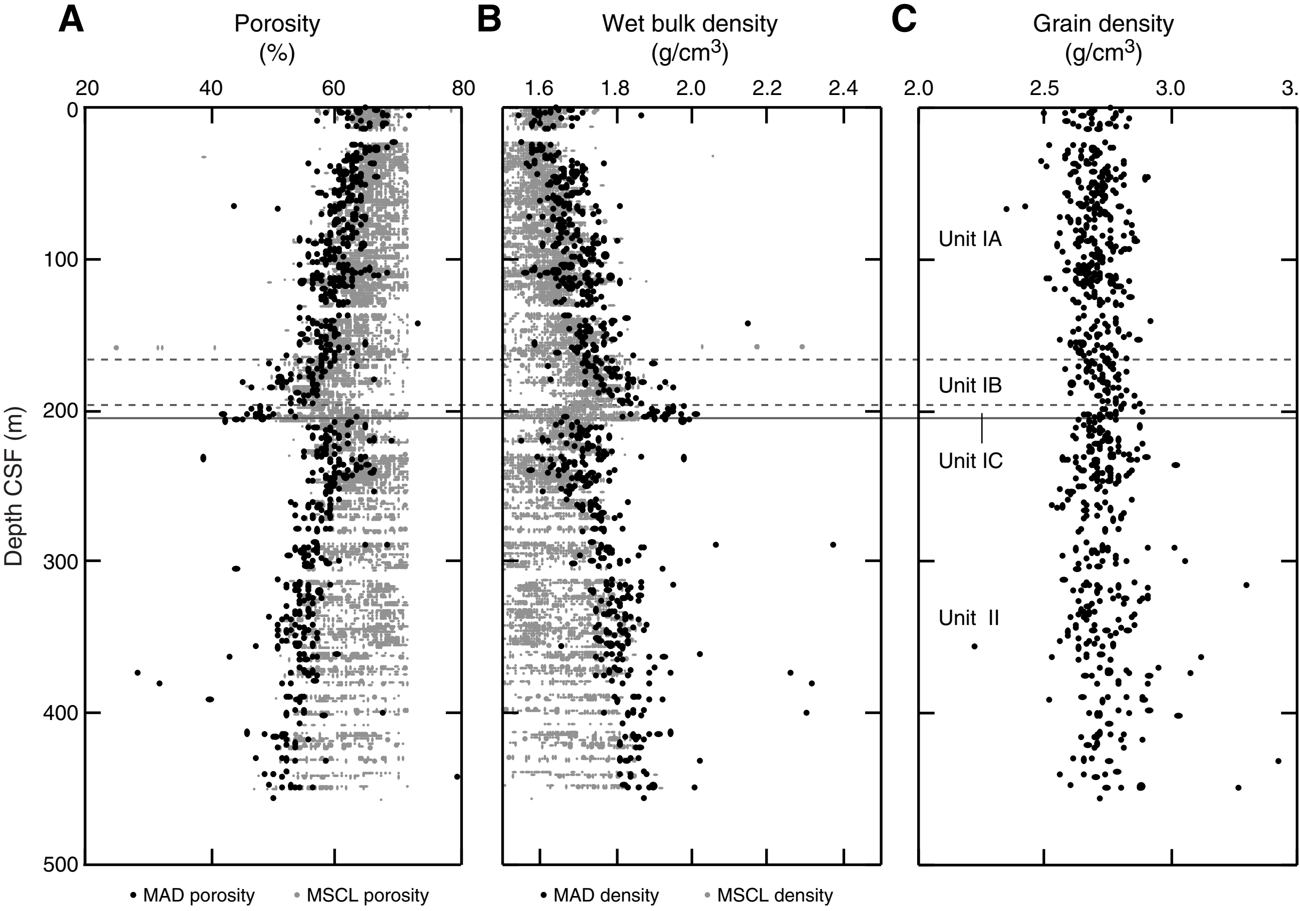

Figure F47. Physical property measurements, Site C0001. **A.** Undrained shear strength measured using a miniature vane shear and pocket penetrometer. Circle = data obtained for disturbed ESCS cores. **B.** Porosity profile. **C.** Thermal conductivity. CSF = core depth below seafloor.

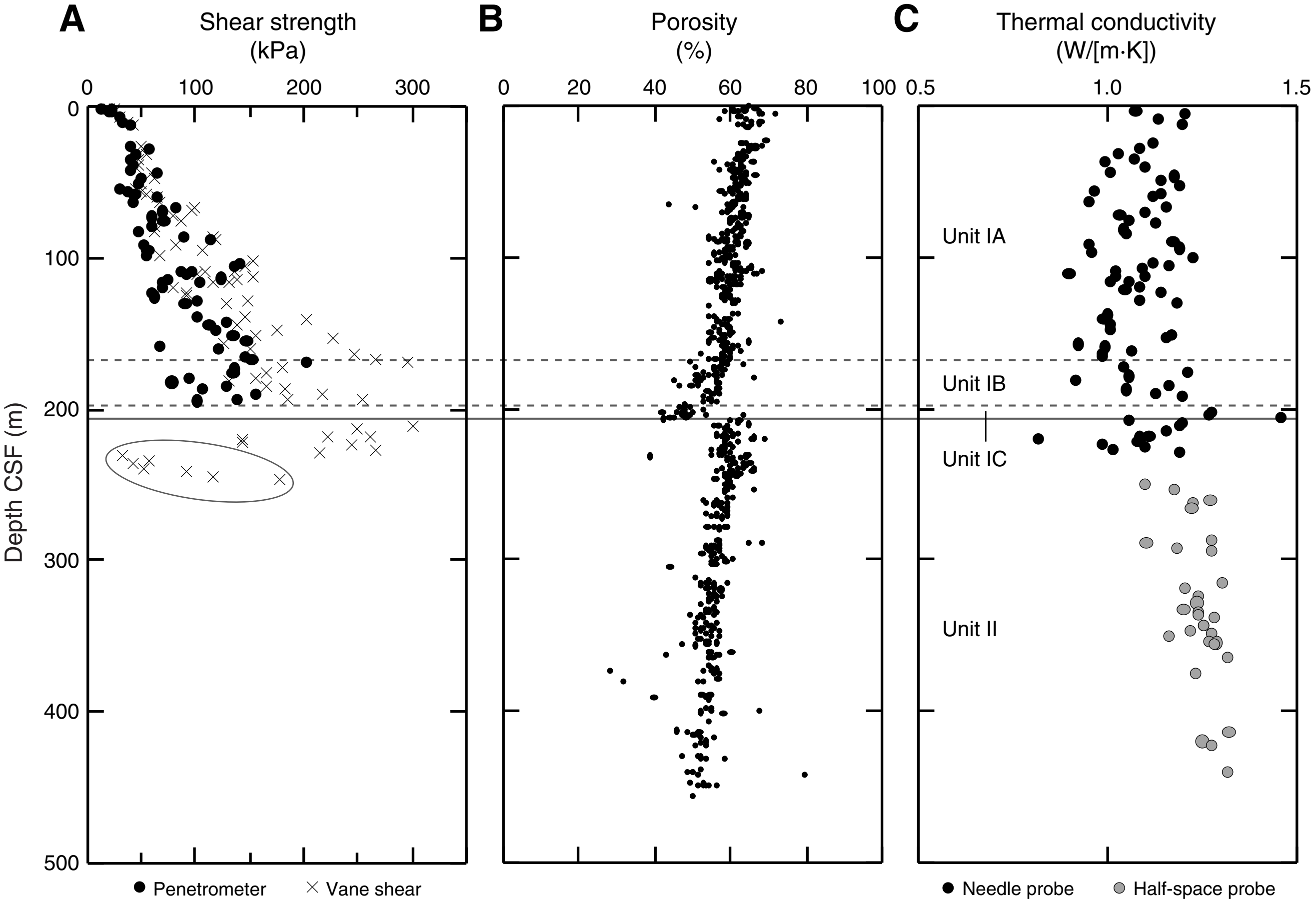

Figure F48. L*, a*, and b* values, Site C0001. CSF = core depth below seafloor.

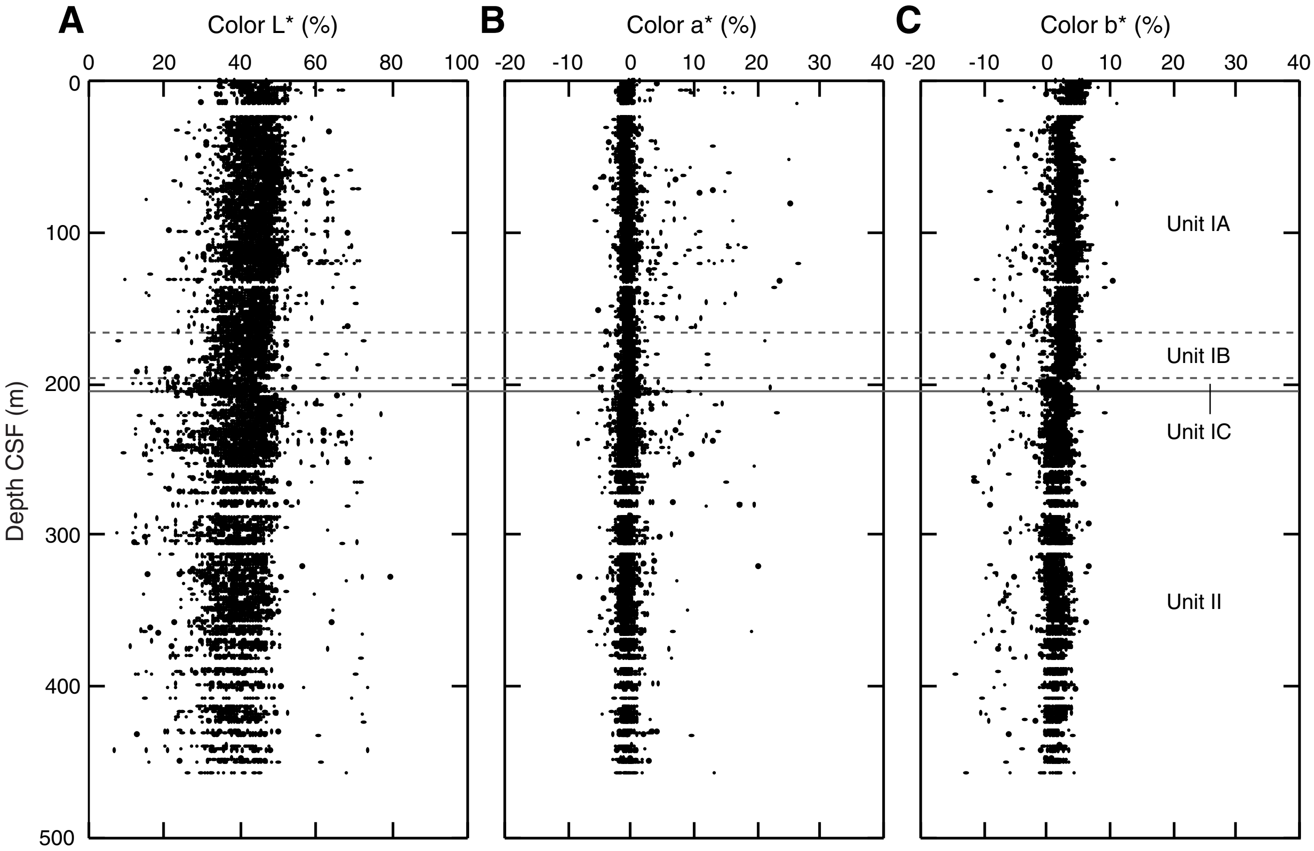

Figure F49. Downhole temperature, Site C0001. **A.** Gradient fit. **B.** Heat flow determination and temperature extrapolation based on measured thermal conductivities. CSF = core depth below seafloor.

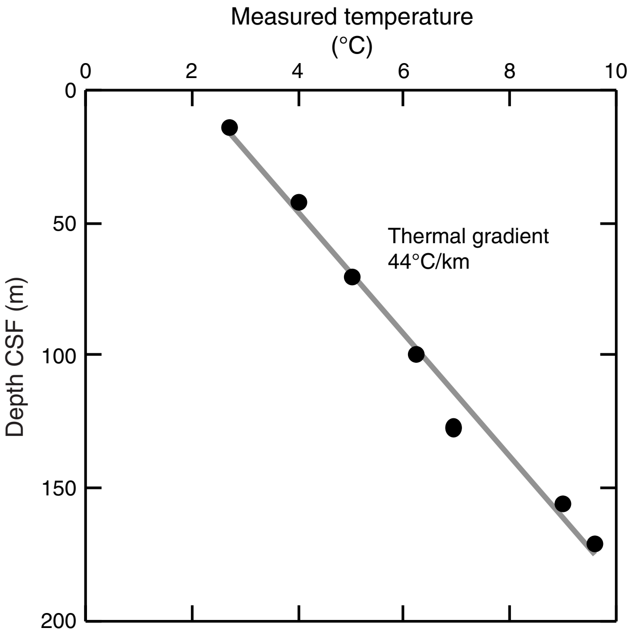

Figure F50. Downhole temperature, Site C0001. Gradient fit of measurements = 43°C/km. Heat flow determination and temperature extrapolation based on downhole temperature measurements. CSF = core depth below seafloor.

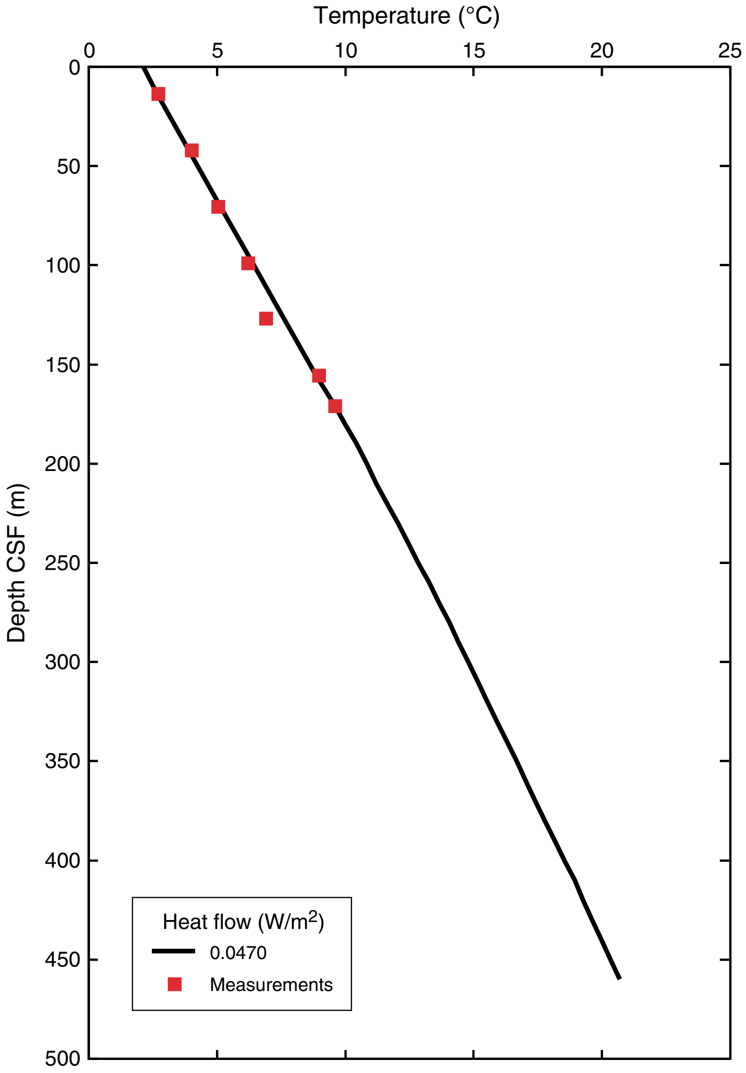

Figure F51. Electrical conductivity and *P*-wave velocity measurements on discrete samples in orthogonal directions (*x*, *y*, and *z*). CSF = core depth below seafloor.

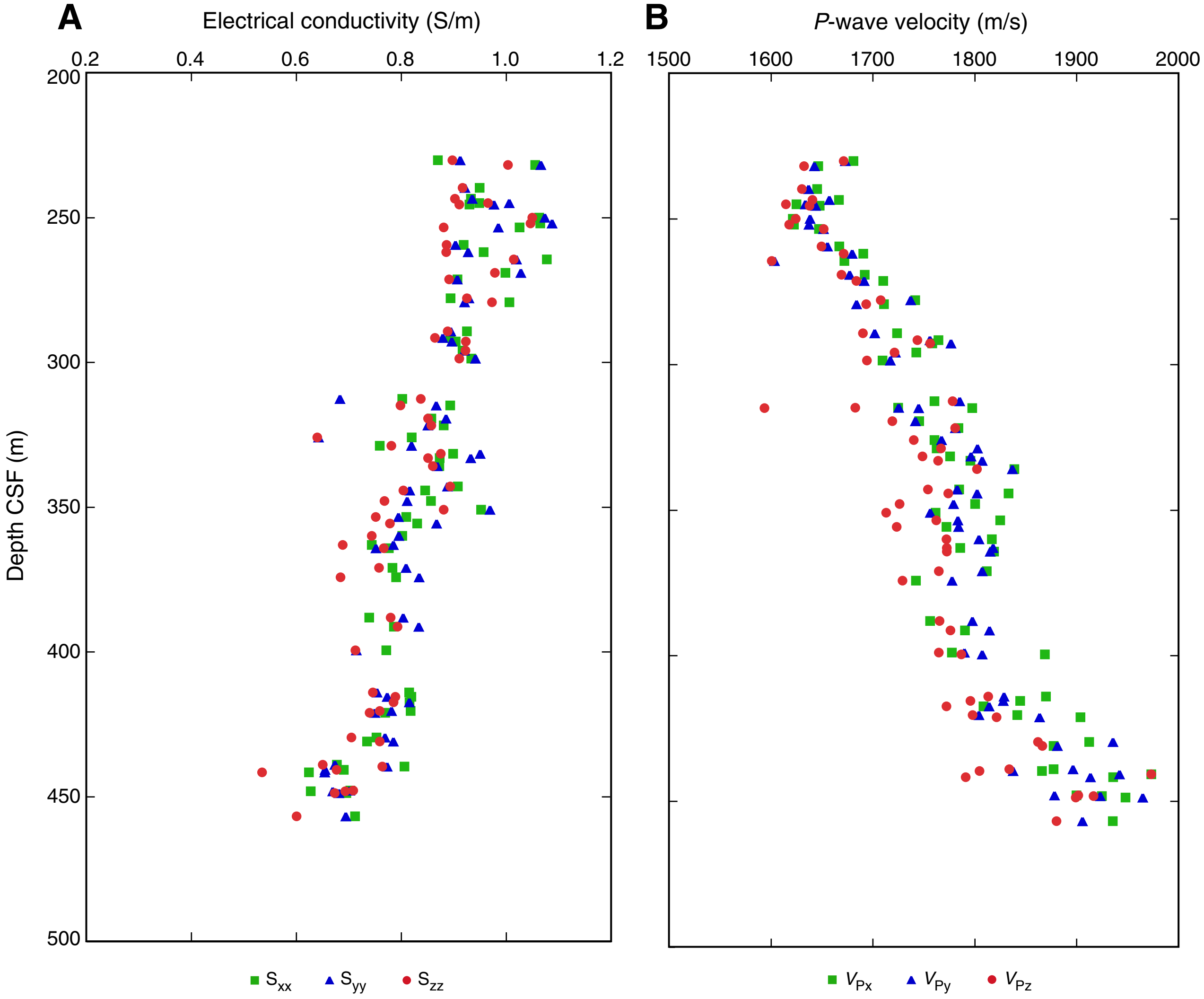

Figure F52. Magnetic susceptibility from MSCL-W, Site C0001. **A.** Data from Hole C0001E shifted to corresponding depth in Hole C0001B. Hole C0001B data are shifted by 0.1 magnetic susceptibility unit. **B.** Holes C0001E and C0001F. Data from Hole C0001F are shifted by 0.1 magnetic susceptibility unit. **C.** Holes C0001F and C0001H. CSF-B = core depth below seafloor, IODP Method B (see the **"Expedition 315 Methods"** chapter).

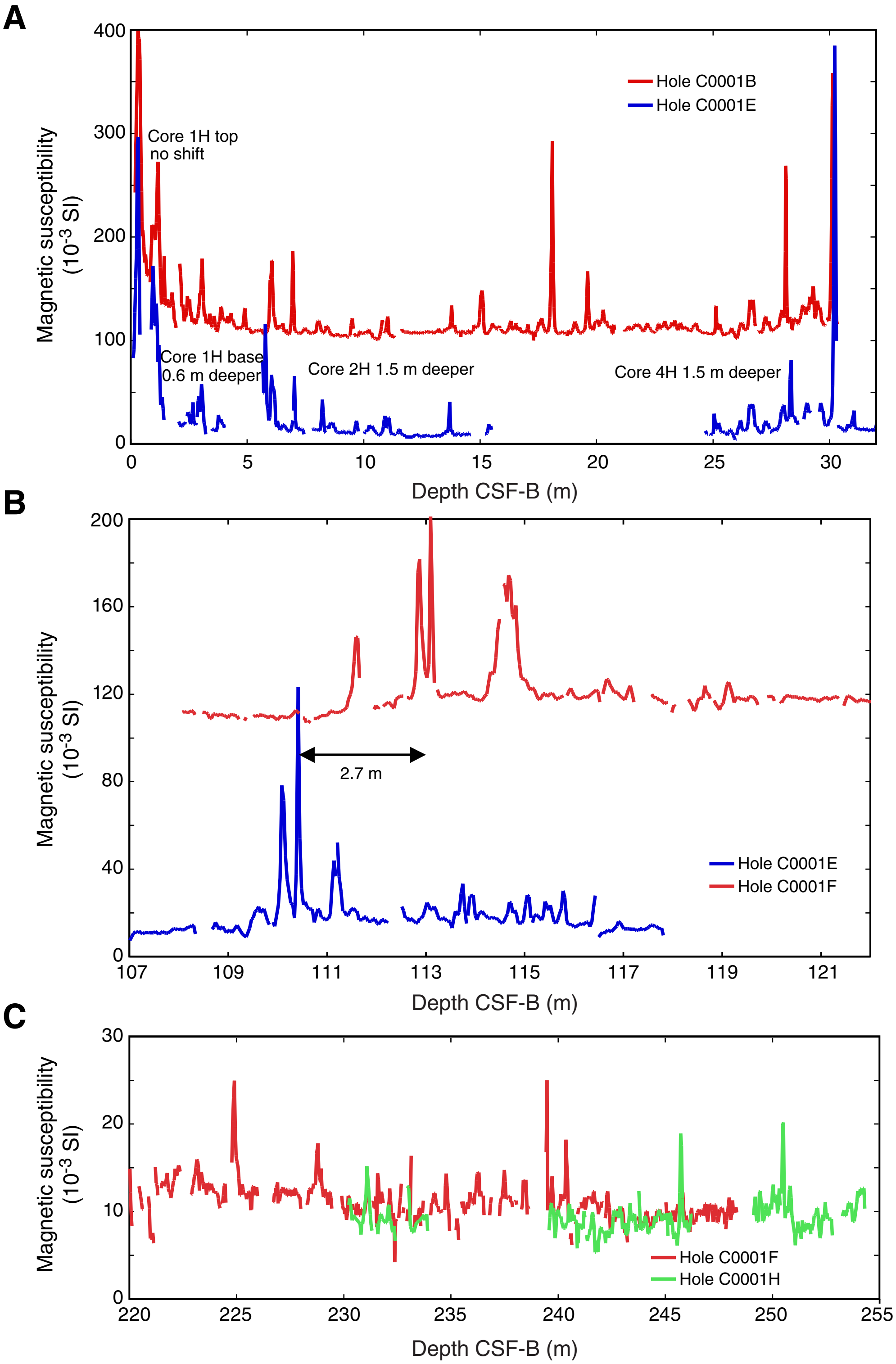

Figure F53. Gamma ray (GR) density from multisensor core log (MSCL) measurements on whole-round cores (MSCL-W) and archive and from logging-while-drilling (LWD) GR data, Site C0001. MSCL natural gamma ray (NGR) units = counts per seconds, LWD units = gAPI units. **A.** Holes C0001D, C0001E, and C0001F plotted as a function of depth. **B.** Holes C0001D, C0001E, and C0001F plotted as a function of corresponding depth in LWD hole. **C.** Holes C0001D and C0001H plotted as a function of corresponding depth in LWD hole. CSF = core depth below seafloor, LSF = LWD depth below seafloor.

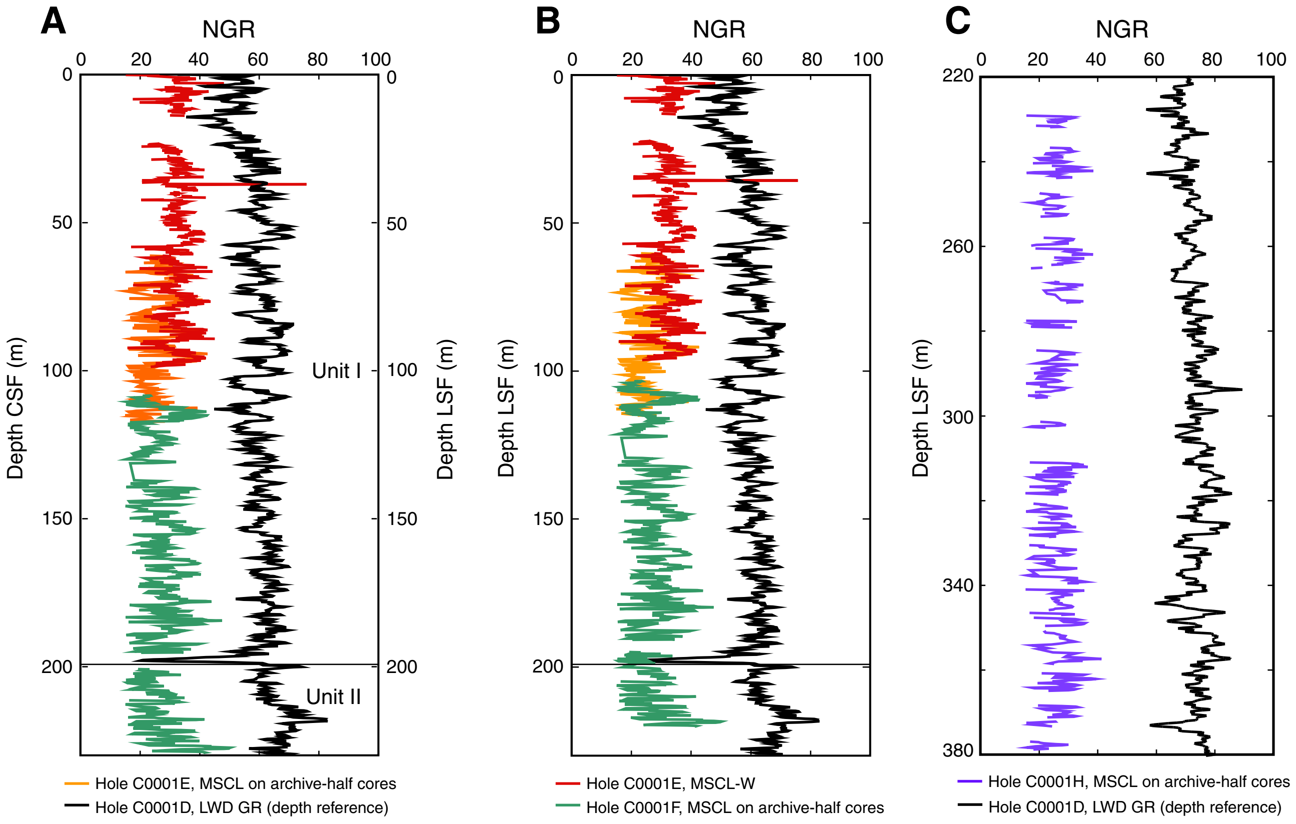

Figure F54. Resistivity measured on samples in the horizontal plane and corrected for in situ temperature compared with logging-while-drilling (LWD) ring resistivity, Holes C0001D and C0001H. CSF = core depth below seafloor, LSF = LWD depth below seafloor.

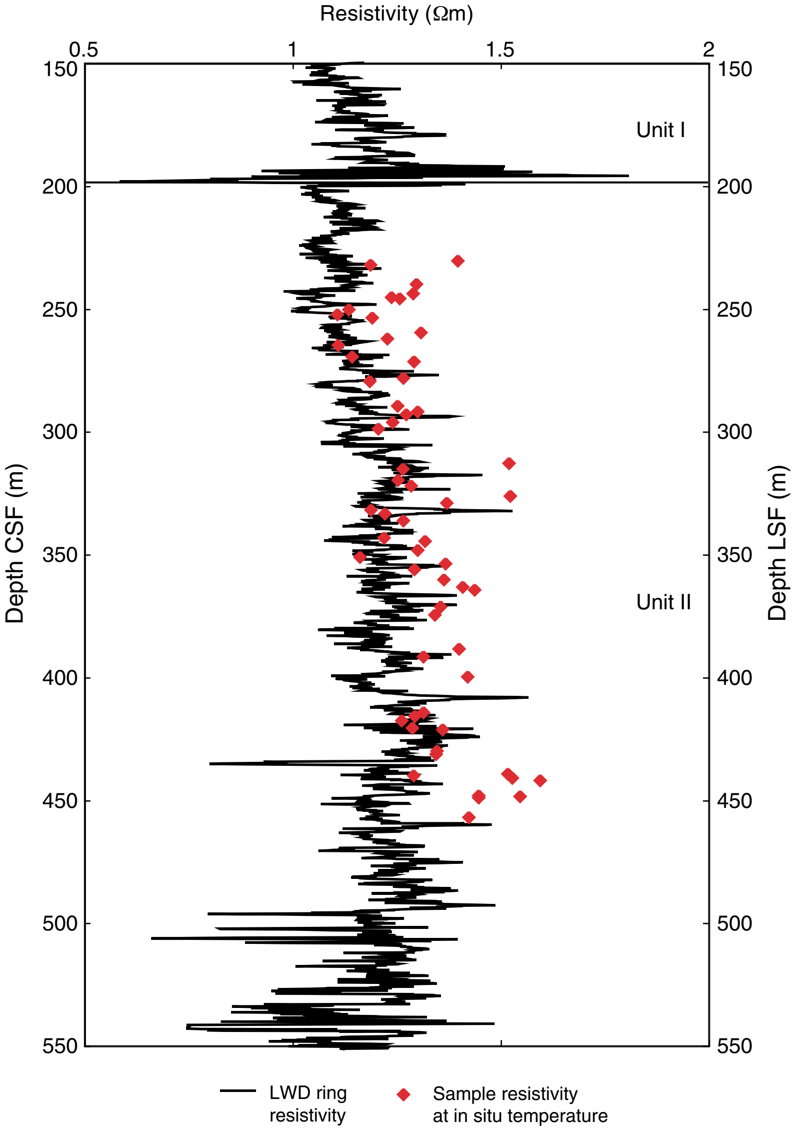

Figure F55. *P*-wave velocity in vertical direction (V_{Pz}) from logging-while-drilling (LWD) in Hole C0001D and from discrete samples from Hole C0001H. Values in blue were measured in the laboratory. CSF = core depth below seafloor, LSF = LWD depth below seafloor.

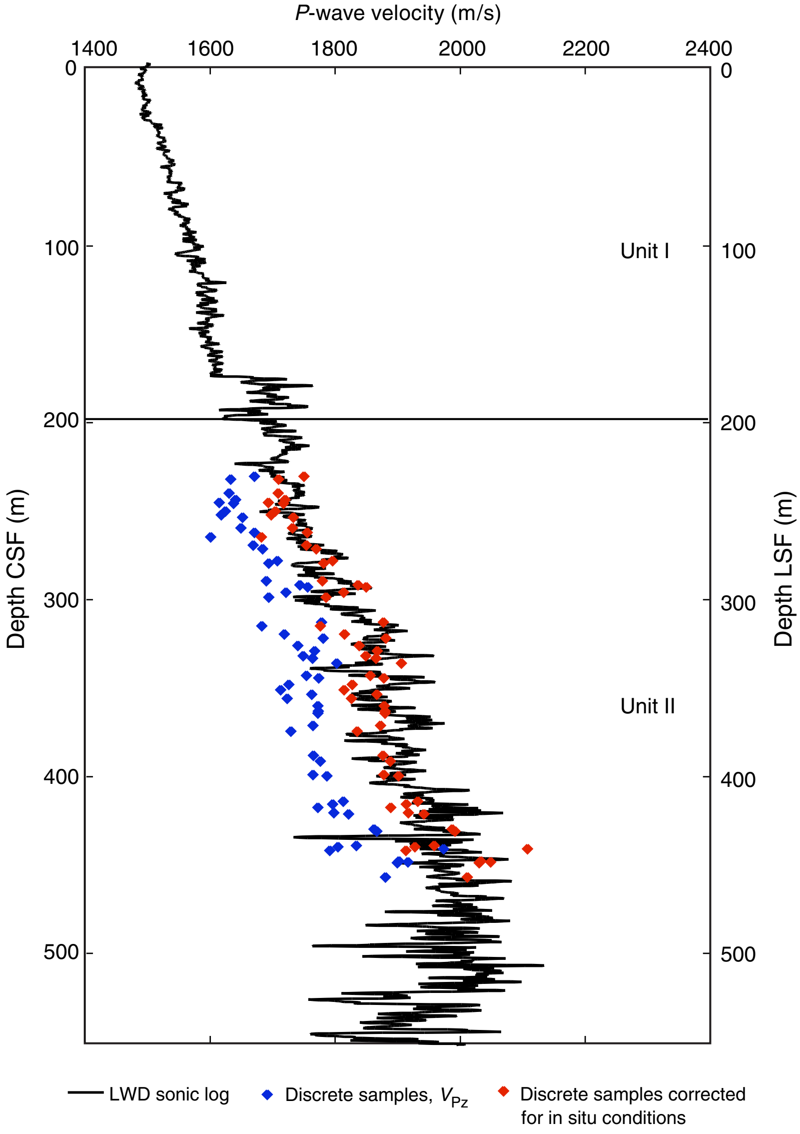

Movie M1. QuickTime movie of X-ray CT image along axis of core to bottom. Note sediment structure shows clockwise rotation.

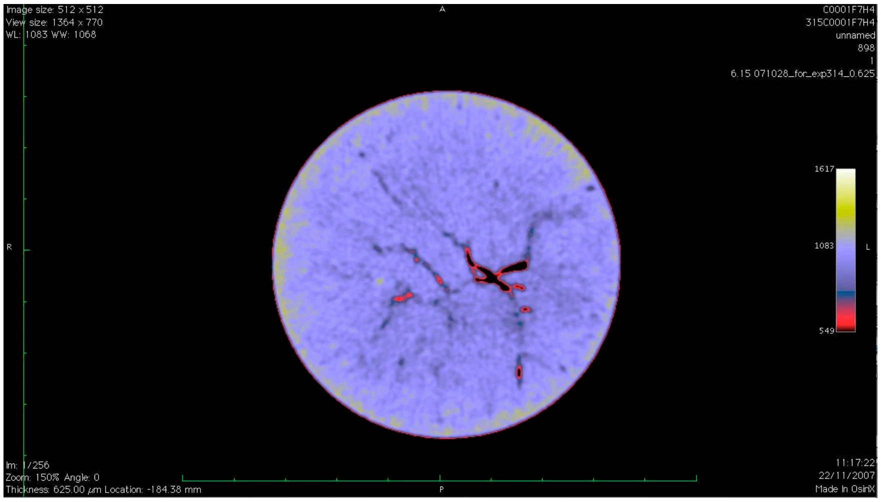

Table T1. Coring summary, Hole C0001E. (See table notes.)

Hole C0001E
Latitude: 33°14.3442′N
Longitude: 136°42.6924′E
Time on hole (h): 104.5 (0000 h, 17 Nov 2007–0830 h, 21 Nov 2007)
Seafloor (drillers measurement from rig floor, m): 2226.5
Distance between rig floor and sea level (m): 28.5
Water depth (drillers measurement from sea level, m): 2198
Total depth (drillers depth below rig floor, m): 2344.6
Total penetration (core depth below seafloor, m): 118.1
Total length of cored section (m): 118.1
Total core recovered (m): 112.67
Core recovery (%): 95.4
Total number of cores: 13

Core	Date (Nov 2007)	Local time (h)	Depth CSF (m)		Length (m)		Recovery (%)	Comments
			Top	Bottom	Cored	Recovered		
315-0001E-								
1H	20	0443	0	4.1	4.1	4.1	100.0	
2H	20	0653	4.1	13.6	9.5	9.6	101.1	With APCT3
3H	20	0835	13.6	23.1	9.5	0.7	7.4	
4H	20	1045	23.1	32.6	9.5	9.7	102.2	
5H	20	1303	32.6	42.1	9.5	9.7	102.1	With APCT3
6H	20	1451	42.1	51.6	9.5	9.8	102.7	
7H	20	1700	51.6	61.1	9.5	9.8	103.6	
8H	20	1900	61.1	70.6	9.5	9.8	103.2	Higher pressure is needed to shoot the piston
9H	20	2028	70.6	80.1	9.5	9.9	104.2	Opened valve of HPCS
10H	20	2211	80.1	89.6	9.5	9.9	104.2	
11H	21	0040	89.6	99.1	9.5	9.9	104.2	With APCT3
12H	21	0256	99.1	108.6	9.5	9.9	104.2	
13H	21	0425	108.6	118.1	9.5	9.9	103.8	
14H	21		118.1					With APCT3; lost HPCS coring assembly in hole
				Cored totals:	118.1	112.7	95.4	

Notes: CSF = core depth below seafloor. APCT3 = advanced piston corer temperature tool, HPCS = hydraulic piston coring system.

Table T2. Coring summary, Hole C0001F. (See table notes.)

Hole C0001F
Latitude: 33°14.3437′N
Longitude: 136°42.7067′E
Time on hole (h): 68.5 (0830 h, 21 Nov 2007–0500 h, 24 Nov 2007)
Seafloor (drillers measurement from rig floor, m): 2225.5
Distance between rig floor and sea level (m): 28.5
Water depth (drillers measurement from sea level, m): 2197
Total depth (drillers depth below rig floor, m): 2474.3
Total penetration (core depth below seafloor, m): 248.8
Total length of cored section (m): 140.9
Total core recovered (m): 137.5
Core recovery (%): 97.6
Total number of cores: 21

Core	Date (Nov 2007)	Local time (h)	Depth CSF (m)		Length (m)		Recovery (%)	Comments
			Top	Bottom	Cored	Recovered		
315-C0001F-								
1H	21	1552	108.0	117.5	9.5	9.5	100.0	
2H	21	1726	117.5	127.0	9.5	9.5	100.0	With APCT3
3H	21	2021	127.0	136.5	9.5	5.0	52.1	
4H	21	2223	136.5	146.0	9.5	9.0	94.7	Overdrilled 3 m; 40 cm of bottom of liner is broken
5H	22	0205	146.0	155.5	9.5	9.9	104.0	With APCT3
6H	22	0347	155.5	161.5	6.0	6.0	100.0	Pumped twice; shot timing unclear
7H	22	0825	161.5	171.0	9.5	9.5	100.0	Overdrilled 3 m; hard to pull out liner
8H	22	1215	171.0	179.7	8.8	8.8	100.0	With APCT3; overdrilled 6 m
9H	22	1352	179.7	189.2	9.5	9.5	100.0	
10H	22	1553	189.2	196.8	7.5	7.5	100.0	Middle 4 m core liner burst
11H	22	1740	196.8	200.8	4.0	6.0	150.0	With APCT3; top and bottom were loose sand; recovery was 9.48 m; upper half of core became slime; Curator decided total length = ~ 6 m
12H	22	2009	200.8	202.4	1.6	1.6	100.0	Prepuncture liner surface for safety
13H	22	2137	202.4	207.2	4.8	4.8	100.0	
14H	22	2303	207.2	213.3	6.1	6.1	100.0	
15H	23	0058	213.3	218.9	5.6	5.6	100.0	Lower part of core tube covered with very fine sandy silt; difficult to pull out
16H	23	0239	218.9	219.6	0.8	0.8	100.0	
17H	23	0400	219.6	220.3	0.7	0.7	100.0	Pump pressure did not increase; gravity coring applied
18H	23	0629	220.3	226.5	6.2	6.2	100.0	
19H	23	0824	226.5	229.8	3.3	3.3	100.0	Formation too stiff for HPCS
20X	23	1247	229.8	239.3	9.5	9.3	98.3	Severe drilling disturbance
21X	23	1541	239.3	248.8	9.5	9.0	94.8	Severe drilling disturbance
				Cored totals:	140.8	137.5	97.6	

Notes: CSF = core depth below seafloor. APCT3 = advanced piston corer temperature tool, HPCS = hydraulic piston coring system. APCT3 measurements were abandoned because of the time required to take an accurate measurement.

Table T3. Coring summary, Hole C0001G. (See table note.)

Hole C0001G
Latitude: 33°14.3237′N
Longitude: 136°42.6933′E
Time on hole (h): 6.25 (0845 h, 24 Nov 2007–1500 h, 24 Nov 2007)
Seafloor (drillers measurement from rig floor, m): 2225
Distance between rig floor and sea level (m): 28.5
Water depth (drillers measurement from sea level, m): 2196.5
Total depth (drillers depth below rig floor, m): 2299.5
Total penetration (meters below seafloor, mbsf): 74.5
Total length of cored section (m): 0
Total core recovered (m): 0
Core recovery (%): NA
Total number of cores: 0

Note: The ROV cable became entangled around the drill pipe and the hole had to be abandoned.

Table T4. Coring summary, Hole C0001H. (See table notes.)

Hole C0001H
Latitude: 33°14.3233′N
Longitude: 136°42.6840′E
Time on hole (h): 229 (0000 h, 26 Nov 2007–1300 h, 5 Dec 2007)
Seafloor (drillers measurement from rig floor, m): 2225.5
Distance between rig floor and sea level (m): 28.5
Water depth (drillers measurement from sea level, m): 2197
Total depth (drillers depth below rig floor, m): 2816
Total penetration (core depth below seafloor, m): 590.5
Total length of cored section (m): 228.6
Total core recovered (m): 126.3
Core recovery (%): 55.2
Total number of cores: 26

	Date	Local time	CSF (m)		Length (m)		Recovery	
Core	(Nov 2007)	(h)	Top	Bottom	Cored	Recovered	(%)	Comments
315-C0001H-								
1R	26	1704	230.0	239.5	9.5	3.9	41.4	
2R	26	1829	239.5	249.0	9.5	6.8	71.2	
3R	26	2008	249.0	258.5	9.5	5.4	56.3	
4R	26	2213	258.5	268.0	9.5	6.7	70.7	
5R	26	2332	268.0	277.5	9.5	4.0	41.6	Changed core catcher type from flapper + finger to finger + slip
6R	27	0137	277.5	287.0	9.5	2.4	25.5	
7R	27	0355	287.0	296.5	9.5	8.7	92.0	Change pump rate; higher WOB and ROP
8R	27	1020	296.5	302.5	6.0	9.0	149.2	6 m core for connection; soft, sticky, washed
9R	27	1150	302.5	312.0	9.5	1.8	18.4	
10R	27	1301	312.0	321.5	9.5	7.5	79.3	
11R	27	1513	321.5	331.0	9.5	7.7	81.1	
12R	27	1616	331.0	340.5	9.5	7.4	77.6	
13R	27	1734	340.5	350.0	9.5	8.5	89.1	
14R	27	1853	350.0	359.5	9.5	6.9	72.4	
15R	27	2002	359.5	369.0	9.5	5.2	54.4	Circulation mud in top of liner
16R	27	2107	369.0	378.5	9.5	5.8	61.4	
17R	27	2255	378.5	388.0	9.5	2.3	24.3	
18R	28	0023	388.0	397.5	9.5	3.7	38.5	Decrease pump rate; caving gravels at the top interval (15 cm)
19R	28	0204	397.5	407.0	9.5	3.3	35.1	
20R	28	0537	407.0	412.5	5.5	0.5	8.4	Change to advance-by-recovery for improving recovery; cavings at top of core
21R	28	0750	412.5	419.5	7.0	6.6	94.6	WOB, ROP increased
22R	28	0920	419.5	429.0	9.5	3.1	32.9	
23R	28	1147	429.0	438.5	9.5	3.3	34.6	
24R	28	1307	438.5	448.0	9.5	3.3	35.1	FFF installation
25R	30	0733	447.2	456.2	9.0	2.3	25.9	Caving at top 50 cm
26R	30	1015	456.2	457.8	1.6	0.3	18.1	Stop coring because of BHA change
				Cored totals:	228.6	126.3	55.2	

Notes: CSF = core depth below seafloor. Hole was drilled from 457.8 to 590.5 m CSF. WOB = weight on bit, ROP = rate of penetration. FFF = free-fall funnel.

Table T5. Coring summary, Hole C0001I. (See table note.)

Hole C0001I
Latitude: 33°14.2030′N
Longitude: 136°42.4330′E
Time on hole (h): 34.5 (1550 h, 5 Dec 2007–0230 h, 8 Dec 2007)
Seafloor (drillers measurement from rig floor, m): 2227.0
Distance between rig floor and sea level (m): 28.5
Water depth (drillers measurement from sea level, m): 2198.5
Total depth (drillers depth below rig floor, m): 2747
Total penetration (meters below seafloor, mbsf): 520
Total length of cored section (m): 0
Total core recovered (m): 0
Core recovery (%): NA
Total number of cores: 0

Note: The hole caved, a drill pipe became stuck, and the hole had to be abandoned.

Table T6. Summary of lithologic units, Site C0001. (See table note.)

Depth CSF (m)	Unit	Subunit	Lithology	Environmental interpretation
0.00–168.35	I	A	Silty clay, volcanic ash	Hemipelagic settling and ash falls on trench slope, well above CCD
168.35–196.76		B	Silty clay, thin silt beds	Hemipelagic settling and silty turbidity currents near base of trench slope
196.76–207.17		C	Sand, silty clay	Sandy turbidity currents at base of trench slope
207.17–456.50	II		Silty clay, rare layers of silt, sand, and volcanic ash	Hemipelagic settling below CCD, probably near outer margin of trench wedge

Note: CSF = core depth below seafloor, CCD = carbonate compensation depth.

Table T7. Results of X-ray diffraction analysis, random bulk powder, Site C0001. (See table notes.) (Continued on next two pages.)

											Abundance calculated from SVD normalization factors								
			Peak intensity (counts/step)				Integrated peak area (total counts)				Absolute (wt%)					Normalized (wt%)			
Unit	Hole, core, section, interval (cm)	Depth CSF (m)	Total clay	Quartz (101)	Plagioclase	Calcite	Total clay	Quartz	Plagioclase	Calcite	Total clay	Quartz	Plagioclase	Calcite	Total	Total clay	Quartz	Plagioclase	Calcite
	315-																		
I	C0001E-1H-3, 100	2.59	30	624	149	584	2,274	22,582	10,768	22,255	30.2	12.5	12.9	26.3	82.0	36.8	15.3	15.8	32.1
	C0001E-1H-4, 19	3.07	35	1,031	199	351	2,525	36,352	16,808	13,882	36.1	20.3	20.5	14.5	91.5	39.5	22.2	22.5	15.9
	C0001E-1H-6, 0	3.80	33	773	171	461	2,519	27,167	12,777	18,566	33.7	15.1	15.4	21.1	85.3	39.5	17.7	18.1	24.7
	C0001E-1H-7, 0	4.03	21	560	133	304	1,973	21,036	10,884	12,810	27.0	11.6	13.3	14.2	66.2	40.8	17.6	20.1	21.5
	C0001E-2H-3, 34	7.45	25	630	119	677	1,875	23,876	9,805	25,976	25.7	13.4	11.7	31.5	82.2	31.2	16.3	14.2	38.3
	C0001E-2H-4, 10	8.73	27	806	166	709	2,022	28,215	11,651	26,905	28.3	15.9	13.9	32.4	90.5	31.3	17.5	15.4	35.8
	C0001E-2H-5, 132	10.17	26	596	115	886	1,880	22,509	8,465	32,772	25.1	12.7	9.9	40.4	88.1	28.5	14.4	11.2	45.9
	C0001E-2H-6, 140	11.76	27	749	133	723	1,688	27,753	10,663	27,237	24.3	15.7	12.7	33.1	85.8	28.3	18.3	14.8	38.6
	C0001E-4H-2, 52	25.12	32	963	195	336	2,304	34,005	16,279	12,831	33.6	19.0	20.0	13.4	86.0	39.1	22.1	23.3	15.6
	C0001E-4H-2, 95	25.55	34	945	177	403	2,805	32,715	12,398	14,415	35.8	18.3	14.6	15.3	84.0	42.7	21.8	17.3	18.2
	C0001E-4H-4, 0	27.41	31	998	173	350	2,730	34,797	13,171	12,474	35.5	19.5	15.6	12.7	83.3	42.6	23.4	18.7	15.3
	C0001E-5H-3, 54	36.18	37	821	177	397	2,826	29,307	15,048	14,346	38.1	16.2	18.4	15.2	87.9	43.4	18.4	20.9	17.3
	C0001E-5H-4, 0	36.93	38	1,060	190	315	3,025	35,807	13,192	12,067	38.4	20.0	15.5	12.0	85.8	44.7	23.4	18.0	13.9
	C0001E-5H-6, 60	39.33	40	784	175	217	3,575	38,365	14,468	10,470	44.5	21.4	16.9	9.3	92.2	48.3	23.2	18.4	10.1
	C0001E-6H-1, 95	43.05	42	964	183	306	2,988	35,156	13,715	11,983	38.4	19.6	16.2	11.9	86.1	44.6	22.8	18.8	13.8
	C0001E-6H-3, 30	45.22	31	780	168	605	2,341	28,847	11,687	22,585	31.3	16.2	13.9	26.5	87.8	35.6	18.4	15.8	30.2
	C0001E-6H-4, 0	46.12	35	797	128	688	2,470	29,469	10,428	24,300	31.7	16.6	12.1	28.6	89.0	35.6	18.6	13.6	32.2
	C0001E-6H-6, 25	48.02	34	951	159	515	2,289	33,513	11,765	18,972	30.4	18.9	13.8	21.6	84.8	35.9	22.3	16.3	25.5
	C0001E-6H-6, 50	48.26	41	842	149	487	2,871	31,041	11,694	18,363	36.2	17.4	13.7	20.5	87.7	41.3	19.8	15.6	23.4
	C0001E-7H-2, 20	53.20	30	1,018	212	373	2,627	37,623	14,453	15,406	35.4	21.1	17.2	16.5	90.2	39.2	23.4	19.1	18.3
	C0001E-7H-4, 0	55.73	32	759	154	539	2,117	28,706	11,900	21,518	29.2	16.1	14.3	25.2	84.8	34.4	19.0	16.8	29.8
	C0001E-7H-5, 8	56.02	35	970	179	397	2,763	35,360	15,703	15,247	37.7	19.7	19.0	16.2	92.7	40.7	21.3	20.5	17.5
	C0001E-7H-7, 70	58.27	34	722	142	549	2,546	27,389	12,010	20,369	33.5	15.2	14.3	23.5	86.6	38.7	17.6	16.6	27.1

Table T7 (continued). (Continued on next page.)

											Abundance calculated from SVD normalization factors								
			Peak intensity (counts/step)				Integrated peak area (total counts)				Absolute (wt%)					Normalized (wt%)			
Unit	Hole, core, section, interval (cm)	Depth CSF (m)	Total clay	Quartz (101)	Plagioclase	Calcite	Total clay	Quartz	Plagioclase	Calcite	Total clay	Quartz	Plagioclase	Calcite	Total	Total clay	Quartz	Plagioclase	Calcite
	C0001E-8H-3, 90	64.84	38	831	146	480	3,009	30,381	11,950	17,710	37.8	16.9	14.0	19.6	88.3	42.8	19.2	15.9	22.2
	C0001E-8H-4, 0	65.16	34	958	249	269	2,724	34,147	38,382	9,963	53.7	18.0	50.2	8.6	130.5	41.2	13.8	38.5	6.6
	C0001E-9H-2, 49	72.50	37	931	143	358	3,074	32,633	11,770	13,974	38.0	18.2	13.6	14.6	84.5	45.0	21.6	16.1	17.2
	C0001E-9H-2, 129	73.30	33	762	135	484	2,913	28,397	10,998	18,613	36.3	15.8	12.8	20.9	85.8	42.3	18.4	14.9	24.4
	C0001E-9H-4, 0	74.78	35	919	201	410	2,683	33,372	14,291	15,659	36.0	18.6	17.2	16.9	88.8	40.6	21.0	19.3	19.1
	C0001E-9H-5, 132	76.32	36	973	205	311	2,692	35,736	16,174	12,469	37.2	19.9	19.7	12.6	89.4	41.6	22.3	22.0	14.1
	C0001E-9H-8, 119	80.49	28	737	156	558	2,358	26,731	11,876	21,718	31.6	14.9	14.2	25.4	86.2	36.7	17.3	16.5	29.5
	C0001E-10H-3, 20	83.24	36	746	128	473	2,704	27,639	11,302	18,426	34.5	15.4	13.3	20.8	84.0	41.0	18.3	15.9	24.8
	C0001E-10H-5, 90	85.42	32	847	161	166	2,635	31,016	11,602	5,996	33.3	17.3	13.6	4.5	68.8	48.4	25.2	19.8	6.6
	C0001E-10H-7, 0	87.17	46	1,136	209	115	2,976	41,185	16,060	4,812	39.4	23.1	19.2	2.2	83.9	47.0	27.5	22.9	2.7
	C0001E-11H-1, 100	90.60	39	834	176	359	3,091	30,104	13,063	13,916	39.3	16.7	15.5	14.5	86.0	45.7	19.4	18.1	16.9
	C0001E-11H-4, 19	93.80	50	979	152	304	3,663	35,710	11,927	11,584	43.7	19.9	13.5	10.9	88.1	49.6	22.6	15.4	12.4
	C0001E-11H-5, 116	94.98	37	968	185	255	2,950	35,514	14,903	10,458	38.8	19.8	17.9	9.9	86.3	45.0	22.9	20.7	11.4
	C0001E-12H-3, 130	103.20	22	354	392	96	2,147	14,030	19,311	4,130	34.8	7.1	25.2	2.7	69.8	49.9	10.2	36.1	3.8
	C0001E-12H-4, 23	103.55	34	824	166	449	2,907	30,718	12,267	16,966	37.0	17.1	14.5	18.6	87.2	42.4	19.6	16.6	21.4
	C0001E-12H-5, 0	104.51	40	708	145	471	3,015	25,953	12,468	17,637	38.4	14.3	14.9	19.6	87.2	44.1	16.4	17.1	22.4
	C0001E-13H-4, 0	112.67	45	996	163	109	3,845	35,667	14,157	4,530	46.9	19.8	16.6	1.5	84.7	55.3	23.3	19.6	1.7
	C0001E-13H-6, 50	114.86	40	768	137	546	3,211	28,043	11,546	20,194	39.7	15.5	13.5	22.7	91.5	43.4	17.0	14.7	24.9
	C0001E-13H-8, 109	118.37	40	1,225	175	247	3,243	40,656	14,019	9,746	40.8	22.8	16.3	8.6	88.5	46.1	25.8	18.4	9.7
	C0001F-1H-1, 10	108.10	35	833	141	475	3,285	29,442	10,976	18,733	39.9	16.4	12.6	20.8	89.6	44.5	18.3	14.1	23.1
	C0001F-1H-4, 0	111.99	33	706	140	515	2,881	27,971	12,105	19,931	36.8	15.5	14.4	22.6	89.3	41.2	17.4	16.1	25.3
	C0001F-2H-3, 33	120.65	37	808	144	426	2,928	29,488	12,746	16,641	37.6	16.4	15.2	18.2	87.3	43.0	18.8	17.4	20.9
	C0001F-2H-5, 0	122.94	42	803	161	431	2,503	29,984	13,186	17,450	33.7	16.7	15.9	19.6	85.8	39.3	19.5	18.5	22.8
	C0001F-3H-1, 130	128.30	30	843	161	424	2,375	30,648	12,740	15,734	32.0	17.1	15.3	17.4	81.8	39.1	21.0	18.7	21.3
	C0001F-3H-2, 80	129.22	29	884	170	452	2,620	33,026	13,480	16,327	34.9	18.5	16.1	17.9	87.3	39.9	21.2	18.4	20.5
	C0001F-4H-3, 0	139.10	33	932	156	290	3,118	33,713	13,668	11,021	39.7	18.8	16.2	10.6	85.2	46.6	22.0	19.0	12.4
	C0001F-4H-5, 89	141.61	38	1,059	230	191	3,207	38,931	18,828	7,402	43.9	21.6	23.0	5.4	93.9	46.7	23.0	24.5	5.8
	C0001F-4H-7, 82	144.45	29	702	153	452	2,435	25,977	12,631	17,870	32.8	14.4	15.3	20.3	82.8	39.6	17.4	18.5	24.5
	C0001F-5H-1, 59	146.59	33	964	220	269	2,788	35,672	17,419	11,096	39.1	19.8	21.3	10.7	90.9	43.0	21.8	23.5	11.8
	C0001F-5H-2, 15	147.50	39	924	216	215	3,727	33,656	15,305	8,438	46.8	18.6	18.3	6.7	90.3	51.8	20.6	20.2	7.4
	C0001F-5H-4, 0	149.88	35	912	171	304	3,038	32,868	15,308	11,254	40.1	18.2	18.5	10.9	87.7	45.7	20.8	21.1	12.4
	C0001F-6H-4, 20	158.64	42	801	151	317	3,306	30,979	13,130	13,022	41.4	17.2	15.5	13.1	87.2	47.4	19.7	17.8	15.1
	C0001F-6H-5, 0	158.66	45	850	170	295	4,086	31,500	14,612	11,704	50.1	17.3	17.3	10.8	95.4	52.5	18.1	18.1	11.3
	C0001F-6H-6, 120	161.08	38	798	142	348	3,134	29,233	13,075	12,814	39.7	16.2	15.6	13.1	84.5	47.0	19.1	18.4	15.5
	C0001F-7H-12, 20	168.14	42	905	189	238	3,560	32,875	14,410	9,279	44.6	18.2	17.1	8.0	87.8	50.7	20.7	19.5	9.1
	C0001F-8H-1, 0	170.98	40	900	174	327	2,888	32,792	14,713	11,614	38.2	18.2	17.7	11.5	85.7	44.6	21.3	20.7	13.4
	C0001F-8H-1, 130	172.28	46	1,076	219	48	3,954	39,510	17,830	2,145	50.3	21.8	21.4	0.1	93.7	53.7	23.3	22.9	0.1
	C0001F-8H-2, 65	173.04	37	983	180	144	3,184	34,843	14,930	5,398	41.0	19.4	17.9	3.1	81.3	50.4	23.8	22.0	3.8
	C0001F-8H-6, 50	177.26	39	869	196	311	3,298	31,925	15,338	13,240	42.9	17.6	18.5	13.3	92.3	46.4	19.1	20.0	14.4
	C0001F-9H-1, 118	180.92	34	1,113	212	108	3,061	38,934	16,234	3,709	40.4	21.7	19.5	0.8	82.4	49.0	26.3	23.7	1.0
	C0001F-9H-4, 0	183.89	39	965	229	251	2,796	35,206	18,688	9,269	40.0	19.5	23.1	8.3	90.9	44.0	21.4	25.4	9.1
	C0001F-9H-CC, 79	190.72	41	868	166	244	2,979	31,976	17,112	9,684	40.8	17.6	21.0	8.8	88.3	46.2	19.9	23.8	10.0
	C0001F-10H-10, 0	193.25	33	938	222	225	3,033	35,593	19,786	8,547	43.1	19.6	24.5	7.1	94.4	45.7	20.8	26.0	7.5
	C0001F-10H-11, 14	193.60	38	1,071	181	191	4,136	37,825	14,813	6,838	50.2	21.0	17.3	4.2	92.6	54.2	22.6	18.7	4.5
	C0001F-10H-11, 129	194.75	29	907	240	254	2,792	32,219	19,629	10,020	40.8	17.7	24.5	9.3	92.4	44.2	19.1	26.6	10.1
	C0001F-13H-1, 0	202.37	29	1,842	281	110	2,111	60,310	33,627	3,982	42.7	33.7	42.6	0.6	119.6	35.7	28.2	35.6	0.5
															Average:	42.9	20.3	19.6	17.2
	315-																		
II	C0001F-14H-1, 50	207.67	45	885	168	90	4,479	31,258	13,815	3,006	53.0	17.1	16.2	0.1	86.4	61.4	19.8	18.7	0.1
	C0001F-14H-2, 54	209.12	37	748	130	192	2,888	27,433	12,420	7,672	36.6	15.2	14.9	6.6	73.3	50.0	20.7	20.3	9.0
	C0001F-14H-3, 90	210.91	42	939	147	86	4,097	34,942	13,135	3,038	48.6	19.3	15.2	0.1	83.2	58.4	23.2	18.2	0.1
	C0001F-14H-4, 0	211.21	39	687	111	99	3,514	25,237	10,570	4,041	41.4	13.8	12.3	1.5	69.1	60.0	20.0	17.8	2.2
	C0001F-15H-2, 10	214.81	44	843	135	167	3,427	30,729	12,097	6,870	41.6	17.0	14.1	5.1	77.7	53.5	21.9	18.1	6.5
	C0001F-15H-2, 44	215.15	42	936	166	132	3,858	33,035	13,820	5,310	46.9	18.2	16.2	2.6	83.9	55.9	21.7	19.4	3.1
	C0001F-15H-4, 0	217.19	47	938	221	0	4,879	33,505	18,739	0	60.3	18.1	22.7	0.0	101.2	59.7	17.9	22.4	0.0
	C0001F-18H-4, 20	222.82	53	891	159	100	4,883	33,417	12,837	4,243	56.3	18.3	14.6	0.4	89.6	62.8	20.5	16.3	0.5
	C0001F-18H-6, 62	224.89	50	883	179	62	4,503	33,602	13,498	2,235	52.9	18.5	15.6	0.1	87.1	60.8	21.2	17.9	0.1
	C0001F-18H-6, 108	225.35	53	972	169	33	5,547	34,757	13,076	1,647	62.8	19.0	14.7	0.1	96.6	65.0	19.7	15.2	0.1
	C0001F-19H-4, 0	228.45	57	1,061	152	0	5,266	38,254	12,257	0	59.2	21.1	13.5	0.0	93.8	63.1	22.5	14.4	0.0
	C0001F-19H-4, 19	228.64	61	969	144	0	5,444	35,248	11,311	0	60.4	19.4	12.3	0.0	92.1	65.6	21.0	13.3	0.0
	C0001F-20X-5, 0	235.21	50	907	290	99	4,132	33,159	15,813	3,955	51.0	18.2	18.9	0.5	88.6	57.6	20.5	21.3	0.6
	C0001F-21X-4, 0	243.27	55	918	192	0	5,195	34,062	13,640	0	59.7	18.6	15.6	0.0	93.9	63.6	19.8	16.6	0.0
	C0001H-1R-3, 0	230.00	50	1,007	169	54	4,590	36,969	13,207	1,947	53.4	20.4	15.0	0.1	88.9	60.0	23.0	16.9	0.1
	C0001H-1R-4, 95	233.79	54	945	145	39	5,159	34,095	12,944	1,614	58.9	18.7	14.6	0.1	92.3	63.8	20.2	15.8	0.1

Table T7 (continued).

											Abundance calculated from SVD normalization factors								
			Peak intensity (counts/step)				Integrated peak area (total counts)				Absolute (wt%)					Normalized (wt%)			
Unit	Hole, core, section, interval (cm)	Depth CSF (m)	Total clay	Quartz (101)	Plagioclase	Calcite	Total clay	Quartz	Plagioclase	Calcite	Total clay	Quartz	Plagioclase	Calcite	Total	Total clay	Quartz	Plagioclase	Calcite
	C0001H-2R-2, 128	242.12	52	921	169	71	4,562	32,777	11,924	3,043	52.4	18.0	13.5	0.1	84.0	62.4	21.5	16.0	0.1
	C0001H-2R-3, 105	243.37	51	890	148	0	4,638	31,684	12,439	0	53.5	17.4	14.2	0.0	85.0	62.9	20.4	16.7	0.0
	C0001H-3R-2, 107	251.48	58	974	168	94	4,784	34,606	12,680	3,978	55.1	19.1	14.3	0.1	88.6	62.2	21.5	16.2	0.2
	C0001H-3R-4, 0	252.82	53	834	118	127	4,566	32,020	10,497	6,159	51.6	17.7	11.5	3.3	84.1	61.3	21.0	13.7	3.9
	C0001H-4R-4, 0	262.33	53	993	160	42	5,076	35,987	12,850	2,272	58.0	19.8	14.4	0.1	92.3	62.8	21.5	15.6	0.1
	C0001H-4R-6, 61	264.78	55	899	158	43	4,363	34,863	12,881	2,449	51.0	19.3	14.7	0.1	85.1	59.9	22.6	17.3	0.1
	C0001H-5R-2, 75	270.17	58	954	137	114	4,701	33,989	11,326	5,185	53.4	18.8	12.5	1.8	86.5	61.7	21.7	14.5	2.1
	C0001H-5R-3, 0	270.42	60	822	131	57	5,371	30,001	10,496	2,581	59.5	16.3	11.4	0.1	87.3	68.1	18.7	13.1	0.1
	C0001H-6R-1, 50	278.00	53	1,003	147	49	5,249	35,954	12,295	2,635	59.3	19.8	13.6	0.1	92.8	63.9	21.3	14.7	0.1
	C0001H-6R-2, 0	278.49	58	965	143	99	5,202	34,511	11,225	4,964	58.2	19.0	12.2	1.2	90.6	64.3	21.0	13.5	1.3
	C0001H-7R-2, 66	289.07	47	863	147	0	4,500	31,018	10,674	0	50.8	17.1	11.9	0.0	79.8	63.7	21.4	14.9	0.0
	C0001H-7R-3, 20	290.05	61	1,010	130	45	5,265	35,993	11,467	2,033	58.8	19.8	12.5	0.1	91.3	64.5	21.7	13.7	0.1
	C0001H-7R-3, 38	290.23	54	1,029	161	45	4,597	37,586	12,430	2,296	52.9	20.8	13.9	0.1	87.7	60.3	23.8	15.9	0.1
	C0001H-7R-4, 39	291.24	54	1,003	156	79	4,638	36,476	13,084	3,535	53.8	20.2	14.9	0.1	89.0	60.5	22.7	16.7	0.1
	C0001H-7R-5, 66	291.94	63	1,115	149	0	5,269	38,318	11,912	0	59.0	21.2	13.0	0.0	93.2	63.3	22.7	13.9	0.0
	C0001H-7R-6, 29	292.98	58	992	175	63	5,003	35,110	12,133	3,089	56.8	19.3	13.5	0.1	89.8	63.3	21.5	15.1	0.1
	C0001H-8R-1, 55	297.05	52	974	132	111	5,539	34,529	11,502	5,240	61.8	18.9	12.5	1.3	94.5	65.4	20.0	13.2	1.3
	C0001H-8R-4, 20	301.12	61	891	142	64	5,201	32,257	12,390	2,866	59.1	17.6	13.9	0.1	90.7	65.1	19.4	15.4	0.1
	C0001H-10R-3, 28	315.14	56	1035	126	46	4,349	37,292	10,569	2,452	49.1	20.8	11.5	0.1	81.4	60.3	25.5	14.1	0.1
	C0001H-10R-3, 71	315.57	54	1031	152	0	4,812	38,437	12,218	0	54.7	21.3	13.5	0.0	89.5	61.1	23.8	15.1	0.0
	C0001H-10R-4, 0	315.86	64	925	158	0	4,931	35,807	12,288	0	56.0	19.7	13.7	0.0	89.5	62.6	22.1	15.3	0.0
	C0001H-10R-7, 5	319.18	55	955	162	68	4,770	36,039	12,842	3,072	55.0	19.9	14.5	0.1	89.5	61.4	22.2	16.2	0.1
	C0001H-11R-2, 20	323.12	55	894	129	87	5,133	33,781	10,885	4,207	57.3	18.6	11.8	0.3	88.0	65.1	21.1	13.4	0.3
	C0001H-11R-4, 0	325.34	60	1,135	133	0	4,921	39,423	11,522	0	55.2	21.9	12.5	0.0	89.6	61.6	24.4	13.9	0.0
	C0001H-12R-2, 104	333.45	52	970	175	0	5,089	35,321	13,749	0	58.7	19.4	15.7	0.0	93.8	62.6	20.7	16.7	0.0
	C0001H-12R-4, 0	333.48	56	940	162	121	4,697	32,475	12,231	5,188	54.1	17.8	13.8	1.9	87.6	61.7	20.4	15.8	2.1
	C0001H-12R-5, 97	336.24	54	935	152	83	4,851	34,029	12,689	3,769	55.8	18.7	14.4	0.1	89.0	62.7	21.0	16.1	0.1
	C0001H-13R-5, 0	345.74	50	917	148	125	4,564	34,246	12,560	5,140	52.9	18.9	14.3	1.8	87.9	60.2	21.5	16.2	2.1
	C0001H-13R-6, 59	346.75	61	837	121	0	5,514	32,007	10,849	0	61.0	17.5	11.8	0.0	90.2	67.6	19.4	13.0	0.0
	C0001H-14R-3, 59	353.42	63	914	125	126	5,711	31,544	11,197	5,485	63.4	17.2	12.2	1.6	94.3	67.2	18.2	12.9	1.7
	C0001H-14R-4, 0	353.83	59	772	130	109	4,920	27,877	10,997	4,762	55.6	15.1	12.3	1.3	84.4	65.9	18.0	14.6	1.6
	C0001H-14R-6, 76	356.42	58	882	124	77	5,325	32,138	10,774	3,471	59.2	17.6	11.7	0.1	88.6	66.8	19.9	13.2	0.1
	C0001H-15R-1, 95	360.45	51	899	136	178	4,977	32,391	12,044	6,340	56.8	17.8	13.5	3.2	91.2	62.2	19.5	14.8	3.5
	C0001H-15R-1, 112	360.62	59	873	145	162	5,568	32,602	11,680	6,225	62.3	17.8	12.8	2.6	95.5	65.2	18.6	13.4	2.7
	C0001H-15R-5, 8	363.92	46	798	134	76	4,727	29,298	12,355	3,408	54.5	16.0	14.2	0.1	84.8	64.3	18.8	16.7	0.1
	C0001H-16R-3, 84	372.67	45	970	159	136	4,464	34,150	12,599	5,625	52.0	18.8	14.3	2.5	87.7	59.3	21.5	16.4	2.9
	C0001H-16R-4, 0	372.83	52	987	157	134	4,679	34,255	11,492	5,046	53.3	18.9	12.8	1.7	86.6	61.5	21.8	14.7	1.9
	C0001H-16R-5, 126	374.52	58	931	139	104	4,968	32,727	11,442	4,321	56.1	18.0	12.7	0.5	87.3	64.3	20.6	14.5	0.6
	C0001H-17R-2, 74	380.65	57	794	136	145	4,616	28,864	12,109	5,537	53.4	15.7	13.9	2.5	85.5	62.4	18.4	16.2	2.9
	C0001H-18R-1, 44	388.44	58	947	146	0	5,404	33,487	11,659	0	60.4	18.3	12.8	0.0	91.5	66.0	20.0	14.0	0.0
	C0001H-18R-3, 22	390.65	53	894	142	0	5,003	32,611	12,213	0	56.9	17.9	13.8	0.0	88.5	64.3	20.2	15.5	0.0
	C0001H-19R-2, 65	399.57	47	810	181	123	4,627	29,423	12,571	5,087	53.8	16.0	14.5	1.9	86.1	62.4	18.6	16.8	2.2
	C0001H-19R-2, 76	399.68	54	865	136	127	5,152	30,848	13,326	5,606	59.5	16.8	15.3	2.1	93.6	63.5	17.9	16.3	2.2
	C0001H-19R-3, 39	400.30	45	808	116	220	3,970	28,421	9,351	8,819	45.1	15.7	10.3	7.4	78.5	57.5	20.0	13.1	9.4
	C0001H-19R-4, 15	400.48	56	843	190	153	5,360	30,313	13,661	6,513	61.8	16.4	15.7	3.1	97.1	63.7	16.9	16.2	3.2
	C0001H-21R-2, 66	414.57	47	856	131	44	4,131	31,293	11,986	2,062	48.2	17.2	13.7	0.1	79.3	60.8	21.7	17.3	0.1
	C0001H-21R-3, 0	414.89	51	985	163	51	4,804	35,203	12,635	2,736	55.2	19.4	14.3	0.1	88.9	62.1	21.8	16.0	0.1
	C0001H-21R-4, 71	416.06	49	930	177	94	4,743	34,055	14,329	4,225	55.9	18.7	16.6	0.4	91.7	61.0	20.4	18.2	0.5
	C0001H-22R-2, 92	421.84	56	922	149	66	5,313	34,400	11,725	3,594	59.6	18.9	12.9	0.1	91.5	65.2	20.6	14.1	0.1
	C0001H-23R-2, 0	430.42	64	963	137	63	5,592	34,387	12,097	3,071	62.6	18.8	13.3	0.1	94.9	66.0	19.8	14.0	0.1
	C0001H-23R-3, 20	430.93	53	954	154	82	4,937	34,221	12,978	3,568	56.8	18.8	14.7	0.1	90.5	62.8	20.8	16.3	0.1
	C0001H-24R-1, 36	438.86	61	872	165	195	5,644	32,632	12,297	8,015	63.6	17.8	13.6	4.9	99.9	63.7	17.8	13.7	4.9
	C0001H-24R-2, 0	439.94	53	900	144	171	4,709	32,542	11,241	6,904	53.5	17.9	12.5	4.1	88.1	60.8	20.4	14.2	4.7
	C0001H-24R-3, 19	440.54	45	585	96	81	4,720	22,605	9,179	4,277	52.5	12.2	10.1	1.1	75.9	69.2	16.0	13.4	1.4
	C0001H-25R-1, 69	447.89	55	906	138	205	4,898	32,366	11,220	8,168	55.5	17.8	12.4	5.6	91.3	60.7	19.5	13.6	6.2
	C0001H-25R-1, 100	448.20	54	875	126	96	5,523	32,813	11,633	43,46	61.8	17.9	12.8	0.2	92.6	66.7	19.4	13.8	0.2
	C0001H-25R-2, 9	448.70	52	924	121	164	5,270	32,898	10,821	6,992	58.8	18.1	11.7	3.8	92.4	63.6	19.5	12.7	4.2
															Average:	62.5	20.6	15.6	1.3

Notes: CSF = core depth below seafloor. SVD = singular value decomposition.

Table T8. Calcareous nannofossil range chart, Hole C0001E. (**See table notes.**)

Epoch	Zone	Core, section, interval (cm)	Depth CSF (m)	Abundance	Preservation	*Calcidiscus leptoporus*	*Calcidiscus macintyrei*	*Ceratolithus cristatus*	*Coccolithus miopelagicus*	*Coccolithus pelagicus* (without bar)	*Discoaster* spp.	*Emiliania huxleyi*	*Florisphaera profunda*	*Gephyrocapsa* spp. large (>5.5 µm)	*Gephyrocapsa* spp. medium (>3.5–4 µm)	*Gephyrocapsa* spp. medium II (>4–5.5 µm)	*Gephyrocapsa* spp. small (<3.5 µm)	*Helicosphaera carteri*	*Helicosphaera* sp.	*Helicosphaera sellii*	*Helicosphaera wallichii*	*Micula* sp.	*Oolithotus fragilis*	*Pontosphaera japonica*	*Pontosphaera multipora*	*Pseudoemiliania lacunosa*	*Pseudoemiliania ovata*	*Reticulofenestra asanoi*	*Reticulofenestra minutula*	*Reticulofenestra pseudoumbilicus* (5–7 µm)	*Reticulofenestra* sp.	*Rhabdosphaera clavigera*	*Scapholithus fossilis*	*Scyphosphaera* spp.	*Syracosphaera pulchra*	*Syracosphaera* spp.	*Umbellosphaera irregularis*	*Umbellosphaera tenuis*	*Umbilicosphaera foliosa*	*Umbilicosphaera sibogae*
Pleistocene		315-C0001E-																																						
	NN21	1H-2, 10.0	0.70	A	G	C						A	A	F	C	C	C		F		F	R														F	F	C	F	
		1H-3, 38.0	1.83	A	G	F		F		F		C	A		A	C	A	C					C			C														
	NN20	1H-CC, 20–25	4.11	A	G	C							A	A	D	A	D	C					C			F														
	NN19	2H-CC, 48.5	13.62	A	G			R			R		C	C	A		A	F								F	F									R		F	R	F
		3H-CC, 23–28	14.28	A	G								A	C	A		A	R					F				C									F			F	C
		4H-CC, 23.5–28.5	32.59	A	M	C							A	C	C	C	D	F					F			C	F												F	F
		5H-CC, 44.5	42.12	A	M	F			R				C				D						F			R	C									F		C	F	
		6H-CC, 32.5–37.5	51.60	A	G	F							A		C		D	F			F					C	C							R				F		F
		7H-CC, 29.5–34.5	61.10	A	G	C							A		A		A									C	A	C										C		
		8H-CC, 45.5–50.5	70.63	A	M	C	R				R		A				A						C		F	C	A	C	C			R							F	
		9H-CC, 29–34	80.10	A	M	C							C	C	C	C	D						F		R	C	A			C			R			C		C	F	C
		10H-CC, 23.5–28.5	89.60	A	M	C							A	A			A						F			C	C							F						F
		11H-CC, 26.5–31.5	99.10	R	P								A	F	F		A									F	C				C							F		
		12H-CC, 21–26	108.60	C	G	C					R		C			F	D	R		R	R		F	R	R	F	R		F			R	F			R		F		F
		13H-CC, 25–30	118.10	C	M	C				F			A		C	C	D	F		R					R	C	C		C	F			R		R			R		

Notes: CSF = core depth below seafloor. Abundance: D = dominant, A = abundant, C = common, F = few, R = rare. Preservation: G = good, M = medium, P = poor.

Table T9. Calcareous nannofossil range chart, Hole C0001F. (See table notes.) (Continued on next page.)

Epoch	Zone	Core, section, interval (cm)	Depth CSF (m)	Abundance	Preservation	*Amaurolithus* spp.	*Braarudosphaera bigelowii*	*Calcidiscus tropicus*	*Calcidiscus leptoporus*	*Calcidiscus macintyrei*	*Ceratolithus acutus*	*Ceratolithus cristatus*	*Ceratolithus cristatus* var. *telesmus*	*Coccolithus pelagicus* (without bar)	*Discoaster brouweri*	*Discoaster pentaradiatus*	*Discoaster* spp.	*Discoaster surculus*	*Discoaster tamalis*	*Discoaster triradiatus*	*Discoaster variabilis*	*Florisphaera profunda*	*Gephyrocapsa* spp. large (>5.5 µm)	*Gephyrocapsa* spp. medium (>3.5–4 µm)	*Gephyrocapsa* spp. medium II (>4–5.5 µm)	*Gephyrocapsa* spp. small (<3.5 µm)	*Helicosphaera carteri*	*Helicosphaera* sp.	*Helicosphaera sellii*	*Helicosphaera wallichii*
		315-C0001F-																												
Pleistocene	NN19	1H-CC, 23.5–28.5	117.50	A	G				C													C	C	A	C	D	C	C		
		2H-CC, 22–27	127.00	C	M				C					F									C	C	A	D	C		F	
		3H-CC, 51–56	131.97	A	G				C													C	C	A	C	A	F	F	R	
		4H-CC, 12.5–17.5	145.95	C	M				C					F								A		A	C	A	C			C
		5H-CC, 0–5	155.48	A	G				C					F										C		D				
		6H-CC, 21–26	161.50	C	G				C													A		A		A				
		7H-CC, 71–76	170.98	C	M				C	F		F		F								A		F		A	C		C	
		8H-CC, 45–50	179.75	C	G			C	C	C			F	F			F					D				C				
		9H-CC, 27.5–32.5	189.24	F–C	M			R	C	C		R					R					A				A				
Pliocene	NN18	10H-CC, 37–42	195.79	R–F	P				C					C	C	F						C				C	C			
		11H-CC, 13–18	200.76	R	G				C					A		C	F									C	C			
		12H-CC, 18–23	202.34	R	M			C	C	C				C	C	F										A	C			
		13H-CC, 20–25	207.16	R	P				C					F	C	C	C									C				
		14H-CC, 0–5	213.27	F	P			C	C						C	A	C	C												
		15H-CC, 29–34	218.89	F	P			F	C	C					C	C		F			A	F				F	F			
		16H-CC, 19.5–24.5	219.64	R	P			C		F					C	C	C	C		F	C									
	NN15–NN13	17H-CC, 13–18	220.29	C	G–P			R	R	F	R			R				R	R		R	A		R	F	C	F	F		
		18H-CC, 0–1	226.18	C	M			F	C			F		R	F	C	C	F			F	A				C				
		19H-CC, 33–38	229.83	R	P					F				C		C	C	C				A				C				
		20X-CC, 49.5–54.5	239.33	R	P	F	F	C	C			F			C	C	C	F			C	A					F			
		21X-CC, 24.5–29.5	248.71	R	P							F			C	C	A				C	A								

Notes: CSF = core depth below seafloor. Abundance: D = dominant, A = abundant, C = common, F = few, R = rare. Preservation: G = good, M = medium, P = poor.

Table T9 (continued).

Epoch	Zone	Core, section, interval (cm)	Depth CSF (m)	Abundance	Preservation	*Oolithotus fragilis*	*Pontosphaera japonica*	*Pontosphaera multipora*	*Pseudoemiliania lacunosa*	*Pseudoemiliania ovata*	*Reticulofenestra minutula*	*Reticulofenestra pseudoumbilicus* (5–7 µm)	*Reticulofenestra pseudoumbilicus* (>7 µm)	*Reticulofenestra* sp.	*Reticulofenestra* spp.	*Rhabdosphaera clavigera*	*Scapholithus fossilis*	*Scyphosphaera* spp.	*Sphenolithus abies*	*Sphenolithus* spp.	*Syracosphaera pulchra*	*Syracosphaera* spp.	*Umbilicosphaera annulus*	*Umbilicosphaera foliosa*	*Umbilicosphaera jafari*	*Umbilicosphaera rotula*	*Umbilicosphaera sibogae*
		315-C0001F-																									
Pleistocene	NN19	1H-CC, 23.5–28.5	117.50	A	G			C	C												C	C					
		2H-CC, 22–27	127.00	C	M		C		F	F																	
		3H-CC, 51–56	131.97	A	G			F	C	C											R	F					R
		4H-CC, 12.5–17.5	145.95	C	M			F	C	C																	
		5H-CC, 0–5	155.48	A	G				C		C																
		6H-CC, 21–26	161.50	C	G	C			C	A	C										C						
		7H-CC, 71–76	170.98	C	M		F		C	A	A													F	F		
		8H-CC, 45–50	179.75	C	G		F		C	C	C					C					F	C					
		9H-CC, 27.5–32.5	189.24	F–C	M				C	C	C																
Pliocene	NN18	10H-CC, 37–42	195.79	R–F	P				A	A	C		C	C	C								C				
		11H-CC, 13–18	200.76	R	G			F	A	A	A							F									
		12H-CC, 18–23	202.34	R	M					A	A			C						F							
		13H-CC, 20–25	207.16	R	P		C		A	C	A	C											C				
		14H-CC, 0–5	213.27	F	P				C	C	A																
		15H-CC, 29–34	218.89	F	P					C	A		D	C												C	
		16H-CC, 19.5–24.5	219.64	R	P						A	C	D					F	C								
		17H-CC, 13–18	220.29	C	G–P		R		A	A	C		F	F			R										
	NN15–NN13	18H-CC, 0–1	226.18	C	M					C	A	F	C	C					F							R	F
		19H-CC, 33–38	229.83	R	P						A	C	A	C	C								C			C	
		20X-CC, 49.5–54.5	239.33	R	P						A		C		C				F								
		21X-CC, 24.5–29.5	248.71	R	P						A	C	C		C												

Table T10. Calcareous nannofossil range chart, Hole C0001H. (See table notes.)

Epoch	Zone	Core, section, interval (cm)	Depth CSF (m)	Abundance	Preservation	*Amaurolithus delicatus*	*Amaurolithus primus*	*Calcidiscus tropicus*	*Calcidiscus leptoporus*	*Calcidiscus macintyrei*	*Ceratolithus acutus*	*Ceratolithus larrymayeri*	*Ceratolithus rugosus*	*Coccolithus pelagicus* (without bar)	*Discoaster asymmetricus*	*Discoaster berggrenii*	*Discoaster bollii*	*Discoaster brouweri*	*Discoaster exilis*	*Discoaster loeblichii*	*Discoaster pentaradiatus*	*Discoaster quinqueramus*	*Discoaster* sp. (short arms, prom. knob)	*Discoaster* spp.	*Discoaster surculus*	*Discoaster variabilis*	*Florisphaera profunda*	*Helicosphaera carteri*	*Pontosphaera japonica*	*Pontosphaera multipora*	*Reticulofenestra haquii*	*Reticulofenestra minuta*	*Reticulofenestra pseudoumbilicus* (5–7 µm)	*Reticulofenestra pseudoumbilicus* (>7 µm)	*Reticulofenestra rotaria*	*Reticulofenestra* sp.	*Reticulofenestra* sp. (with grill)	*Reticulofenestra* spp.	*Rhabdosphaera clavigera*	*Sphenolithus abies*	*Sphenolithus grandis*	*Sphenolithus* spp.	*Syracosphaera* spp.	*Umbilicosphaera annulus*	*Umbilicosphaera rotula*
		315-C0001H-																																											
Pliocene	NN15–NN13	1R-CC, 26–31	234.25	F	P			C	F	F			R					C			F	R		C	C	F	A			F	C	A		C		C				C					
		2R-CC, 0–5	246.35	C	P–M			F	F	F								F	R					C	F	F	C				A	D		C				F		C	C				
		3R-CC, 0–5	254.41	C	M			C	C	R	R		F					R			C	R		C		F	A	C			C	A	C	C		F			F	C	R				R
		4R-CC, 21–26	265.54	C	M–G			C	C	R	R		F					R			C	R		C		F	A	C			C	A	C	C		F			F	C	R				R
		5R-CC, 0–5	272.00	F	P–M			C	C					F				F			C			C	F	C	A	C			C	A	C	C	F					F					F
		6R-CC, 35–40	280.32	F	P			F	F					R							C			C	F	F	C				A	D	C	R	F	C				C	R				
		7R-CC, 35–40	296.47	R	P-M			C										C				F		C			A				C	A	C	C									C		C
		8R-CC, 16–21	302.55	R	M			F																C	C	F	A	F		C	C	A		A											
		9R-CC, 0–5	304.31	R	P																			D																					
		10R-CC, 26.5–31.5	319.56	R	P			C			F			C				C						C	C	C	A	F			A	A	C	F		C				F					
		11R-CC, 0–5	329.42	R	P			C																A			F				A		A												
		12R-CC, 0–5	338.52	R	P–M					F				C				F			F			C	F		D				C	A	C	F						F					C
		13R-CC, 0–5	349.06	F	M–G			C		F				C	F			F			C			C	C	F	A				A	A	C	A	C					C	F				F
		14R-CC, 23–28	357.22	R	P-M				C												C			C	F						C	A	A												C
		15R-CC, 22–27	365.08	F	M			C	C					F				C			C	F		A	F		A	F			A	A	A	C							F				C
		16R-CC, 17.5–22.5	375.10	R	P			C									F	F	C			F		A	F		A				C	A	A	F						F					F
		17R-CC, 0–5	380.81	F	M			C			C		C			C		C			C		F	C	C		A				A	D	C	F	F										C
		18R-CC, 0–5	391.71	F	M			F			R					C		F						C			F				A	A	A			F				F				F	
		19R-CC, 0–5	400.87	F	P					C	C							F		C	C	F		C	C		A	F			A	A	C			C				F					
		20R-CC, 0–5	407.47	R	P				C					F		F							F	A	C		C				A	A	A							C					
		21R-CC, 0–5	417.82	F	M	R	R		C									F			R	F	F	C	F		C				C	D	C	C			F			C	F				
		22R-CC, 0–5	422.71	C	M–G			F	F			R	F			F		F			C			C	C		C	R			A	D	C	C	R					C					F
	NN12	23R-CC, 29–34	431.56	C	M			F	F	R				R		R		R			R	R	F	C	F	F	A	R	R		C	D	C		R					C		R			R
		24R-CC, 0–5	441.84	F	M–G	R	R		C		R			R		R		F			C		F	C	F	C					C	C	R							C					
		25R-CC, 0-5	449.53	F	M	R	R		C		R			R		R		F			C			C	F	C		R			C	C	F	F						C		R			
Miocene		26R-CC, 15–20	456.55	F	P				F							R		F			F			C	F		R				C	C	F	F						C					

Notes: CSF = core depth below seafloor. Abundance: D = dominant, A = abundant, C = common, F = few, R = rare. Preservation: G = good, M = medium, P = poor.

Table T11. Nannofossil events, Site C0001. (**See table notes.**)

Zone	Age (Ma)	Event	Top: Core, section, interval (cm)	Top: Depth CSF (m)	Bottom: Core, section, interval (cm)	Bottom: Depth CSF (m)	Mean depth CSF (m)	Range (±m)
			314-C0001B-		314-C0001B-			
NN21	0.291	FO *Emiliania huxleyi*	1H-CC, 0–5	2.11	2H-CC, 0–5	11.86	6.99	4.87
NN20	0.436	LO *Pseudoemiliania lacunosa*	2H-CC, 0–5	11.86	3H-CC, 15–17	22.06	16.96	5.10
			315-C0001E-		315-C0001E-			
	0.063	X *Gephyrocapsa* spp. (>3.5 µm)–*Emiliania huxleyi*	1H-2, 10	0.17	1H-3, 38	1.83	1.00	0.89
NN21	0.291	FO *Emiliania huxleyi*	1H-3, 38	1.83	1H-5, 18	3.02	2.43	0.66
NN20	0.436	LO *Pseudoemiliania lacunosa*	2H-6, 16.5	10.10	2H-7, 16.5	11.50	10.80	0.70
	0.9	LCO *Reticulofenestra asanoi*	7H-2, 80	53.63	7H-5, 75	57.58	55.61	1.97
	1.04	RE *Gephyrocapsa* spp. (≥4 µm)	8H-CC, 48	68.07	9H-CC, 31.5	80.10	74.09	6.02
			315-C0001F-		315-C0001F-			
	1.24	LO *Gephyrocapsa* spp. (>5.5 µm)	3H-CC, 51.0	131.97	4H-CC, 12.5–17.5	145.95	138.96	6.99
	1.6	LO *Calcidiscus macintyrei* (≥11 µm)	6H-CC, 23.5	161.50	7H-CC, 71–76	171.02	166.26	4.76
NN19	2.06	LO *Discoaster brouweri*	9H-CC, 27.5	189.25	10H-CC, 37–42	195.79	192.52	3.27
NN16	3.79	LO *Reticulofenestra pseudoumbilicus* (>7 µm)	17H-CC, 13–18	220.31	18H-CC	226.18	223.25	2.94
			315-C0001H-		315-C0001H-			
	5.04	LO *Ceratolithus acutus*	16R-CC, 17.5–22.5	374.92	17R-CC, 0–5	380.83	377.87	2.95
	4.5	LO *Amaurolithus primus*	21R-CC, 0–5	417.85	22R-2, 139–140	422.32	420.08	2.23
NN13	5.12	FO *Ceratolithus rugosus*	22R-CC, 0–5	422.71	23R-CC, 29–34	431.56	427.13	4.42
	5.32	FO *Ceratolithus acutus*	25R-CC, 0–5	449.53	26R-CC, 0–5	456.55	453.04	3.51

Notes: CSF = core depth below seafloor. FO = first occurrence, LO = last occurrence, X = crossover in abundance, LCO = last consistent occurrence, RE = reentrance.

Table T12. Planktonic foraminifer range chart, Hole C0001E. (**See table notes.**)

Epoch	Zone	Core, section, interval (cm)	Depth CSF (m)	Abundance	Preservation	*Globigerina bulloides*	*Globigerina falconensis*	*Globigerinella siphonifera*	*Globigerinita glutinata*	*Globigerinoides conglobatus*	*Globigerinoides ruber*	*Globigerinoides ruber rosa*	*Globigerinoides sacculifer*	*Globoconella inflata* modern form	*Globoconella inflata* transitional form	*Globoconella puncticulata*	*Globorotalia scitula*	*Globorotalia tumida*	*Globoturborotalita obliquus*	*Hirsutella hirsuta*	*Menardella menardii*	*Neogloboquadrina dutertrei*	*Neogloboquadrina humerosa*	*Neogloboquadrina incompta*	*Neogloboquadrina kagaensis*	*Neogloboquadrina pachyderma* dextral form	*Neogloboquadrina pachyderma* sinistral form	*Orbulina universa*	*Pulleniatina finalis*	*Pulleniatina* spp. dextral form	*Pulleniatina* spp. sinistral form	*Sphaeroidinella dehiscens*	*Truncorotalia crassaformis*	*Truncorotalia crassaformis hessi*	*Truncorotalia crassaformis viola*	*Truncorotalia tosaensis*	*Truncorotalia truncatulinoides*	*Turborotalita quinqueloba*
Pleistocene	N22	315-C0001E-																																				
		1H-1, 7–9	0.07	A	M	C		+	R	+	R		+	C	C		+	+			+	R		A				+	+	R			+				+	+
		1H-2, 36–40	0.47	A	G	R	+		R		+		+	R	C		+	+			+	R		A				+	+	+			+				+	+
		1H-3, 81–83	2.27	A	G	A	+	+	C	+	C	+	+	C	R		+	+			+	C		C				+	+	C			+				+	
		1H-5, 39–43	3.26	A	G	C	+	+	R	+	R	+	+	+	R		+	+			+	+		A			+	+	+	+			+				+	
		1H-CC, 20–25	4.11	A	G	A			+	+	C	+	+	A	+			+			+	C		A				+	+	A			+				+	
		2H-2, 12–16	5.64	A	G	C	+	+	R	+	C	+	+	+	+		+	+			+	R		A			+	+	+	+			+				+	
		2H-3, 12–16	7.04	A	G	+	R	+	R	+	R	R	+	A	C		+	+		+	+	C		+				+	+	R		+	+	+			R	+
		2H-5, 14–18	8.68	A	G	+	+		R	+	+	+	+	A	C		+	+			+	C		A				+	+	C			+	+				
		2H-6, 17–21	10.12	A	G	C	R	+	C	+	R		+	R	+		+	+			+	+		A		+		+	+	R			+					+
		2H-CC, 46–51	13.60	A	G	+		+	+	+	R		+	A							+	A		A				+	+	C			+				+	
		3H-CC, 23–28	14.28	A	G	+		+	+	+	+		+	+	+		+	+				+		A				+	+	+			+			+		+
		4H-CC, 23.5–28.5	32.59	A	G	C	+	R	+		R		+	A	R		+	+	+		+	R		A			+	+		+			+			+		+
		5H-CC, 42–47	42.10	C	G	R	A	+	+	+	C		+	A	R		+	+				+		R				+		+			+	+		+		
		6H-CC, 32.5–37.5	51.60	A	G	+	R	+	+	+	+		+	C	+	+	+	+			+	+		A				+					+	+	+	+		+
		7H-CC, 29.5–34.5	61.07	A	G	R			+		+		+	C	A	R		+			+	+		A				+		R		+	R			+	+	
		8H-CC, 45.5–50.5	70.60	A	G	+	+	+		+	+		+	C	A	+		+			+	+		A				+	+	R		+	+					
		9H-CC, 29–34	80.10	A	M	R	+	+	C		+		+	A	C	+		+				+		A				+	+	+		+	+			+		
		10H-CC, 23.5–28.5	89.60	A	G	+	+	+	+		R		+	A	A	+	+	+			+	R		C				+	+	+			+			+		
		11H-CC, 26.5–31.5	99.10	C	M	R	+		C	+	+		+	A	A	+		+					+	+		+		+		+			+			+	+	
		12H-CC, 21–26	108.60	A	G	C	+		+	+	R		+	C	A	+	+	+	+		+	+	+	A	+		+	+			+	+	+			+	+	+
		13H-CC, 25–30	118.10	A	G	R	R		+	+	C		+	C	R	+		+	+			+	R	A	+		+	+		+		+	+			+	+	R

Notes: CSF = core depth below seafloor. Abundance: A = abundant, C = common, R = rare, + = present. Preservation: G = good, M = medium.

Table T13. Planktonic foraminifer range chart, Hole C0001F. (**See table notes.**)

Epoch	Zone	Core, section, interval (cm)	Depth CSF (m)	Abundance	Preservation	*Dentoglobigerina altispira*	*Globigerina bulloides*	*Globigerina falconensis*	*Globigerinella obesa*	*Globigerinita glutinata*	*Globigerinita uvula*	*Globigerinoides conglobatus*	*Globigerinoides ruber*	*Globigerinoides ruber rosa*	*Globigerinoides sacculifer*	*Globoconella conoidea*	*Globoconella conomiozea*	*Globoconella inflata* modern form	*Globoconella inflata* transitional form	*Globoconella puncticulata*	*Globoconella sphericomiozea*	*Globorotalia scitula*	*Globorotalia tumida*	*Globoturborotalita decoraperta*	*Globoturborotalita extremus*	*Globoturborotalita obliquus*	*Menardella menardii*	*Menardella pseudomiocenica*	*Neogloboquadrina acostaensis* dextral form	*Neogloboquadrina asanoi*	*Neogloboquadrina* cf. *asanoi*	*Neogloboquadrina dutertrei*	*Neogloboquadrina humerosa*	*Neogloboquadrina incompta*	*Neogloboquadrina kagaensis*	*Neogloboquadrina pachyderma* dextral form	*Neogloboquadrina pachyderma* sinistral form	*Neogloboquadrina praehumerosa*	*Orbulina universa*	*Pulleniatina finalis*	*Pulleniatina* spp. dextral form	*Pulleniatina* spp. sinistral form	*Sphaeroidinella dehiscens*	*Sphaeroidinellopsis seminulina*	*Sphaeroidinellopsis subdehiscens*	*Truncorotalia crassaformis*	*Truncorotalia tosaensis*	*Truncorotalia truncatulinoides*	*Turborotalita quinqueloba*
		315-C0001F-																																															
Pleistocene	N22	1H-CC, 23.5–28.5	117.50	C	G		C	+		+		+	+		+			A	A	C			+	+								+	+	A						+	+	+		+			+	+		
			2H-CC, 22–27	127.00	A	G		+	R		+			R		+			A	A	R		+	+				+					+	+	A						+	+					+	+	+	
			3H-CC, 51–56	131.97	C	M		+	R		+			+		+			R	C	C			+	+						+		+	+	A	R				+		R		+			+	+	+	
Pliocene	N21	4H-CC, 12.5–17.5	145.95	C	G		C	+		+			R		+			C	C	C		+	+			+				+			+	A						+		+		+			C			
			5H-CC, 0–5	155.48	C	M		A			C		+	C		R			+	C	+			+							+				A						+		+		+			R			
			6H-CC, 21–26	161.50	C	G		A			+			A		+			R	C				+										+	A	+	+			+		+		+			+	+		+
			7H-CC, 71–76	170.98	C	M		A	+		A			+		+			+	C	+			+			+	+			+			+	A	+	C	+		+			+	+			+	+		
			8H-CC, 45–50	179.75	C	M		+			C		+	+		+			A	A	R			R											+	C		+				+		+	+						
			9H-CC, 27.5–32.5	189.24	R	M		+	+		A			+		+				+				+	+			+							+	A	+	A	+		+			+	+				R		
			10H-CC, 37–42	195.79	R	P													+	R	A			+							A					A	+								+						
			11H-CC, 13–18	200.76	R	P		C	R		A	+	+	+		+				C	+		+	+			R	+						+	R	+	A	+		+			+	+			+	+		R
			12H-CC, 18–23	202.34	R	P	+	+	+		+			+		+			+	+	+		+	+			+	+			+			+	+	+				+		+		+			+			
		N18	13H-3, 29–33	203.61	R	M		+			+											+			+	+													+		+						+					+
			13H-4, 44–48	204.16	C	M		A	+	+	+			R		+			+	+	+				+		+				+				A	+	C		+	+							+			
			13H-CC, 20–25	207.16	R	P		+	+		+			+		+			+	+	+				+		+	+							+	+	+	+			+				+			+			
			14H-1, 125–129	208.45	C	M	+	C	+	+	C			+		+	+	+			R	+	+		+		+	+		+	+				C	+	A	+	+	+					+		+			
			14H-2, 28–32	208.86	C	P	+	C	+		+			+		+	+	+			+		+				+			+						A	+	A	+	+	+					+		+	+			+
			14H-3, 53–57	210.52	R	P		+						+		+	+				+								+								+		+		+								+				
			14H-5, 112–116	212.49	C	M	+	+	+		R			C		C	+				+	+	+			+	+	+		+	+				A	+	A	+	+	+					+			+			
			14H-CC, 0–5	213.27	C	M		R	+		R			+		+	+				R	+		+			+		+									A	+		+		+		+	+		+			
			15H-CC, 29–34	218.89	B	B																																												
			16H-CC, 19.5–24.5	219.64	B	B																																												
			17H-CC, 13–18	220.29	C	G		C	+		+			C	+	+			A	C	+		+	+			+						R	+			A			+		R				+			+	
			18H-CC, 0–1	226.17	R	P					+												+											+		+								+	+			
Pliocene– ? Miocene	?N17b	19H-CC, 33–38	229.75	B	B																																												
			20X-CC, 49.5–54.5	239.33	R	P		C			C		+			+		cf									C											+	A	+	+											
			21X-CC, 24.5–29.5	248.71	R	M		+			+					+											+													+															

Notes: CSF = core depth below seafloor. Abundance: A = abundant, C = common, R = rare, + = present, B = barren. Preservation: G = good, M = medium, P = poor.

Table T14. Planktonic foraminifer range chart, Hole C0001H. (See table notes.)

Epoch	Planktonic foraminifer zone	Core, section, interval (cm)	Depth CSF (m)	Abundance	Preservation	*Candeina nitida*	*Dentoglobigerina altispira*	*Globigerina bulloides*	*Globigerina falconensis*	*Globigerinella obesa*	*Globigerinella siphonifera*	*Globigerinita glutinata*	*Globigerinoides conglobatus*	*Globigerinoides ruber*	*Globigerinoides sacculifer*	*Globoconella conoidea*	*Globoconella conomiozea*	*Globoconella sphericomiozea*	*Globoquadrina baroemoenensis*	*Globorotalia plesiotumida*	*Globorotalia scitula*	*Globorotalia tumida*	*Globorotalia* cf. *tumida*	*Globoturborotalita decoraperta*	*Globoturborotalita extremus*	*Globoturborotalita nepenthes*	*Globoturborotalita obliquus*	*Hirsutella margaritae*	*Menardella menardii*	*Menardella pseudomiocenica*	*Neogloboquadrina acostaensis* dextral form	*Neogloboquadrina acostaensis* sinistral form	*Neogloboquadrina* cf. *asanoi*	*Neogloboquadrina conglomerata*	*Neogloboquadrina humerosa*	*Neogloboquadrina pachyderma* dextral form	*Neogloboquadrina pachyderma* sinistral form	*Neogloboquadrina praehumerosa*	*Orbulina universa*	*Pulleniatina primalis* sinistral form	*Sphaeroidinellopsis seminulina*	*Sphaeroidinellopsis subdehiscens*	*Turborotalita quinqueloba*
early Pliocene	N18	315-C0001H-																																									
		1R-CC, 26–31	234.24	C	G			R	+		+	C			+				+					R			R		C	+						R	A	R	+	+	+	+	
		2R-CC, 0–5	246.34	C	G			+	R		+	C	+	+	+		+	+			+	+				+	+		+					+		C	A	R	+	+	+	+	+
		3R-CC, 0–5	254.41	R	M			+	+			+			+									+	+	+	+		+								+	+	+		+		
		4R-CC, 21–26	265.54	R	M		+	+	+						+	+	+				+		+	+	+		+		+								+	+	+			+	
		5R-CC, 0–5	272.00	R	M		+	+	+							+											+		+							+							
		6R-CC, 35–40	280.32	R	P									+													+														+	+	
		7R-CC, 35–40	296.46	R	M		+	+	+	+		+			+	+	+									+	+		+	+					+	+	+	+	+	+		+	
		8R-CC, 16–21	305.69	R	M			+				+			+												+									+	+	+					
		9R-CC, 0–5	304.30	R	P				+			+				+												+								+	+	+			+		
		10R-CC, 26.5–31.5	319.95	R	M		+	+	+			+			+	+	+							+	+	+	+		+								+	+			+		
		11R-CC, 0–5	329.42	R	M			+	+			+			+	+										+	+		+							+			+		+		
		12R-CC, 0–5	338.52	R	M			+	+	+		+			+	+											+		+		+	+					+	+				+	
		13R-CC, 0–5	349.06	R	M		+	+	+			+			+	+	+			+						+	+		+				+								+		
		14R-CC, 23–28	357.21	R	M			+	+			+			+	+					+							+								+	+		+	+			
		15R-CC, 22–27	365.07	R	M		+	C	R			C		+	R	C	+							+	+	R	A		+							+	+	+	+	+			
		16R-CC, 17.5–22.5	375.10	R	P		+					+			+	+	+			+							+		+					+			+		+		+	+	
		17R-CC, 0–5	380.83	R	P		+	+	+			A			C	+			+	+		+		+			C	R	+							+							
		18R-CC, 0–5	391.74	C	M	+	+	R	R	+		A		+	+	+	+	+	+		+		+	+	+	+	C	+	+	+	+				+	A	R	+	+	+	+	+	+
		19R-CC, 0–5	400.89	R	M		+	+	+			+			+	+	+				+				+	+	+		+					+		+	+		+	+	+	+	
		20R-CC, 0–5	407.50	R	P			+	+			+			+	+								+		+	+		+							+	+				+		
		21R-CC, 0–5	417.85	R	M		+	+		+	+	+		+	+	+	+				+	+	+	+		+	+	+	+								+		+		+		
? late Miocene	N17b	22R-CC, 0–5	422.71	R	P		+	+	+			+		+	+	+					+					+	+		+							+	+	+	+		+		
		23R-CC, 29–34	431.56	R	M			+				+			+												+		+							+	+			+	+		
		24R-CC, 0–5	441.84	R	M		+	+	+		+				+											+	+		+		+					+	+	+	+	+		+	
		25R-CC, 30.5–35.5	449.53	R	P			+	+			+			+												+									+					+	+	
		26R-CC, 15–20	456.55	R	M		+	+	+			+			+												+		+		+					+		+	+	+	+	+	

Notes: CSF = core depth below seafloor. Abundance: A = abundant, C = common, R = rare, + = present. Preservation: G = good, M = medium, P = poor.

Table T15. Planktonic foraminifer events, Site C0001. (**See table notes.**)

Zone	Age (Ma)	Event	Top		Bottom		Mean depth CSF (m)	Range (±m)
			Core, section, interval (cm)	Depth CSF (m)	Core, section, interval (cm)	Depth CSF (m)		
			315-C0001E-		315-C0001E-			
	0.12	LO *Globigerinoides ruber rosa*	1H-2, 36–40	0.47	1H-3W, 81–83	2.27	1.36	0.91
	0.61	LO *Truncorotalia tosaensis*	2H-6, 17–21	10.12	3H-CC, 23–28	14.28	12.20	2.08
	0.80	FO *Truncorotalia crassaformis hessi*	6H-CC, 32.5–37.5	51.60	7H-CC, 29.5–34.5	61.07	56.34	4.74
			315-C0001F-		315-C0001F-			
N.22	1.93	FO *Truncorotalia truncatulinoides*	2H-CC, 22–27	127.00	3H-CC, 51–56	131.97	129.48	2.48
	1.75	SD2 *Pulleniatina* spp.	6H-CC, 21–26	161.50	7H-CC, 71–76	171.01	166.25	4.76
	1.80	LO *Neogloboquadrina asanoi*	9H-CC, 27.5–32.5	189.25	10H-CC, 37–42	195.79	192.52	3.27
N.21	3.35	FO *Truncorotalia tosaensis*	11H-CC, 13–18	200.85	13H-CC, 20–25	207.16	204.00	3.16
	2.40	FO *Globoconella inflata* modern form	13H-CC, 20–25	207.16	14H-1W, 125–129	208.45	207.80	0.64
	3.59	LO *Sphaeroidinellopsis seminulina*	14H-1, 125–129	208.45	14H-2W, 28–32	208.86	208.65	0.21
	3.47	LO *Dentoglobigerina altispira altispira*	14H-2, 28–32	208.86	14H-3W, 53–57	210.52	209.69	0.83
	4.08	SD1 *Pulleniatina* spp.	14H-CC, 0–5	213.27	1R-CC, 26–31	233.96	223.61	10.35
	4.31	FO *Truncorotalia crassaformis*	18H-CC, 0–0	226.17	20X-CC, 49.5–54.5	239.33	232.75	6.58
			315-C0001H-		315-C0001H-			
	4.37	LO *Globoturborotalita nepenthes*	1R-CC, 26–31	233.96	2R-CC, 0–5	246.35	240.15	6.19
N.18	5.57	FO *Globorotalia tumida*	21R-CC, 0–5	417.85	22R-CC, 0–5	431.27	424.56	6.71
N.17b	6.40	FO *Pulleniatina primalis*	26R-CC, 15–20	456.68				

Notes: CSF = core depth below seafloor. LO = last occurrence, FO = first occurrence. SD = change in coiling direction from sinistral to dextral.

Table T16. Remanent magnetization at 20 mT, Hole C0001F. (See table notes.)

Core, section	Declination (°)	Inclination (°)	α95	*N*	*k*
315-C0001F-					
1H-1	**332.7**	**–48.5**	09.8	17	014
1H-2	**318.5**	**–33.5**	14.9	13	009
1H-3	**358.1**	**–42.5**	14.8	15	008
1H-5	**312.1**	**–52.3**	02.7	17	182
1H-6	**312.1**	**–52.6**	04.6	11	098
1H-7	**297.8**	**–50.9**	04.6	20	052
1H-8	**295.7**	**–35.1**	10.0	07	037
1H-9	**266.7**	**–52.6**	14.7	09	013
4H-4	**346.0**	**–49.3**	15.8	22	005
5H-5	126.5	25.7	14.0	12	011
5H-8	**022.8**	**–55.3**	11.1	22	009
5H-9	**336.9**	**–58.4**	08.2	23	015
7H-3	**142.3**	**–40.6**	16.0	18	006
7H-13	**140.5**	**–45.5**	03.4	24	076
8H-3	**340.4**	**–39.4**	13.7	16	008
8H-5	181.3	47.5	11.9	24	007
8H-6	170.5	45.5	04.3	16	074
8H-7	149.5	57.3	06.2	22	026
8H-8	144.6	38.0	10.5	04	078
9H-2	346.7	59.8	09.7	24	010
9H-3	337.7	63.2	13.0	12	012
9H-5	337.4	43.4	05.0	19	046
9H-6	319.5	54.0	04.9	24	038
10H-9	255.9	54.6	03.2	19	114
14H-1	204.2	57.9	17.5	09	010
14H-2	204.0	50.0	08.8	13	023
15H-1	197.0	51.8	09.3	22	012
15H-2	180.1	55.9	08.3	15	022
15H-3	165.8	50.9	13.3	12	012
19H-2	256.1	43.6	08.4	17	019
19H-4	229.2	44.4	12.3	14	011

Notes: Measurements made on archive halves where +*x* = vertical upward direction when the core is sitting with the single line at the bottom, +*y* = direction to the left along the split-core surface when looking upcore, and +*z* = downcore (see Fig. F18). Declination and inclination are for remanent magnetization at 20 mT. If inclination is positive (plain text), then declination needs to be restored to north (360°); if it is negative (bold text), it needs to be restored to the south (180°). α95 = radius of the 95% confidence cone centered around the mean paleomagnetic direction. *N* = number of measurements (= intervals). *k* = Fisher or precision parameter.

Table T17. Magnetic polarity ages, Site C0001. (See table notes.)

Chron/ Subchron	Depth CSF (m)	Age (Ma)
T C1n	0	0
B C1n	85.8	0.781
T C1r.1n	123 ± 4.5	0.988
B C1r.1n	134 ± 3.0	1.072
T C2n	174.7	1.778
B C2n	193.5	1.945
B C3n.4n (?)	320.0	5.235

Notes: CSF = core depth below seafloor. T = top, B = bottom.

Table T18. Interstitial water geochemistry, Site C0001. (See table notes.) (Continued on next page.)

Core, section	Depth CSF (m)	pH	Alkalinity (mM)	Salinity (refractive index)	Cl (mM)	Br (µM)	SO_4 (mM)	PO_4 (µM)	NH_4 (mM)	Na (mM)	K (mM)	Mg (mM)	Ca (mM)	Li (µM)	B (µM)	Mn (µM)
315-C0001E-																
1H-4	3.00	7.69	4.75	1.33933	553.9	902	26.3	7.91	0.23	458	11.3	48.7	8.20	26.0	532	1.53
1H-6	3.91	7.71	5.92	1.33931	554.8	883	22.4	11.1	0.28	466	11.9	49.1	7.99	26.7	502	1.44
1H-7	4.14	7.65	6.14	1.33930	553.4	861	21.8	10.4	0.30	450	12.5	47.7	7.70	26.4	515	1.01
2H-4	8.74	7.88	10.86	1.33916	556.7	922	12.5	21.2	0.57	467	12.0	44.0	5.26	26.1	507	1.06
4H-4	27.52	8.02	19.38	1.33896	556.4	953	0.23	80.3	1.34	470	10.4	35.6	2.27	17.1	437	2.20
5H-4	37.03	7.81	18.53	1.33891	552.6	910	0.18	91.3	1.72	471	10.7	33.3	2.28	16.5	446	1.64
6H-4	46.23	7.73	18.47	1.33887	551.6	981	0.22	66.4	1.99	463	9.89	30.9	2.30	18.3	425	1.56
7H-4	55.83	7.66	18.95	1.33885	551.0	978	0.11	70.6	2.22	478	9.70	29.9	2.67	21.2	419	1.90
8H-4	65.22	7.67	19.12	1.33885	548.4	990	0.17	62.3	2.39	481	9.70	29.0	2.92	27.4	388	2.01
9H-4	74.89	7.67	18.87	1.33884	549.0	990	0.11	40.1	2.57	473	9.76	27.5	3.11	26.4	407	3.12
10H-7	87.27	7.78	18.23	1.33883	544.2	985	0.11	26.3	2.78	474	9.74	26.3	3.21	28.6	381	3.03
11H-4	93.71	7.65	17.67	1.33880	544.2	1010	0.42	38.7	2.74	471	9.65	25.5	3.43	29.7	382	2.27
12H-5	104.62	7.72	16.19	1.33879	545.9	1010	0.24	18.0	2.94	479	9.39	24.4	3.26	29.8	326	3.67
13H-4	112.77	7.66	16.57	1.33876	542.0	1030	0.22	41.5	2.96	471	8.61	21.2	4.29	32.7	332	3.37
315-C0001F-																
1H-4	112.11	7.62	16.91	1.33881	543.9	987	0.13	22.2	2.88	475	9.05	24.2	3.64	32.0	332	3.11
2H-5	123.04	7.64	15.60	1.33879	546.2	1070	0.16	35.4	2.83	484	9.41	25.2	3.56	32.8	306	2.39
4H-3	139.20	7.73	16.12	1.33914	546.4	1120	0.31	28.5	2.96	476	9.23	23.8	3.43	33.8	312	2.54
5H-4	149.98	7.63	15.71	1.33882	547.3	1110	0.21	31.0	2.86	475	8.86	21.8	3.78	40.0	284	3.24
6H-4	158.55	7.6	15.88	1.33875	547.0	1120	0.10	37.0	2.99	484	9.41	25.2	3.56	36.7	290	2.76
7H-12	168.04	7.66	15.62	1.33882	545.4	1150	0.17	26.3	2.85	480	9.15	21.5	4.28	37.7	266	3.13
8H-4	175.11	7.78	14.44	1.33879	549.4	1050	0.15	22.2	2.99	471	9.15	20.9	4.25	39.0	256	2.49
9H-4	184.00	7.59	16.31	1.33881	548.5	1090	0.16	11.4	2.76	502	8.74	21.6	4.72	44.2	284	3.73
10H-10	193.35	7.6	16.52	1.33882	548.9	1110	0.20	23.1	2.78	467	8.71	21.5	4.78	47.0	267	4.94
13H-2	203.23	7.72	16.23	1.33884	547.0	1010	0.88	15.5	2.67	473	8.51	21.9	5.06	53.6	258	5.38
14H-4	211.32	7.64	16.25	1.33883	549.5	1110	0.23	16.5	2.64	486	8.46	21.1	5.12	64.5	261	4.28
15H-4	217.30	7.74	16.09	NA	549.2	1110	0.24	21.5	2.48	494	7.87	21.4	5.56	65.6	211	4.32
18H-4	222.72	7.67	16.89	1.33883	548.7	1080	0.16	16.8	2.36	489	8.21	21.1	5.63	70.3	232	5.12
19H-4	228.34	7.66	15.97	1.33883	549.5	1020	0.16	18.4	2.25	485	7.93	20.8	5.78	70.7	202	4.03
20X-5	235.34	7.54	15.62	1.33884	546.5	1220	0.90	17.1	2.38	483	7.92	21.1	5.89	81.8	246	4.72
21X-4	243.42	7.54	15.72	1.33882	545.0	1080	0.96	13.9	2.25	475	7.78	21.0	6.21	78.6	240	4.80
315-C0001H-																
1R-3	232.63	7.79	15.84	1.33883	549.4	1110	0.08	13.0	2.32	473	7.92	20.6	5.79	76.0	248	4.05
3R-4	253.02	7.74	14.15	1.33881	549.6	1050	0.13	14.2	2.43	463	7.72	20.1	6.47	87.0	230	6.83
4R-4	262.54	7.84	14.72	1.33871	540.0	1060	0.07	10.8	2.17	471	7.21	18.3	6.98	92.6	192	9.34
5R-3	270.64	7.58	14.37	1.33880	550.7	1092	0.07	10.1	2.34	485	8.10	19.4	7.46	106	202	11.7
6R-2	278.71	7.53	13.20	1.33879	552.5	1080	0.07	6.96	2.15	476	7.52	18.6	7.82	110	204	10.9
7R-4	291.06	7.69	13.53	1.33882	550.0	1080	0.06	7.59	2.34	483	7.77	17.1	8.42	116	161	11.1
8R-4	300.93	7.68	11.76	1.33879	551.8	1060	0.15	2.85	2.09	489	7.60	18.2	8.61	117	173	12.3
10R-4	316.06	7.52	13.80	1.33879	552.0	1080	0.03	6.96	2.36	476	7.22	15.3	9.48	130	194	12.0
11R-4	325.55	7.66	11.70	1.33885	551.1	1080	0.13	6.96	2.13	480	7.12	16.1	9.95	139	155	8.84
12R-4	335.06	7.55	11.25	1.33878	553.9	1090	0.04	4.43	2.15	480	6.69	15.1	9.89	142	169	9.60
13R-5	345.95	7.57	11.13	1.33878	555.4	1190	0.02	8.23	2.24	478	6.92	14.3	10.4	159	154	8.16
14R-4	354.04	7.7	10.39	1.33875	552.0	1100	0.04	7.91	2.11	490	6.54	14.0	10.3	152	144	6.47
16R-4	373.04	7.49	10.18	1.33877	553.8	1090	0.02	5.38	2.18	472	6.04	12.8	11.1	164	154	7.38
18R-3	390.64	NA	NA	1.33882	556.0	1070	0.10	5.70	2.45	485	6.61	13.2	11.7	164	165	9.28
19R-3	400.12	7.5	7.60	1.33862	542.1	1030	0.09	0.95	2.27	480	5.90	11.9	11.7	172	155	7.70
21R-3	415.12	7.55	7.73	1.33877	557.2	1020	0.08	2.53	2.21	493	5.97	12.1	12.6	181	140	7.89
23R-2	430.57	7.66	7.48	1.33875	552.4	1100	0.02	3.80	2.15	492	5.45	11.2	13.4	194	142	12.3
24R-2	440.14	7.43	7.05	1.33879	548.8	1090	0.03	6.96	2.05	482	5.13	10.9	13.2	176	143	12.0

Notes: CSF = core depth below seafloor. * = shore-based analyses. NA = not analyzed.

Table T18 (continued).

Core, section, interval (cm)	Depth (mbsf)	Fe (µM)	Si (µM)	Sr (µM)	Ba* (µM)	V* (nM)	Cu* (nM)	Zn* (nM)	Rb* (µM)	Mo* (nM)	Cs* (nM)	Pb* (nM)	U* (nM)	Y* (pM)	δ^{18}O* (‰ VSMOW)	δD* (‰ VSMOW)
315-C0001E-																
1H-4	3.00	15.5	739	84.6	0.29	22	3.22	94.2	1.64	199	2.81	1.05	4.26	NA	–0.15	1.5
1H-6	3.91	12.2	679	85.9	0.31	35	173	195	1.82	157	2.88	2.42	6.30	NA	–0.15	0.0
1H-7	4.14	10.1	774	76.3	0.31	24	13.9	169	1.67	142	2.98	1.95	3.23	NA	–0.21	–1.8
2H-4	8.74	4.22	806	87.6	0.51	42	8.84	322	1.69	42.2	3.79	0.45	1.69	NA	–0.15	–0.3
4H-4	27.52	3.21	835	86.6	50.6	54	13.3	288	1.20	129	3.25	0.26	1.13	0.31	–0.42	–1.0
5H-4	37.03	4.78	824	88.0	69.8	40	14.3	383	1.16	146	2.85	0.05	2.09	NA	–0.49	–6.0
6H-4	46.23	15.2	867	88.9	73.7	38	35.1	187	1.08	103	3.25	1.05	0.70	NA	–0.67	–3.4
7H-4	55.83	28.8	892	93.6	78.9	34	26.9	474	1.14	105	3.17	0.95	1.36	NA	–0.92	–2.4
8H-4	65.22	35.3	867	98.0	85.5	31	0.33	357	1.07	106	2.84	1.08	1.07	NA	–1.25	0.4
9H-4	74.89	37.5	971	99.9	85.7	35	228	547	1.05	188	2.71	0.92	1.30	NA	–1.24	–4.6
10H-7	87.27	29.8	831	105	94.0	36	213	420	1.17	246	3.83	1.98	4.56	NA	–1.36	–6.5
11H-4	93.71	44.2	830	109	97.3	22	1960	882	1.10	165	3.20	5.45	2.09	NA	–1.59	–7.5
12H-5	104.62	76.7	906	110	113	36	117	389	1.05	399	2.98	1.81	1.34	NA	–1.82	–7.8
13H-4	112.77	57.6	932	115	131	35	87.1	874	1.10	225	3.31	0.31	2.56	NA	–2.24	–4.4
315-C0001F-																
1H-4	112.11	50.5	966	113	125	28	116	354	1.02	136	2.88	2.07	0.92	NA	–1.75	–4.5
2H-5	123.04	42.9	961	113	139	43	64.5	1840	1.05	206	3.20	2.35	2.49	NA	–1.79	–5.0
4H-3	139.20	58.6	994	115	195	47	48.3	452	0.99	405	2.81	2.11	2.51	NA	–2.00	–4.9
5H-4	149.98	81.2	965	121	238	42	743	489	0.93	326	2.43	0.89	6.01	NA	–2.09	–5.1
6H-4	158.55	53.7	1140	117	263	34	522	1020	1.01	240	2.90	1.44	1.21	0.12	–1.92	–8.9
7H-12	168.04	76.4	998	120	294	54	1430	626	0.98	406	2.76	1.66	1.60	NA	–2.31	–10
8H-4	175.11	37.9	976	120	314	28	1210	990	1.03	247	3.12	10.1	1.96	NA	–2.31	–6.5
9H-4	184.00	87.3	981	121	350	30	428	854	0.96	366	2.84	1.97	1.70	NA	–2.39	–7.7
10H-10	193.35	85.6	1030	122	363	30	239	620	0.98	432	3.26	5.25	3.95	NA	–2.47	–9.2
13H-2	203.23	68.8	858	109	18.8	35	229	232	1.05	372	3.50	0.55	0.93	NA	–2.38	–7.6
14H-4	211.32	62.3	901	122	391	28	299	866	1.03	317	2.83	1.49	1.07	NA	–2.51	–8.2
15H-4	217.30	8.73	991	126	388	25	398	641	0.82	384	1.73	0.24	5.53	0.64	–2.55	–12
18H-4	222.72	79.2	992	126	403	58	803	709	0.83	475	1.94	1.56	4.52	NA	–2.27	–11
19H-4	228.34	25.5	1110	126	365	61	1120	1230	0.82	195	1.99	NA	3.23	1.35	–2.59	–9.0
20X-5	235.34	55.4	1110	114	33.6	24	1860	885	0.89	353	1.98	0.40	2.43	NA	–2.49	–16
21X-4	243.42	44.2	1200	111	18.8	27	2210	676	0.79	218	1.67	1.57	1.96	NA	–2.59	–12
315-C0001H-																
1R-3	232.63	35.8	1220	115	38.7	34	1310	1420	0.87	215	2.02	1.21	1.82	NA	–2.44	–14
3R-4	253.02	26.6	1220	108	25.9	21	6160	714	0.81	114	1.94	0.18	1.86	NA	–2.52	–12
4R-4	262.54	47.0	1180	115	49.9	26	5730	1530	0.77	198	2.36	4.13	3.97	0.23	–2.72	–14
5R-3	270.64	80.2	1080	117	45.2	25	2330	911	0.86	403	2.41	2.31	1.09	NA	–2.49	–12
6R-2	278.71	78.4	1150	113	28.7	31	312	415	0.74	391	2.11	1.12	1.08	0.75	–2.10	–11
7R-4	291.06	79.8	999	118	34.2	35	403	387	0.83	590	2.94	1.40	1.19	NA	–2.57	–12
8R-4	300.93	105	1030	109	7.50	22	709	350	0.79	732	2.22	2.23	2.18	NA	–2.39	–10
10R-4	316.06	136	1170	132	240	30	1350	1260	0.83	458	3.36	5.34	0.96	0.12	–2.81	–13
11R-4	325.55	60.0	1150	115	8.7	35	501	715	0.80	368	2.82	0.23	2.07	NA	–2.55	–13
12R-4	335.06	103	1340	128	219	24	720	932	0.71	387	2.36	1.10	1.08	0.96	–2.52	–12
13R-5	345.95	81.9	1220	134	239	21	662	1400	0.74	177	2.58	1.26	0.38	NA	–2.99	–11
14R-4	354.04	47.6	1230	134	219	18	606	1510	0.70	295	2.18	1.84	2.41	NA	–2.93	–10
16R-4	373.04	65.0	1380	135	249	15	813	2460	0.72	116	3.06	2.83	1.50	NA	–3.12	–10
18R-3	390.64	79.4	1190	121	53.5	9.4	163	1030	0.78	209	2.82	1.20	0.29	NA	–3.12	–8.8
19R-3	400.12	56.0	1200	122	25.0	8.1	470	1700	0.76	232	2.77	0.38	0.70	0.57	–2.97	–9.9
21R-3	415.12	34.9	1110	126	30.3	7.5	1830	1400	0.80	183	2.98	1.83	1.16	NA	–3.12	–9.5
23R-2	430.57	104	1180	139	222	23	1480	618	0.76	509	2.75	1.43	0.67	0.28	–3.28	–11
24R-2	440.14	105	1350	119	206	11	303	2430	0.71	278	2.62	4.73	0.74	NA	–3.24	–9.9

Table T19. Headspace gas analysis, Site C0001. (**See table notes.**)

Core, section, interval (cm)	Depth CSF (m)	Headspace gas (ppmv)		C_1/C_2
		Methane	Ethane	
315-C0001E-				
1H-2, 147–151	1.55	3.6	ND	—
2H-1, 145.5–149.5	5.56	23.8	ND	—
4H-1, 145–150	24.55	4,750.9	ND	—
5H-1, 148–152	34.08	36,329.6	7.8	4,683
6H-1, 136.5–140.5	43.47	25,720.5	5.8	4,410
7H-1, 136–140	52.96	19,978.9	3.2	6,304
8H-1, 140.5–144.5	62.51	10,555.6	3.3	3,194
9H-1, 137–141	71.97	6,409.9	2.6	2,484
10H-1, 136.5–140.5	81.47	12,879.0	4.1	3,175
11H-1, 137–141	90.97	13,458.7	4.1	3,285
12H-1, 141.5–145.5	100.52	6,679.9	3.1	2,149
13H-1, 136.5–140.5	109.97	5,997.6	2.7	2,185
315-C0001F-				
1H-3, 131.5–140	112.14	5,137.6	2.8	1,820
2H-1, 136.5–140.5	118.87	5,361.0	2.3	2,357
3H-1, 137.5–141.5	128.38	8,223.0	3.1	2,678
4H-1, 136.4–140.5	137.87	4,278.9	2.0	2,107
5H-2, 129.5–133.5	148.64	14,632.3	5.0	2,902
6H-1, 137–141	156.87	9,606.8	4.8	2,008
7H-11, 123–127	167.89	13,885.6	5.0	2,773
8H-1, 137–141	172.35	5,886.6	3.3	1,785
9H-1, 136–140	181.10	5,353.8	3.1	1,736
10H-8, 0–4	191.63	830.5	2.4	342
11H-1, 136–140	198.12	6,463.1	ND	—
12H-1, 115.5–119.5	201.89	10,604.3	3.5	3,048
13H-1, 71.5–75.5	203.09	4,082.5	2.2	1,886
14H-1, 137–141	208.54	6,368.7	3.6	1,786
15H-1, 137.5–141.5	214.67	8,762.3	4.5	1,965
16H-1, 65.5–69.5	219.55	4,010.9	3.8	1,065
18H-3, 136–140	222.79	5,416.5	4.1	1,335
19H-1, 50–54	226.99	7,466.2	5.6	1,327
20X-1, 136–140	231.19	7,205.4	3.6	1,987
21X-2, 136–140	242.10	13,082.6	5.1	2,575
315-C0001H-				
1R-1, 139.5–143.5	231.40	7,858.8	2.8	2,851
2R-1, 137–141	240.87	4,783.2	2.6	1,865
3R-1, 136.5–140.5	250.37	7,270.6	2.8	2,581
4R-1, 137–141	259.87	14,397.4	4.6	3,133
5R-2, 96–100	270.38	23,535.7	5.5	4,257
6R-1, 95–96	278.45	43,883.5	9.2	4,790
7R-1, 136–140	288.36	12,374.9	3.3	3,750
8R-3, 136.5–140.5	300.68	24,803.1	5.4	4,598
9R-1, 137–141	303.87	24,352.8	5.4	4,507
10R-1, 137.5–141.5	313.38	10,668.1	2.9	3,703
11R-1, 138–142	322.88	15,560.6	4.2	3,734
12R-1, 137–141	332.37	17,660.1	4.2	4,164
13R-1, 136.5–140.5	341.87	15,384.9	3.4	4,528
14R-1, 137–141	351.37	6,187.8	2.2	2,763
15R-1, 137–141	360.87	28,193.2	5.4	5,247
16R-1, 137.5–141.5	370.38	15,467.4	3.7	4,209
17R-1, 137–141	379.87	2,861.6	2.2	1,310
18R-1, 137.5–141.5	389.38	7,526.6	2.1	3,559
19R-1, 137.5–141.5	398.88	6,310.5	1.9	3,407
20R-1, 43–47	407.43	4,384.6	1.8	2,504
21R-1, 137–141	413.87	27,243.5	4.0	6,818
22R-1, 141–142	420.91	13,491.8	3.0	4,526
23R-1, 137.5–141.5	430.38	12,624.3	2.7	4,661
24R-1, 139.5–143.5	439.90	5,127.6	ND	—
25R-1, 140.5–141.0	448.61	11,811.4	2.5	4,644

Notes: CSF = core depth below seafloor. ND = not determined, — = not applicable.

Table T20. Carbon, nitrogen, and sulfur, Holes C0001E, C0001F, and C0001H. (See table notes.) (Continued on next two pages.)

Core, section, interval (cm)	Depth CSF (m)	Carbon (wt%)				TN (wt%)	TS (wt%)	C/N
		Total	Inorganic	$CaCO_3$	Organic			
315-C0001E-								
1H-3, 100–101.5	2.60	3.01	2.55	21.27	0.46	0.09	0.18	5.43
1H-4, 19–20	3.08	2.11	1.54	12.84	0.57	0.10	0.35	5.79
1H-6, 0–1	3.80	1.53	1.38	11.48	0.16	0.05	0.63	3.21
1H-7, 0–1	4.03	0.68	0.67	5.59	0.01	0.07	0.45	0.16
2H-3, 34–35	7.46	3.35	2.93	24.40	0.42	0.09	0.36	4.61
2H-4, 10–11	8.73	3.41	3.06	25.48	0.35	0.07	0.36	5.22
2H-5, 132–133	10.17	4.34	3.82	31.87	0.52	0.10	0.18	5.04
2H-6,140–142	11.77	3.71	3.23	26.92	0.48	0.10	0.28	4.64
4H-2, 52–53	25.13	2.15	1.58	13.21	0.56	0.11	0.34	5.16
4H-2, 95–96	25.56	1.98	1.32	11.02	0.66	0.11	1.15	6.21
4H-4, 0–1	27.42	1.68	1.39	11.58	0.29	0.03	0.57	8.67
5H-3, 54–55	36.18	2.01	1.65	13.75	0.36	0.09	0.43	4.21
5H-4, 0–1	36.93	1.35	1.13	9.41	0.22	0.05	0.36	4.89
5H-6, 60–61	39.34	1.30	0.79	6.55	0.52	0.10	0.42	5.33
6H-1, 95–96	43.06	1.57	1.15	9.57	0.43	0.10	0.78	4.39
6H-3, 30–31.5	45.23	3.00	2.53	21.04	0.47	0.10	0.25	4.67
6H-4, 0–1	46.13	3.22	2.85	23.77	0.37	0.07	0.29	5.59
6H-6, 25–26.5	48.02	2.55	2.05	17.09	0.50	0.10	0.34	4.98
6H-6, 49.5–51	48.27	2.43	1.99	16.61	0.43	0.11	0.44	4.04
7H-2, 20–21.5	53.21	2.00	1.61	13.38	0.39	0.08	0.40	4.75
7H-4, 0–1	55.73	2.96	2.62	21.86	0.33	0.05	0.45	7.34
7H-5, 8–9.5	56.03	2.28	1.72	14.34	0.56	0.11	0.35	5.24
7H-7, 70–71.5	58.28	2.97	2.48	20.67	0.49	0.11	0.60	4.39
8H-3, 90–91.5	64.85	2.37	2.02	16.81	0.35	0.09	0.41	3.92
8H-4, 0–1	65.16	1.14	1.03	8.60	0.11	0.05	0.62	2.29
8H-7, 35–36.5	67.36	0.14	0.06	0.51	0.08	0.03	0.60	2.39
9H-2, 49–50	72.51	2.02	1.44	11.98	0.59	0.13	0.38	4.65
9H-2, 129–130	73.31	2.60	2.02	16.79	0.59	0.12	0.31	4.82
9H-4, 0–1	74.79	2.06	1.63	13.62	0.42	0.07	0.31	5.78
9H-5, 132–133	76.32	1.98	1.31	10.90	0.67	0.11	0.44	5.84
9H-8, 118.5–120	80.49	2.86	2.45	20.44	0.40	0.10	0.37	4.17
10H-3, 20–21	83.25	2.40	1.87	15.58	0.53	0.11	0.57	4.85
10H-5, 90–91	85.42	1.29	0.84	6.97	0.45	0.10	2.03	4.54
10H-7, 0–1	87.17	0.74	0.41	3.43	0.33	0.04	1.01	7.77
11H-1, 100–101	90.61	1.91	1.50	12.51	0.41	0.11	0.29	3.85
11H-4, 19–20	93.80	1.49	1.15	9.56	0.34	0.08	0.35	4.42
11H-5, 115.5–117	94.98	1.56	1.07	8.94	0.49	0.11	0.17	4.51
12H-3, 130–131.5	103.21	1.02	0.74	6.15	0.28	0.09	3.15	3.34
12H-4, 23–24.5	103.55	2.12	1.73	14.43	0.39	0.10	0.21	3.78
12H-5, 0–1	104.52	1.97	1.88	15.63	0.10	0.04	0.22	2.50
13H-4, 0–1	112.67	0.59	0.39	3.25	0.20	0.06	0.18	3.44
13H-6, 50–51.5	114.87	2.64	2.24	18.67	0.40	0.10	0.16	3.89
13H-8, 109–110.5	118.37	1.56	1.06	8.86	0.50	0.10	0.42	5.18
315-C0001F-								
1H-1, 10–11.5	108.11	2.52	2.03	16.88	0.49	0.11	0.22	4.49
1H-4, 0–1	112.00	2.50	2.23	18.58	0.27	0.06	0.20	4.37
2H-3, 33–34	120.66	2.21	1.78	14.86	0.43	0.10	0.12	4.20
2H-5, 0–1	122.94	2.06	1.87	15.56	0.19	0.06	0.23	3.11
3H-1, 130–131	128.31	2.15	1.66	13.83	0.49	0.11	0.42	4.27
3H-2, 80–81	129.22	2.03	1.83	15.28	0.20	0.03	0.22	7.81
4H-3, 0–2	139.11	1.49	1.26	10.50	0.23	0.07	0.26	3.36
4H-5, 89–90	141.62	1.36	0.91	7.59	0.45	0.10	0.22	4.37
4H-7, 82–83.5	144.45	2.15	1.73	14.40	0.43	0.11	0.19	3.86
5H-1, 59–60	146.60	1.43	0.91	7.55	0.53	0.11	0.30	4.97
5H-2, 15–16	147.50	1.37	0.84	7.00	0.53	0.12	0.26	4.32
5H-4, 0–1	149.88	1.39	1.24	10.36	0.15	0.06	0.18	2.42
6H-4, 20–21.5	158.65	1.54	1.30	10.84	0.24	0.08	0.66	3.08
6H-5, 0–1	158.66	1.82	1.33	11.06	0.49	0.14	0.26	3.62
6H-6, 120–121.5	161.09	1.91	1.38	11.47	0.53	0.12	0.33	4.25
7H-12, 20–21	168.14	1.17	0.99	8.26	0.18	0.01	0.21	12.45
8H-1, 0–1	170.99	1.63	1.15	9.59	0.48	0.11	0.26	4.35
8H-1, 130–131.5	172.29	0.63	0.17	1.44	0.46	0.11	0.17	4.13
8H-2, 65–66.5	173.05	0.77	0.64	5.34	0.13	0.07	0.21	2.02
8H-6, 50–51.5	177.26	1.92	1.52	12.65	0.40	0.12	0.25	3.46
9H-1, 118–119.5	180.93	0.86	0.39	3.28	0.47	0.11	4.82	4.10
9H-4, 0–1	183.49	1.38	0.98	8.15	0.40	0.09	0.24	4.44

Table T20 (continued). (Continued on next page.)

Core, section, interval (cm)	Depth CSF (m)	Carbon (wt%)				TN (wt%)	TS (wt%)	C/N
		Total	Inorganic	$CaCO_3$	Organic			
9H-CC, 78.5–80	183.90	1.26	1.11	9.23	0.15	0.01	0.23	11.03
10H-10, 0–1	193.25	1.09	0.81	6.75	0.28	0.03	0.18	8.89
10H-11, 13.5–15	193.60	1.18	0.63	5.23	0.55	0.10	0.13	5.30
10H-11, 128.5–130	194.75	1.44	1.06	8.87	0.38	0.08	0.15	4.72
13H-1, 0–1	202.38	0.58	0.38	3.15	0.20	0.03	0.80	5.98
14H-1, 50–51	207.68	0.68	0.41	3.38	0.28	0.08	0.62	3.41
14H-2, 54–55	209.13	1.28	0.85	7.06	0.43	0.09	1.23	4.63
14H-3, 90–91	210.92	0.70	0.25	2.12	0.44	0.10	0.79	4.47
14H-4, 0–1	211.22	0.53	0.39	3.25	0.14	0.05	1.36	2.67
15H-2, 10–11	214.81	1.15	0.68	5.63	0.48	0.11	0.82	4.40
15H-2, 44–45	215.15	1.10	0.63	5.21	0.48	0.12	0.73	4.13
15H-4, 0–1	217.20	0.27	0.02	0.15	0.25	0.07	0.61	3.75
18H-4, 20–21	222.82	0.79	0.43	3.58	0.36	0.10	0.67	3.78
18H-6, 62–63.5	224.90	0.50	0.16	1.33	0.34	0.10	1.20	3.29
18H-6, 108–109.5	225.36	0.64	0.11	0.92	0.53	0.12	0.56	4.50
19H-4, 0–1	228.46	0.31	0.10	0.81	0.22	0.07	0.85	3.24
19H-4, 18.5–20	228.64	0.56	0.11	0.93	0.45	0.11	0.63	4.03
20X-5, 0–1	235.22	0.69	0.22	1.83	0.47	0.06	0.77	7.36
21X-4, 0–1	243.27	0.41	0.21	1.77	0.20	0.06	1.31	3.17
315-C0001H-								
1R-3, 0–1	232.43	0.56	0.37	3.06	0.19	0.06	0.97	2.94
1R-4, 95–96	233.80	0.81	0.29	2.45	0.51	0.08	0.96	6.17
2R-2, 128–129	242.20	0.54	0.10	0.82	0.44	0.08	0.94	5.33
2R-3, 105–106	243.38	0.24	0.06	0.49	0.18	0.08	0.99	2.27
3R-2, 107–108	251.48	0.81	0.38	3.16	0.43	0.09	0.52	4.94
3R-4, 0–1	252.82	0.99	0.71	5.88	0.29	0.09	0.79	3.32
4R-4, 0–1	262.34	0.42	0.22	1.83	0.20	0.08	0.44	2.45
4R-6, 61–62	264.79	0.52	0.18	1.47	0.35	0.07	0.30	4.65
5R-2, 75–76	270.18	0.86	0.52	4.34	0.34	0.08	0.23	4.02
5R-3, 0–2	270.43	0.40	0.29	2.38	0.11	0.08	0.78	1.50
6R-1, 50–51	278.01	0.74	0.30	2.54	0.44	0.11	0.58	4.16
6R-2, 0–1	278.50	0.85	0.55	4.55	0.31	0.09	0.50	3.44
7R-2, 66–67	289.08	0.58	0.22	1.85	0.36	0.09	0.42	3.98
7R-3, 20–21	290.05	0.68	0.23	1.95	0.45	0.08	0.40	5.38
7R-3, 38–39	290.23	0.65	0.20	1.69	0.45	0.09	0.45	4.95
7R-4, 39–40	291.25	0.44	0.20	1.65	0.25	0.08	0.49	3.12
7R-5, 66–67	291.94	0.55	0.11	0.95	0.44	0.10	0.26	4.59
7R-6, 29–30	292.99	0.78	0.29	2.45	0.48	0.10	0.20	4.93
8R-1, 55–56	297.06	1.09	0.67	5.58	0.42	0.09	0.30	4.69
8R-4, 20–21	300.93	0.36	0.22	1.87	0.14	0.08	0.29	1.78
10R-3, 28–29	315.15	0.72	0.25	2.06	0.48	0.09	1.48	5.20
10R-3, 71–72	315.58	0.82	0.30	2.53	0.52	0.10	0.19	5.23
10R-4, 0–1	315.86	0.41	0.21	1.73	0.20	0.08	0.38	2.44
10R-7, 5–6	319.19	0.68	0.31	2.55	0.38	0.09	0.21	4.11
11R-2, 20–21	323.13	0.84	0.40	3.30	0.45	0.10	0.29	4.65
11R-4, 0–1	325.35	0.34	0.13	1.09	0.21	0.08	0.28	2.61
12R-2, 104–105	333.46	0.84	0.30	2.52	0.54	0.11	0.27	5.10
12R-4, 0–1	334.86	0.62	0.46	3.86	0.15	0.08	0.33	1.92
12R-5, 97–98	336.24	0.74	0.40	3.33	0.34	0.09	0.24	3.80
13R-5, 0–1	345.75	0.66	0.60	4.96	0.07	0.07	0.24	1.01
13R-6, 59–60	346.75	0.61	0.22	1.87	0.38	0.09	0.34	4.03
14R-3, 59–60	353.42	0.92	0.51	4.22	0.41	0.11	4.85	3.90
14R-4, 0–1	353.83	0.62	0.46	3.87	0.15	0.08	0.41	1.91
14R-6, 76–77	356.43	0.79	0.26	2.17	0.53	0.10	0.37	5.13
15R-1, 95–96	360.46	1.12	0.61	5.09	0.51	0.11	0.30	4.61
15R-1, 112–113	360.63	1.13	0.59	4.96	0.54	0.11	0.15	4.86
15R-5, 8–9	363.93	0.68	0.38	3.15	0.30	0.09	0.31	3.15
16R-3, 84–85	372.67	1.17	0.66	5.52	0.50	0.08	0.25	6.22
16R-4, 0–1	372.83	0.99	0.57	4.74	0.42	0.06	0.39	7.05
16R-5, 126–127	374.52	1.05	0.61	5.11	0.43	0.08	0.34	5.22
17R-2, 74–75	380.66	0.73	0.45	3.76	0.28	0.05	0.28	5.79
18R-1, 44–45	388.45	0.72	0.27	2.24	0.45	0.09	0.29	5.28
18R-3, 22–4	390.66	0.39	0.09	0.78	0.30	0.07	0.69	4.00
19R-2, 65–66	399.57	0.84	0.41	3.45	0.43	0.09	0.69	4.79
19R-2, 76–77	399.68	1.00	0.52	4.37	0.48	0.10	0.32	4.83
19R-3, 39–40	400.31	1.41	0.81	6.78	0.59	0.10	0.57	6.00
19R-4, 15–16	400.49	1.06	0.56	4.67	0.50	0.10	0.25	5.07
21R-2, 66–67	414.58	0.59	0.20	1.65	0.39	0.09	0.17	4.45

Table T20 (continued).

Core, section, interval (cm)	Depth CSF (m)	Carbon (wt%) Total	Inorganic	$CaCO_3$	Organic	TN (wt%)	TS (wt%)	C/N
21R-3, 0–2	414.90	0.75	0.33	2.74	0.44	0.10	0.33	4.38
21R-4, 71–72	416.07	1.07	0.63	5.28	0.44	0.10	0.17	4.39
22R-2, 92–94	421.85	0.70	0.28	2.35	0.44	0.10	0.74	4.32
23R-2, 01	430.42	0.51	0.23	1.95	0.28	0.10	0.30	2.90
23R-3, 20–21	430.94	0.75	0.39	3.27	0.36	0.09	0.47	3.99
24R-1, 36–37	438.87	1.22	0.76	6.37	0.45	0.09	0.17	4.97
24R-2, 0–1	439.94	1.29	0.94	7.79	0.39	0.10	0.28	4.02
24R-3, 19–20	440.54	0.61	0.37	3.08	0.24	0.07	0.12	3.33
25R-1, 69–70	447.90	0.90	0.63	5.27	0.30	0.08	0.23	3.52
25R-1, 100–101	448.21	0.64	0.40	3.34	0.24	0.08	0.22	3.15
25R-2, 9–10	448.71	0.85	0.49	4.10	0.36	0.09	0.13	3.86

Notes: CSF = core depth below seafloor. TN = total nitrogen, TS = total sulfur, C/N = carbon to nitrogen ratio.

Table T21. Whole-round core sections, Site C0001. (**See table notes.**)

WRC type	Core, section	Depth CSF (m)	Sampling method
	315-C0001E-		
A	1H-2	1	Syringe
A	5H-5	38	Syringe
A	11H-3	93	Syringe
	315-C0001F-		
A	6H-5	159	Syringe
A	10H-1	190	Syringe
A	18H-6	225	Syringe
A	21X-3	243	Syringe
	315-C0001H-		
A	6R-3	280	Intact piece
A	11R-3	325	Intact piece
A	16R-1	370	Intact piece
A	21R-4	416	Intact piece
A	25R-1	448	Intact piece
	315-C0001E-		
B	1H-2	1	Syringe
B	2H-2	6	Syringe
B	2H-6	11	Syringe
B	4H-5	28	Syringe
B	6H-7	50	Syringe
B	8H-6	66	Syringe
B	10H-2	82	Syringe
B	12H-3	102	Syringe
	315-C0001F-		
B	11H-4	202	Syringe
	315-C0001H-		
B	8R-2	298	Intact piece
B	19R-1	399	Intact piece
	315-C0001E-		
C	1H-2	1	Syringe
C	2H-2	6	Syringe
C	2H-6	11	Syringe
C	4H-5	28	Syringe
C	6H-7	50	Syringe
C	8H-6	66	Syringe
C	10H-2	82	Syringe
C	12H-3	102	Syringe
	315-C0001F-		
C	4H-2	138	Syringe
C	11H-4	202	Syringe
C	18H-3	223	Syringe
	315-C0001H-		
C	8R-2	298	Intact piece
C	13R-1	341	Intact piece
C	19R-1	399	Intact piece
C	24R-1	440	Intact piece

Notes: CSF = core depth below seafloor. WRC = whole-round core. WRC type: A = subsampled on board for cell fixing, DNA and RNA extraction, and cultivation studies; B = stored at +4°C for cultivation experiments to be conducted on shore; C = subsampled on board for cell fixing and thereafter stored at –80°C for molecular analysis.

Table T22. Cell abundance in sediments, Site C0001. (**See table note.**)

Core, section, interval (cm)	Sample depth CSF (m)	Cell abundance (cells/cm^3)
315-C0001E-		
1H-2, 0.40–0.55	0.56	4.1E+09
5H-5, 1.05–1.20	38.27	3.7E+09
11H-3, 0.60–0.75	93.08	1.6E+09
315-C0001F-		
6H-5, 0.95–1.10	159.47	1.2E+09
10H-1, 0.87–1.02	190.18	2.4E+09
18H-6, 0.27–0.42	224.62	1.2E+09
21X-3, 0.30–0.45	242.55	9.5E+08
315-C0001H-		
6R-3, 0.60–0.70	279.57	6.9E+08
11R-3, 0.39–0.54	324.80	7.8E+08
16R-1, 1.16–1.31	370.24	6.8E+08
21R-4, 0.34–0.49	415.77	1.0E+09
25R-1, 1.20–1.33	448.47	2.8E+09

Note: CSF = core depth below seafloor.

Table T23. APCT3 temperature measurements, Holes C0001E and C0001F. (**See table notes.**)

Core	Depth CSF (m)	Temperature (°C)	RMS misfit (°C)
315-C0001E-			
2H	13.6	2.723	5.00E–03
5H	42.1	4.018	1.10E–02
8H	70.6	5.041	2.70E–02
11H	99.1	6.218	2.00E–03
315-C0001F-			
2H	127.0	6.918	3.00E–03
5H	155.5	8.982	7.00E–03
8H	170.98	9.613	2.20E–03

Notes: APCT3 = advanced piston corer temperature tool. CSF = core depth below seafloor, RMS = root mean square.

Table T24. Core-log depth correlation, Holes C0001E, C0001F, and C0001H. (See table note.)

Hole	Core depth CSF (m)	Corrected depth CSF-B (m)	Logging depth LSF (m)	Depth shift (m)
C0001E	0.00	0.00	0.00	0.00
	12.38	11.80	11.20	–0.60
	34.66	34.48	33.07	–1.41
	54.30	53.96	52.27	–1.69
	74.50	74.14	74.52	0.38
	86.95	86.30	84.28	–2.02
	96.32	95.83	93.42	–2.40
	111.36	111.11	108.81	–2.30
	121.15	120.00	117.70	–2.30
C0001F	108.00	108.00	103.00	–5.00
	114.33	113.85	108.81	–5.04
	130.89	130.89	122.07	–8.82
	169.50	168.87	166.27	–2.60
	184.98	184.47	179.83	–4.64
	196.76	196.76	192.30	–4.46
	207.20	206.93	199.00	–7.93
	212.09	212.00	205.74	–6.26
	218.23	217.85	210.00	–7.85
	227.07	227.00	218.00	–9.00
	250.00	250.00	241.00	–9.00
C0001H	230.00	230.00	229.00	–1.00
	230.50	230.50	229.50	–1.00
	239.80	239.80	237.00	–2.80
	243.78	243.78	241.10	–2.68
	262.10	262.10	261.90	–0.20
	269.05	269.05	269.14	0.09
	271.30	271.30	272.95	1.65
	288.50	288.50	285.45	–3.05
	295.40	295.40	293.83	–1.57
	327.02	327.02	326.29	–0.73
	332.20	332.20	331.62	–0.58
	335.64	335.64	336.04	0.40
	337.75	337.75	339.24	1.49
	341.40	341.40	341.30	–0.10
	353.00	353.00	354.00	1.00
	355.38	355.38	357.38	2.00
	372.27	372.27	370.94	–1.33
	389.35	389.35	387.00	–2.35
	413.10	413.10	413.10	0.00
	417.58	417.58	418.64	1.06
	439.55	439.55	441.80	2.25
	460.00	460.00	460.00	0.00

Note: CSF = core depth below seafloor; CSF-B = CSF, IODP Method B (see the **“Expedition 315 Methods”** chapter); LSF = LWD depth below seafloor.